

広島大学学位請求論文

Exploration of Elementary Processes in Sequential  
Photodissociation Reactions of Transition Metal  
Carbonyls Using Ion Imaging Methods  
(イオンイメージング法を用いた遷移金属カルボニ  
ル錯体の逐次的光解離反応素過程の探索)

2024年

広島大学大学院理学研究科

化学専攻

長森 啓悟

# 目次

## 1. 主論文

Exploration of Elementary Processes in Sequential Photodissociation Reactions  
of Transition Metal Carbonyls Using Ion Imaging Methods

(イオンイメージング法を用いた遷移金属カルボニル錯体の逐次的光解離

反応素過程の探索)

長森 啓悟

## 2. 公表論文

(1) Generation of Highly Vibrationally Excited CO in Sequential  
Photodissociation of Iron Carbonyl Complexes

Keigo Nagamori, Misato Haze, Hiroyuki Nakata, Oliver Zingsheim,  
Katsuyoshi Yamasaki, and Hiroshi Kohguchi

.....The Journal of Physical Chemistry A, 126 (2022) 306

(2) Primary and Secondary Processes in the Ultraviolet Photodissociation of  
CpCo(CO)<sub>2</sub> (Cyclopentadienylcobalt Dicarbonyl)

Keigo Nagamori, Misato Haze, Yuuka Okuda, Katsuyoshi Yamasaki, and  
Hiroshi Kohguchi

.....The Journal of Physical Chemistry A, 127 (2023) 9921.

### 3. 参考論文

- (1) Detection of direct NO ligand loss in the ultraviolet photodissociation of  $\text{Co}(\text{CO})_3\text{NO}$   
Hiroyuki Nakata, Keigo Nagamori, Katsuyoshi Yamasaki, Hiroshi Kohguchi  
Chemical Physics Letters, 707 (2018) 150
- (2) Spectroscopic signatures of  $\text{HHe}_2^+$  and  $\text{HHe}_3$   
Matthias Töpfer, Anders Jensen, Keigo Nagamori, Hiroshi Kohguchi, Tamás Szidarovszky, Attila G. Császár, Stephan Schlemmer and Oskar Asvany  
Physical Chemistry Chemical Physics, 22 (2020), 22885
- (3) Primary and Secondary Loss of CO and NO Ligands in the Ultraviolet Photodissociation of the Heteroleptic  $\text{Co}(\text{CO})_3\text{NO}$  Complex  
Hiroyuki Nakata, Keigo Nagamori, Misato Haze, Katsuyoshi Yamasaki, and Hiroshi Kohguchi  
Journal of Physical Chemistry A, 124 (2020) 10694
- (4) Pure Rotational Spectrum of  $\text{CCl}^+$   
O. Asvany, C. R. Markus, K. Nagamori, H. Kohguchi, J. Furuta, J. Furuta, S. Schlemmer and S. Thorwirth  
The Astrophysical Journal, 910 (2021) 15
- (5) Improvement and determination of higher-order centrifugal distortion constants of the electronic transition of NO  
Misato Haze, Hiroyuki Nakata, Kento Inoue, Ryo Shinohara, Peerapat Wangchingchai, Keigo Nagamori, Yuuki Onitsuka, Katsuyoshi Yamasaki, Hiroshi Kohguchi  
Journal of Molecular Spectroscopy, 378 (2021) 111475

# Table of Contents

## Chapter 1. General Introduction

<b>1.1. Photochemistry of Transition Metal Carbonyl Complexes</b> .....	7
<b>1.2 Overview of features and application areas of transition metal carbonyl complexes</b> .....	9
1.2.1. Bonding Properties of Transition Metal Carbonyl Complexes.....	9
1.2.2. Optical absorption properties and electronic excited states .....	10
<b>1.3. Photodissociation Reactions of Transition Metal Carbonyl Complexes</b> .....	13
1.3.1. State-Resolved Experiment in 1980s .....	14
1.3.2. Ultrafast Time Resolve Experiments in 1990s~2000s .....	15
1.3.3. Ultrafast Time Resolve Experiments in 2010s.....	17
<b>1.4. This Study</b> .....	18
<b>References</b> .....	19

## Chapter 2. Experimental methods and analysis

<b>2.1. Experimental Principle</b> .....	23
2.1.1. Resonance Enhanced Multiphoton Ionization and Non-Resonance Ionization	23
2.1.2. CO REMPI Spectroscopy .....	25
2.1.3. Time of Flight spectroscopy .....	26
2.1.4. Velocity-Map Imaging .....	27
2.1.5. VMI Experiment .....	29
<b>2.2. Velocity Distribution Analysis in the Center-of-Mass Coordinate System</b> .....	31
2.2.1. Convolution of velocity distribution by multi-step dissociation .....	31
2.2.2. Extracting velocity distributions in the CM system by multiple regression analysis.....	33
2.2.3. Error evaluation and gradient descent method .....	34
2.2.4. Program Environment.....	35
<b>2.3. Model validation</b> .....	<b>36</b>
2.3.1. Simple fitting model.....	36
2.3.2. Regularized Model.....	39
2.3.3. Model with reduced parameters .....	41
2.3.4. Mixture of regularized model and reduced number of parameters model .....	42
2.3.5. Multiple Outputs Model .....	43
2.3.6 Removal of non-negative restriction on $w_i$ .....	45
2.3.7 Censoring of iterative calculations.....	48
<b>References</b> .....	49

<b>Chapter 3. Identification of High-<math>\nu</math> Excited CO Generation Processes in the Ultraviolet Photodissociation of Fe(CO)<sub>5</sub></b>	
<b>3-1. Introduction</b> .....	52
<b>3-2. Experimental</b> .....	57
<b>3-3. Results and Discussion</b> .....	60
3-3-1. REMPI spectrum of CO fragments in vibrational state $\nu=0,1$ .....	60
3-3-2. REMPI spectrum of CO fragments in vibrational state $\nu \geq 11$ .....	63
3-3-3. Photolysis wavelength dependence of the Fe(CO) <sub><i>n</i></sub> <sup>+</sup> yield.....	66
3-3-4. Verification by theoretical calculations of specific distributions .....	67
3-3-5. Scattering image of CO and Fe(CO) <sub><i>n=0-4</i></sub> photofragments .....	72
<b>3-4. Conclusion</b> .....	75
<b>References</b> .....	76
<b>Chapter 4. Primary and Secondary Processes in the Ultraviolet Photodissociation of CpCo(CO)<sub>2</sub></b>	
<b>4-1. Introduction</b> .....	83
<b>4-2. Experimental and Calculation methods</b> .....	85
<b>4-3. Results</b> .....	92
4-3-1. UV/Vis absorption spectrum of CpCo(CO) <sub>2</sub> .....	92
4-3-2. Photolysis yield spectra in CpCo(CO) <sub>2</sub> photofragments.....	95
4-3-3. Photolysis wavelength dependence of recoil velocity in CpCoCO, CpCo, CoC <sub>3</sub> H <sub>3</sub> photofragments.....	97
4-3-4. CO photofragment in $\nu = 0,1$ .....	101
<b>4-4. Discussion</b> .....	103
4-4-1. Competition of sequential dissociation and second photodissociation .....	103
4-4-2. Identification of the counterproduct of the second photodissociation .....	107
4-4-3. Potential energy curves of the CO loss of CpCo(CO) <sub>2</sub> and CpCoCO.....	108
4-4-4. Stability of CoC <sub>3</sub> H <sub>3</sub> as an intermediate in CpCo photodissociation .....	108
4-4-5. Contribution of the singlet and triplet states in the CpCo(CO) <sub>2</sub> photodissociation .....	110
<b>4-5. Conclusion</b> .....	111
<b>References</b> .....	113
<b>Chapter 5. General Conclusion</b>	
<b>Acknowledgements</b>	

# **Chapter 1**

## **General Introduction**

## 1.1. Photochemistry of Transition Metal Carbonyl Complexes

Study on photochemical reactions of organic molecules has developed a variety of techniques to deepen our understanding of such reactions. In particular, optical techniques, including lasers, have been widely used in the study of photochemical reactions of organic molecules and have played an important role in elucidating the dynamics and reaction pathways of photochemical reactions. The development of laser technology has contributed greatly to the elucidation of the photochemical reaction dynamics of organic molecules. For example, time-resolved measurements using femtosecond lasers with short pulse widths make it possible to observe the formation of reaction intermediates by photoexcitation and their behavior with high temporal resolution. This enables detailed elucidation of the rate constants of photochemical reactions and the behavior of intermediate steps in the reaction pathway. Furthermore, optical techniques combined with frequency-resolved methods such as infrared spectroscopy, Raman spectroscopy, and resonant multiphoton laser excitation contribute to the analysis of electronic and vibrational states of organic molecules in photochemical reactions. These techniques allow detailed analysis of vibrational energy excitation by photoexcitation and structural changes of molecules in the reaction pathway. Laser-based optical methods, such as flow cell experiments and time-resolved measurements, are also used to control photochemical reaction conditions and analyze products. Advances in optical techniques, including lasers, are essential tools in the study of photochemical reactions of organic molecules. Combined, these techniques provide detailed information on the dynamics of photochemical reactions of organic molecules and on the elucidation of reaction pathways. Furthermore, the application of optical techniques is expected to have applications in a wide range of areas of organic molecular chemistry, such as the

development of new photocatalysts and improvement of the efficiency of organic synthesis.

On the other hand, in the basic physical photochemical reactions of transition metal complexes, it is difficult to obtain detailed experimental data as for organic molecules. Compared to organic molecules, transition metal complexes have more complex structures and reactivity, and understanding their photochemical reactions requires more advanced experimental techniques and theoretical approaches. Many factors are involved in the photochemical reactions of transition metal complexes, including the electronic state of the metal center, the vibrational state of the ligand, and the steric structure of the complex. Detailed analysis of the interactions and effects of these elements requires a combination of advanced experimental techniques and theoretical modeling. Current studies of basic physical photochemical reactions of transition metal complexes use some optical methods, including time-resolved and frequency-resolved methods<sup>1,2</sup>. However, detailed information on the dynamics and reaction pathways of photochemical reactions of transition metal complexes is still insufficient. This is due to the complex behavior of the complexes and the difficulty in elucidating the reaction mechanisms. Therefore, we focused on the photochemical reactions of metal carbonyl complexes. Metal carbonyl complexes are complexes with a bond between a transition metal and a carbonyl group, and are important compounds with a wide range of application areas. Elucidation of their properties and reaction mechanisms is of great significance in the fields of catalysis, materials science, and organic synthesis.<sup>3-</sup>

## 1.2 Overview of features and application areas of transition metal carbonyl complexes

### 1.2.1 Bonding Properties of Transition Metal Carbonyl Complexes

Transition metal carbonyl complexes are compounds with a special bond formed between a transition metal and a carbonyl group (CO). This bonding property has important effects on the stability, reactivity, and photophysical properties of the complexes. First, the most characteristic bonding in transition metal carbonyl complexes is the bonding by  $\sigma$ -donation and  $\pi$ -back donation. This bonding allows the carbonyl group to coordinate to the transition metal center, forming a stable complex. Figure 1-1 shows the bonding scheme of metal-CO in the Dewar–Chatt–Duncanson model.

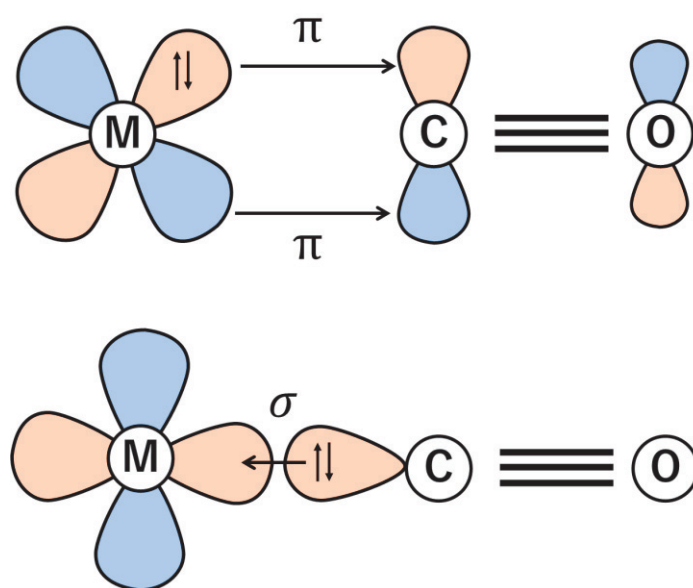


Figure 1-1. Dewar–Chatt–Duncanson model bonding scheme of CO to a transition metal.

The  $\pi$  back donating and  $\sigma$ - donating bond plays an important role in the bonding properties of transition metal carbonyl complexes. These bonds are formed between the d orbital of the transition metal and the  $\pi^*$  orbital of the carbonyl group. This bond attracts the electron density of the transition metal to the carbonyl group, polarizing the bond. This polarization is known to change the vibrational frequency and reactivity of the

carbonyl group and promote photodissociation and electron transfer reactions.

These interactions significantly affect the electron density distribution between the metal center and the ligand.  $\sigma$  donation refers to the transfer of electrons from the ligand to the metal center. In this process, electrons are donated from the non-bonding orbitals of the ligand to the empty d orbitals of the metal. This strengthens the bond between the metal and the ligand. On the other hand,  $\pi$  backdonation refers to the transfer of electrons from the metal center to the ligand. In this case, electrons are transferred from the filled d orbitals of the metal to the empty  $\pi^*$  orbitals of the ligand. The bond length of the CO changes depending on the extent of these interactions<sup>6</sup>. Therefore, the measurement of the CO stretching frequency observed by infrared absorption is a commonly treated method in spectroscopic experiments on metal carbonyl complexes<sup>7</sup>.

### 1.2.2. Optical absorption properties and electronic excited states

The photochemistry of transition metal carbonyl complexes has been applied in the fields of synthesis, photoinduced CO-releasing molecules, photocatalysis, and photopolymerization<sup>8-12</sup>. These are due to the high optical absorption coefficient and high reactivity of transition metal carbonyl complexes. Therefore, absorption properties and electronic excitation states are important factors in the photophysical properties of the complexes, and their understanding is important for elucidating the optical responses and photochemical reactions of transition metal carbonyl complexes. Optical absorption spectra and time-resolved analyses reveal the details of the excited states, energy levels, and relaxation processes of the complexes. This is expected to contribute to the development of applications of complexes with light, such as the control of photoexcited reactions and the rationalization of photocatalytic reactions.

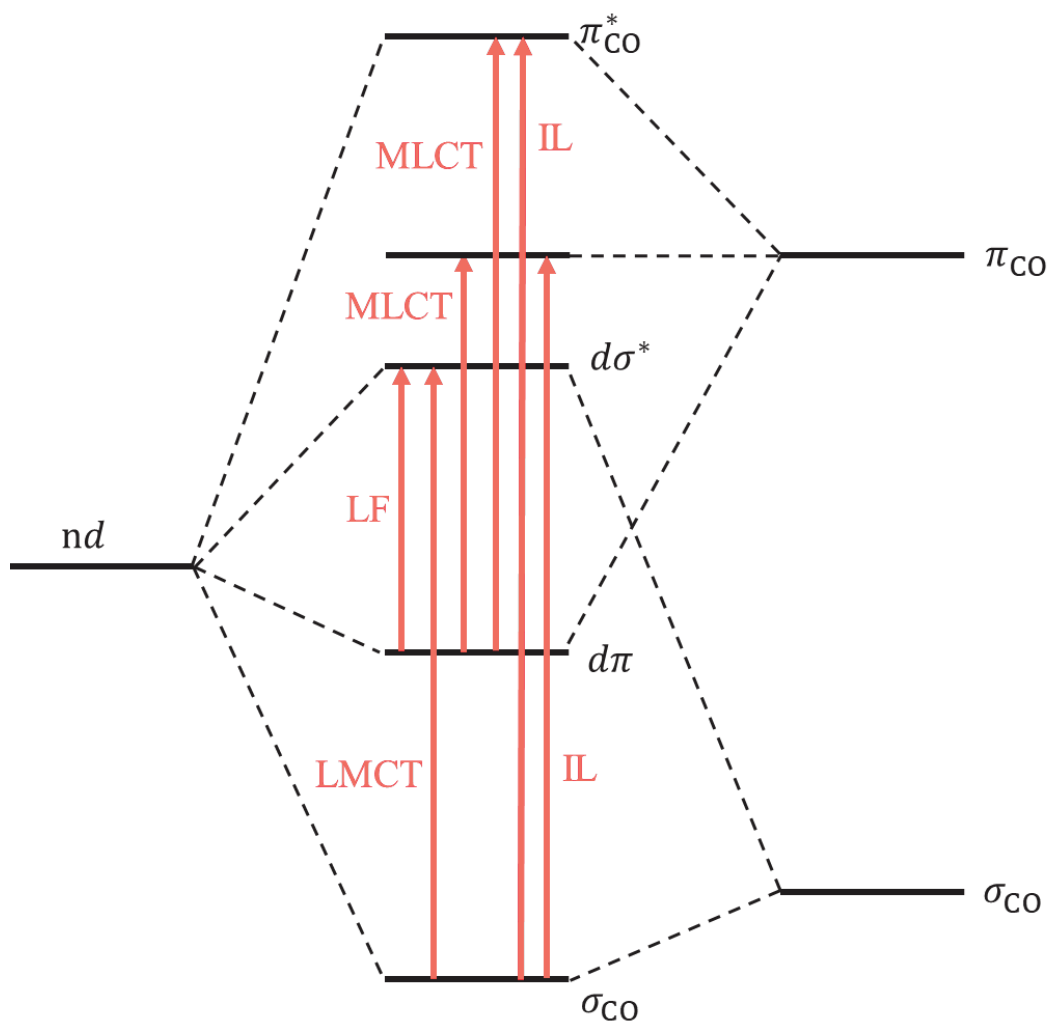


Figure 1-2. Molecular orbital diagram for a transition metal complex. The arrows represent electronic transitions.

Figure 1-2 shows a commonly used type of absorption bands and excited state assignments for mononuclear metal carbonyl complexes. In complexes where the d orbitals are partially filled with electrons, the interaction with the ligand splits the d orbitals, producing absorption bands that represent excitations between the d orbitals. Since this d-d ligand field (LF) transition involves molecular orbitals (MOs) that are predominantly metallic in nature, the resulting electronically excited state is also referred to as a metal-centered (MC) excited state. The d-d transition states are located at lower energies and appear in the visible region. However, in centrosymmetric complexes, the LF band is Laporte forbidden, therefore the extinction coefficient is usually relatively low.

The transition from the metal d orbital to the CO ligand is called the metal-to-ligand charge transfer (MLCT) transition. This transition is not forbidden like the d-d transition and has a high absorption cross section. It is observed over a wide UV-visible region. Other transitions include charge transfer transitions from CO ligands to metals (LMCT; ligand-to-metal charge transfer) and transitions between CO ligands (IL; intra-ligand), which require high energy and are not observed in the UV-visible region. However, it is important to note that many of these ligands and many orbitals described as metal-localized orbitals are in fact of mixed nature.

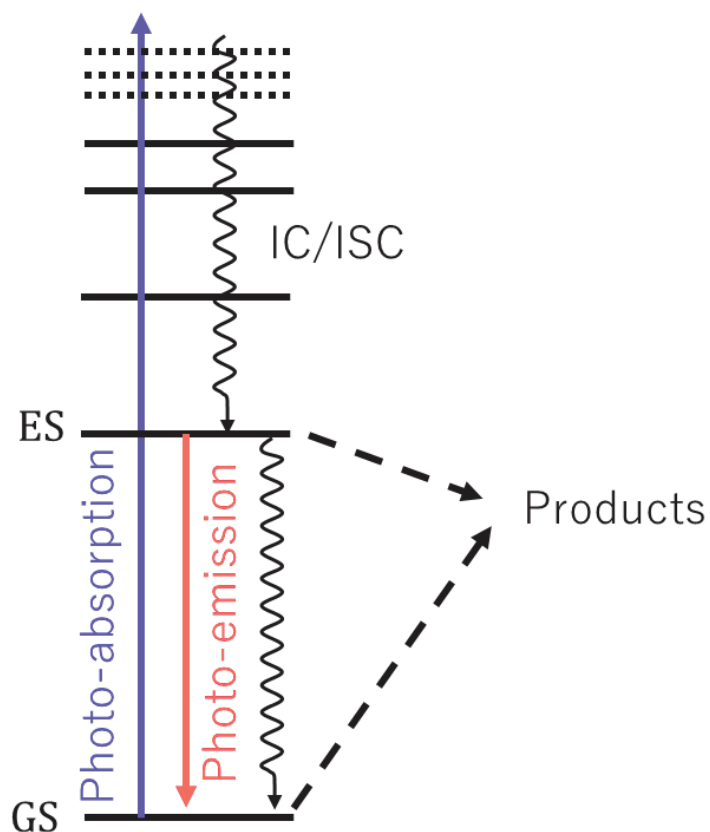


Figure 1-3. Energy diagram illustration the photo-excitation, non-radiative relaxation and photo-emission processes in a transition metal complex. GS, ES, IC, ISC in the figure are grand state, excited state, internal conversion, and intersystem crossing, respectively.

The reaction pathways after light absorption in transition metal carbonyl complexes are complex. Figure 1-3 schematically shows the reaction path after photoexcitation. Electrons excited by light energy relax through several possible pathways, moving between various energy levels. The more complex the structure of the complex, the higher the density of excited states and the greater the probability of going through non-radiative processes such as internal conversion and inter-term crossing. These processes involve the transfer of electrons from one excited state to another without any energy release. This allows the complex to eventually relax to the ground state, where thermally driven chemical reactions can occur. The excited state of the complex can also emit light through a radiative process, which is observed as a luminescence spectrum. In addition, if the energy difference is sufficiently large, dissociation from the excited state may proceed, opening new reaction pathways as the ligand is desorbed. Thus, photoinduced reactions of transition metal complexes involve many competing processes and are an important means of altering the chemical properties of the complexes.

### 1.3. Photodissociation Reactions of Transition Metal Carbonyl Complexes

Many transition metal carbonyl complexes are known to undergo dissociation upon light absorption.



The dissociation products are unstable, and dissociation mechanisms have long been studied. Low-temperature matrix experiments will enable us to immobilize short-lived unsaturated products and analyze their structures in detail<sup>13-16</sup>. However, the energy information of the photogenerated unsaturated complex is lost due to collisions with surrounding molecules. In order to study photoreactions in detail, it is important to study

them in the gas phase.

### 1.3.1. State-Resolved Experiment in 1980s

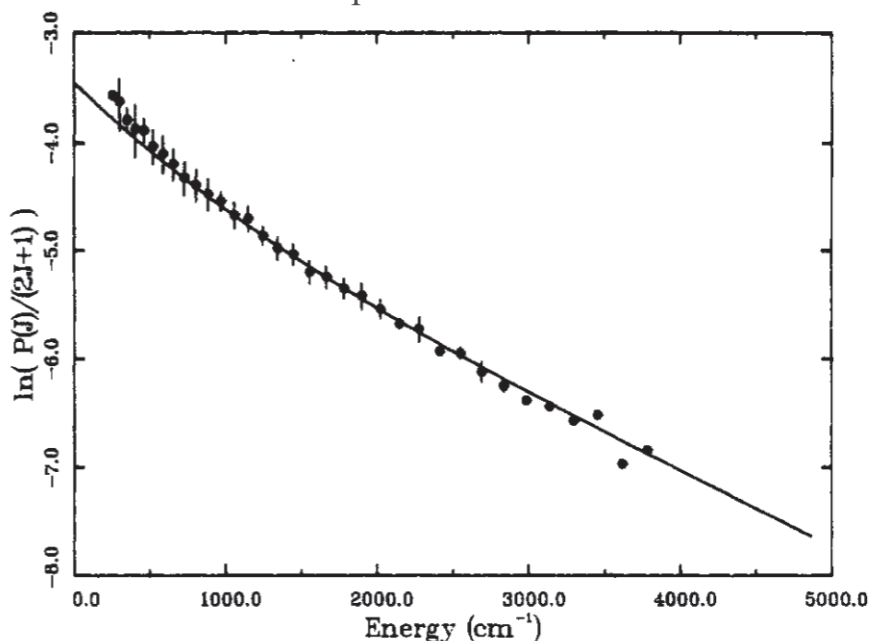


Figure 1-4. Rotational distributions for the CO in  $\nu = 0$  photoproduct from the 193 nm photolysis of  $\text{Fe}(\text{CO})_5$  plotted in the form of Boltzmann plots. The plot is transferred from the reference 17.

There are very few reports on the state-selective experiments of CO fragment. However, in the photodissociation experiments of  $\text{Fe}(\text{CO})_5$  in the 1980s, CO fragment state selection was performed. CO photofragments generated by UV light were excited to the A state by vacuum UV light, and the subsequent emission was measured to determine the rotational distribution for each vibrational state  $\nu = 0, 1, 2$ .<sup>17</sup> Figure 1-4 plots the rotational distribution of CO in  $\nu = 0$  photoproducts from the 193 nm photolysis of  $\text{Fe}(\text{CO})_5$  in the form of a Boltzmann plot. The temperatures obtained by Boltzmann fitting from the obtained rotational distributions and the rotational temperatures obtained by the statistical sequential dissociation model using RRKM theory are consistent, suggesting a statistical sequential dissociation model as the dissociation reaction mechanism. However,

as will be discussed later, with the advent of time-resolved experiments, a fast dissociation mechanism that cannot be explained by statistical dissociation has been observed. This is because CO fragments and their pair products have not been uniquely determined.

### 1.3.2. Ultrafast Time Resolve Experiments in 1990s~2000s

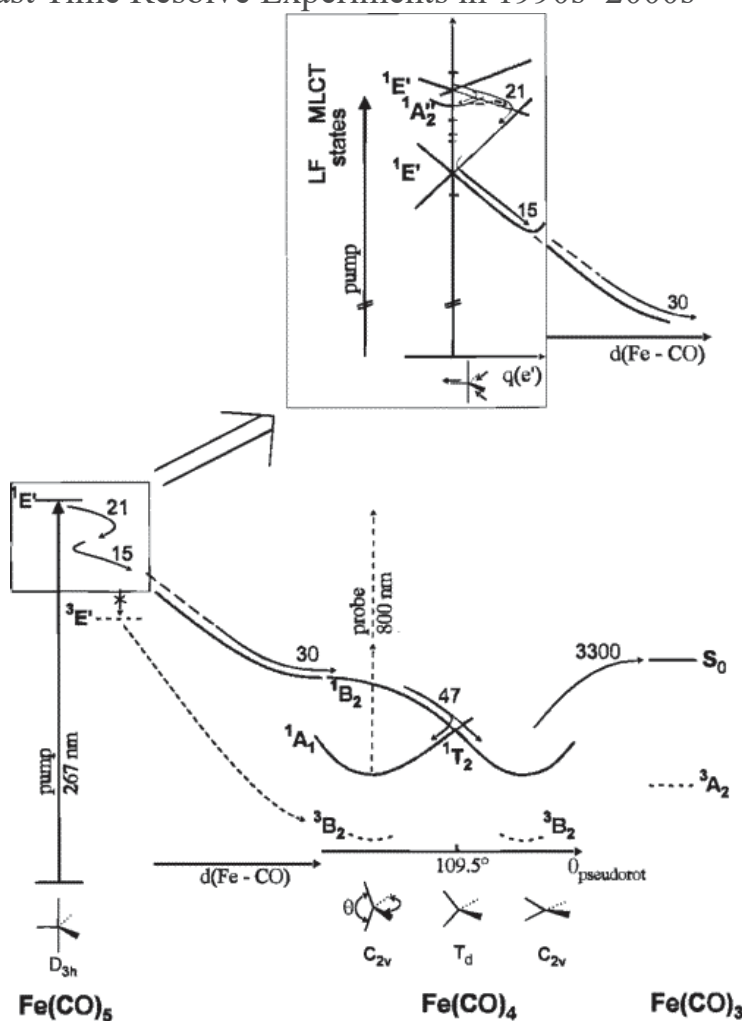


Figure 1-5. Potential energy surface and pathway scheme for UV photolysis of  $\text{Fe}(\text{CO})_5$  proposed by Trushin *et al.* The numbers in the figure are time constants and are on the order of fs. The plot is transferred from the reference 18.

Advances in laser technology have revolutionized the field of time-resolved experiments, particularly with femtosecond lasers. Advances in this technology have made it possible to observe reaction processes on extremely short time scales, revealing

transient phenomena that could not be captured by conventional methods. Particularly noteworthy in this field are the femtosecond laser experiments by Trushin et al<sup>18,19</sup>. Using pump light with a wavelength of 267 nm and probe light with a wavelength of 800 nm, Trushin et al. precisely measured the signal intensity of transient unsaturants by setting a specific delay time. This technique allowed us to determine the time constant of the reaction, on the basis of which a dissociation reaction model shown in figure 1-5 was proposed. The model is a fast internal conversion to the dissociative LF (Ligand Field) state, especially after the MLCT (Metal-to-Ligand Charge Transfer) transition of the metal complex. After this internal conversion, the 1st CO desorption reaction occurs at a remarkable rate of within 100 fs.

This is the fact that the dissociation reaction proceeds in the singlet state even though the electronic ground state of  $\text{Fe}(\text{CO})_4$  is in the triplet state. This fact provides new insights into the dynamics of electronic states in the dissociation process. These proposed dissociation models are proposed to apply equally well to metal carbonyl complexes of the  $\text{M}(\text{CO})_6$  type, furthering our understanding of the photochemical reaction mechanisms of metal carbonyls.<sup>19,20</sup>

### 1.3.3. Ultrafast Time Resolve Experiments in 2010s

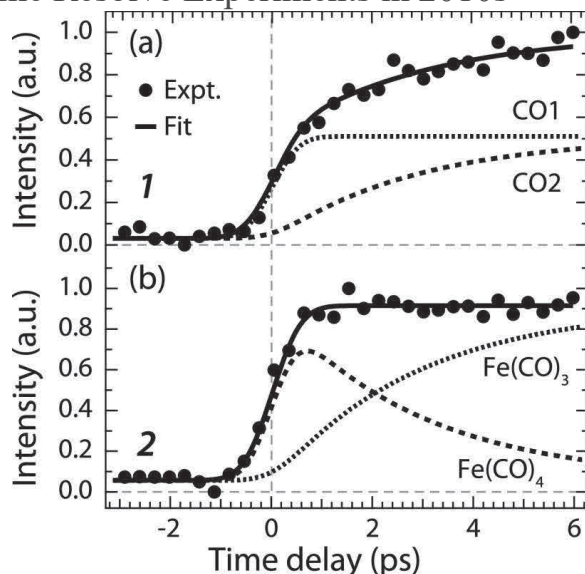


Figure 1-6. Integrated intensities of CO, Fe(CO)<sub>4</sub>, and Fe(CO)<sub>3</sub> valence photoelectron peaks (1 and 2) versus pump-probe delay time. The best fit of a kinetic model is shown as solid lines with the respective components. The plot is transferred from the reference 21.

Experiments have also been conducted to support the model of Trushin et al. The model assumes sequential dissociation. However, it remains unclear whether the dissociation occurs simultaneously or sequentially. Also, the time constants obtained did not uniquely identify the species. To address this issue, Wernet et al. designed and performed a time-resolved experiment using photoelectron spectroscopy.<sup>21</sup> By employing this advanced experimental technique, they were able to observe the reaction process on a very short time scale and directly follow the sequential dissociation process. Specifically, they performed experiments on the photodissociation reaction of Fe(CO)<sub>5</sub> and analyzed in detail the time evolution of the signals corresponding to the products CO, Fe(CO)<sub>4</sub>, and Fe(CO)<sub>3</sub>, as shown in Figure 1-6.

The experimental results were surprising: it was observed that the time variation of the signal corresponding to CO and the Fe signal corresponding to Fe(CO)<sub>4</sub> and

$\text{Fe}(\text{CO})_3$  coincided perfectly with the time constant. This coincidence provides direct evidence for a sequential dissociation process in which  $\text{Fe}(\text{CO})_5$  first dissociates into  $\text{Fe}(\text{CO})_4$  and CO, and then  $\text{Fe}(\text{CO})_4$  further dissociates into  $\text{Fe}(\text{CO})_3$  and CO. This result strongly supports the model proposed by Trushin et al. and opens a new breakthrough in understanding the dissociation mechanism of chemical reactions.

#### 1.4. This Study

Studies of photodissociation reactions of metal complexes have used two main approaches: time-resolved and energy-resolved approaches. The time-resolved approach is superior in capturing the temporal changes in the reaction over a short time span, but has the limitation of relatively low energy resolution. On the other hand, the energy-resolved approach uses pulses with narrower energy widths to precisely measure the energy state distribution of fragments but has lower temporal resolution, mainly observing only fragments after the reaction is complete. These methods are complementary to each other, and both perspectives are important for understanding the detailed mechanisms of photodissociation reactions of metal carbonyl complexes.

However, previous studies have been insufficient to detect CO fragments and to assess their role as end products in energy transfer and photodissociation. Despite the importance of the findings, especially those obtained from the energy resolution approach, research in this area has not yet progressed sufficiently. One reason for this is the phenomenon of "ladder switching" in metal complexes with high absorption cross sections, in which the dissociatively generated fragments further progress in optical absorption, eventually progressing to bare metal atoms.<sup>22-24</sup> In this process, it is difficult to uniquely determine which dissociation process each CO fragment originates from, and the analysis becomes more complicated as the number of CO fragments increases.

Therefore, in this study, the ion imaging method is used to clarify the elementary reaction processes of the detected CO fragments. This methodology will allow us to investigate in detail the origin and dynamics of CO fragments in the photodissociation reaction of metal carbonyl complexes, which has been difficult to elucidate using conventional methods. This advance will lead to a better understanding of the photochemistry and photophysical chemistry of metal complexes and pave the way for the development of new photoinduced reactions.

## References

1. Cole-Filipiak NC, Tross J, Schrader P, et al. Ultraviolet photodissociation of gas-phase iron pentacarbonyl probed with ultrafast infrared spectroscopy. *Journal of Chemical Physics* 2021;154(13), doi:10.1063/5.0041074
2. Turner JJ, George MW, Poliakoff M, et al. Photochemistry of transition metal carbonyls. *Chemical Society Reviews* 2022;51(13):5300-5329, doi:10.1039/d1cs00826a
3. Hoyano JK, McMaster AD, Graham WAG. ACTIVATION OF METHANE BY IRIIDIUM COMPLEXES. *Journal of the American Chemical Society* 1983;105(24):7190-7191, doi:10.1021/ja00362a039
4. Perutz RN, Procacci B. Photochemistry of Transition Metal Hydrides. *Chemical Reviews* 2016;116(15):8506-8544, doi:10.1021/acs.chemrev.6b00204
5. Szymanska-Buzar T. Photochemical reactions of Group 6 metal carbonyls in catalytic transformation of alkenes and alkynes. *Coordination Chemistry Reviews* 1997;159(205-220), doi:10.1016/s0010-8545(96)01291-x
6. Timney JA. Ligand effect constants: A new method for predicting the carbonyl stretching frequencies in transition-metal compounds. *Inorganic chemistry* 1979;18(2502)
7. Snee PT, Payne CK, Kotz KT, et al. Triplet organometallic reactivity under ambient conditions: An ultrafast UV pump/IR probe study. *Journal of the American Chemical Society* 2001;123(10):2255-2264, doi:10.1021/ja002350r
8. Askes SHC, Reddy GU, Wyrwa R, et al. Red Light-Triggered CO Release from Mn-2(CO)(10) Using Triplet Sensitization in Polymer Nonwoven Fabrics. *Journal of the American Chemical Society* 2017;139(43):15292-15295, doi:10.1021/jacs.7b07427
9. Schatzschneider U. PhotoCORMs: Light-triggered release of carbon monoxide from the coordination sphere of transition metal complexes for biological applications. *Inorganica Chimica Acta* 2011;374(1):19-23, doi:10.1016/j.ica.2011.02.068

10. Li Z, Pierri AE, Huang PJ, et al. Dinuclear PhotoCORMs: Dioxxygen-Assisted Carbon Monoxide Uncaging from Long-Wavelength -Absorbing Metal-Metal-Bonded Carbonyl Complexes. *Inorganic Chemistry* 2017;56(11):6094-6104, doi:10.1021/acs.inorgchem.6b03138
11. Hammarback LA, Aucott BJ, Bray JTW, et al. Direct Observation of the Microscopic Reverse of the Ubiquitous Concerted Metalation Deprotonation Step in C-H Bond Activation Catalysis. *Journal of the American Chemical Society* 2021;143(3):1356-1364, doi:10.1021/jacs.0c10409
12. Simpson CP, Adebolu OI, Kim JS, et al. Metal and Ligand Effects of Photoactive Transition Metal Carbonyls in the Iodine Degenerative Transfer Controlled Radical Polymerization and Block Copolymerization of Vinylidene Fluoride. *Macromolecules* 2015;48(18):6404-6420, doi:10.1021/acs.macromol.5b00698
13. Stolz IW, Dobson GR, Sheline RK. The Infrared Spectrum and Evidence for the Structure of a New Metal Carbonyl. *Journal of the American Chemical Society* 1962;84(2)
14. Stolz IW, Dobson GR, Sheline RK. Evidence for the Existence of Group VI Metal Pentacarbonyls. *Journal of the American Chemical Society* 1963;85(2)
15. Crichton O, Rest AJ. PHOTOCHEMISTRY OF TRICARBONYLNITROSYLCOBALT IN FROZEN GAS MATRICES AT 20 K - IR SPECTROSCOPIC EVIDENCE FOR DICARBONYLNITROSYLCOBALT AND DICARBONYL(DINITROGEN)NITROSYLCOBALT. *Journal of the Chemical Society-Dalton Transactions* 1977;6):536-541, doi:10.1039/dt9770000536
16. Poliakoff M, Turner JJ. INFRARED-SPECTRA AND PHOTOCHEMISTRY OF COMPLEX PENTACARBONYLIRON IN SOLID MATRICES AT 4 AND 20 K - EVIDENCE FOR FORMATION OF COMPLEX TETRACARBONYLIRON. *Journal of the Chemical Society-Dalton Transactions* 1973;13):1351-1357, doi:10.1039/dt9730001351
17. Waller IM, Hepburn JW. State-Resolved Photofragmentation Dynamics of Fe(CO)<sub>5</sub> at 193, 248, 266, and 351 nm. *Journal of Chemical Physics* 1988;88(10):6658-6669, doi:10.1063/1.454406
18. Trushin SA, Fuss W, Kompa KL, et al. Femtosecond Dynamics of Fe(CO)<sub>5</sub> Photodissociation at 267 nm Studied by Transient Ionization. *Journal of Physical Chemistry A* 2000;104(10):1997-2006, doi:10.1021/jp992474u
19. Trushin SA, Fuss W, Schmid WE, et al. Femtosecond Dynamics and Vibrational Coherence in Gas-phase Ultraviolet Photodecomposition of Cr(CO)<sub>6</sub>. *Journal of Physical Chemistry A* 1998;102(23):4129-4137, doi:10.1021/jp973133o
20. Trushin SA, Kosma K, Fuss W, et al. Wavelength-independent ultrafast dynamics and coherent oscillation of a metal-carbon stretch vibration in photodissociation of Cr(CO)<sub>6</sub> in the region of 270-345 nm. *Chemical Physics* 2008;347(1-3):309-323,

doi:10.1016/j.chemphys.2007.09.057

21. Wernet P, Leitner T, Josefsson I, et al. Direct evidence for sequential dissociation of gas-phase Fe(CO)<sub>5</sub> via a singlet pathway upon excitation at 266 nm. *Journal of Chemical Physics* 2017;146(21):211103, doi:10.1063/1.4984774
22. Willey KF, Brummel CL, Winograd N. Photoionization mechanisms for Cr(CO)<sub>6</sub> using high intensity laser pulses in the near-IR. *Chemical Physics Letters* 1997;267(3-4):359-364, doi:10.1016/s0009-2614(97)00089-4
23. Gobeli DA, Yang JJ, El-Sayed MA. LASER MULTIPHOTON IONIZATION DISSOCIATION MASS-SPECTROMETRY. *Chemical Reviews* 1985;85(6):529-554, doi:10.1021/cr00070a002
24. Niles S, Prinslow DA, Wight CA, et al. LASER MULTIPHOTON IONIZATION AND PHOTOELECTRON-SPECTROSCOPY OF CO(CO)<sub>3</sub>NO AND FE(CO)<sub>5</sub>. *Journal of Chemical Physics* 1990;93(9):6186-6199, doi:10.1063/1.458988

# **Chapter 2**

## **Experimental methods and analysis**

## 2.1. Experimental Principle

### 2.1.1 Resonance Enhanced Multiphoton Ionization and Non-Resonance Ionization

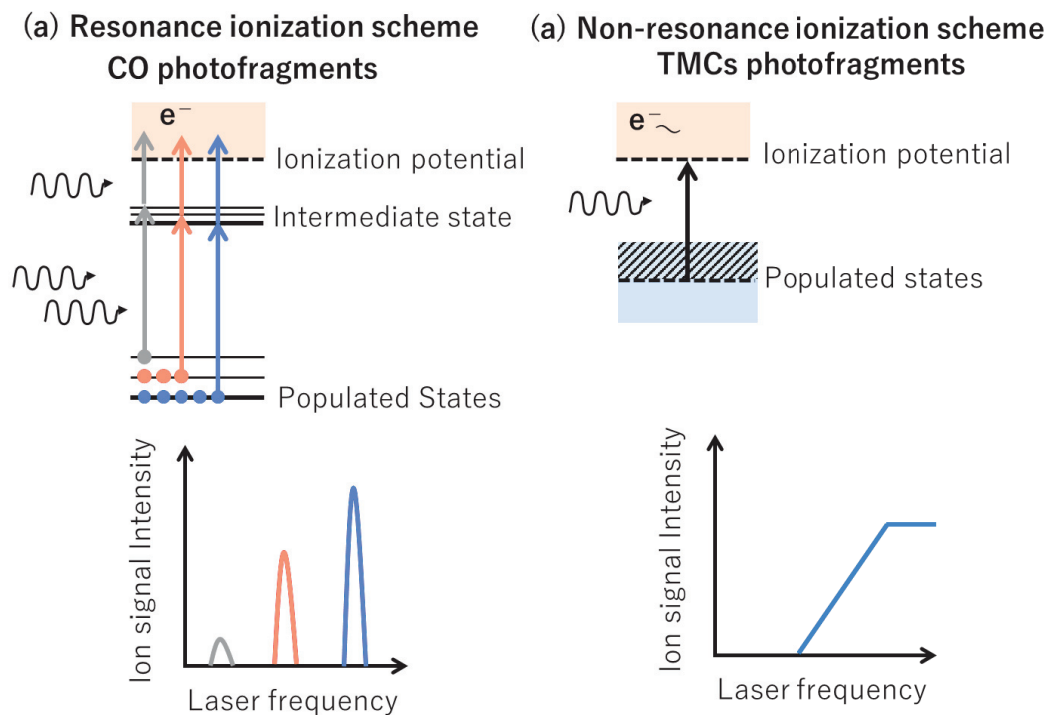


Figure 2-1. Scheme of REMPI and non-resonance ionization processes.

The ionization process involves state-selective ionization using resonance and non-resonant state-selective ionization. Figure 2-1 shows the ionization schemes. The Resonance Enhanced Multi-Photon Ionization (REMPI) method is a technique for detecting dissociation reaction products under very low pressure. In this method, a molecule reaches a resonance state when one or more photons are absorbed by the molecule and their energies match the energy difference between the ground and excited states. In the REMPI method, the number of photons involved in the resonance transition ( $n$ ) and the number of photons required for the subsequent ionization transition ( $m$ ) are expressed together as  $[n + m]$  REMPI.

Ionized molecules pass through an electric field and are separated and detected

by a time-of-flight (TOF) mass spectrometer. REMPI spectra are obtained by monitoring the rate of ion production while varying the laser frequency. The intensity of the spectrum depends on the line strength factor and the population of molecules in a particular state. This makes it possible to measure the final state distribution of dissociation products from the REMPI spectrum.

State-selective ionization of molecules with dense electronic states, such as coordination unsaturated molecules, is difficult. However, when photoabsorption exceeds the ionization threshold, they ionize non-resonantly without going through a transition state. Metal complexes excited to an internal hot by multi-step photodissociation can observe the signal remarkably. In particular, since metal atoms cannot dissociate or otherwise release energy, the ion signal is observed several hundred times stronger than that of other unsaturated materials. The ion intensity depends on the population, laser intensity, and absorption cross section. Since the absorption cross section is wavelength dependent, the non-resonant ion signal intensity also varies with wavelength.

## 2.1.2 CO REMPI Spectroscopy

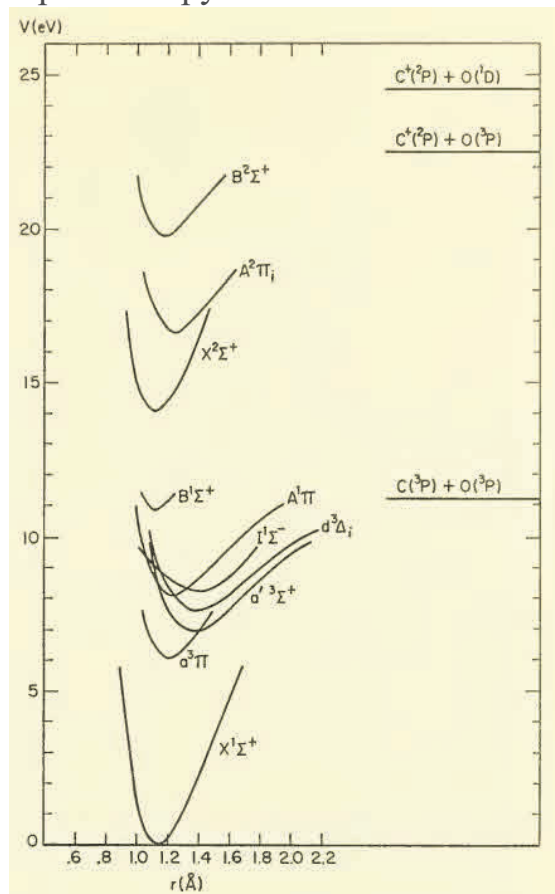


Figure 2-2. Potential energy curves for CO and CO<sup>+</sup>. The plot is transferred from the reference 1.

In the potential energy curves for each electronic state of CO shown in Figure 2-2, the B<sup>1</sup>Σ<sup>+</sup>–X<sup>1</sup>Σ<sup>+</sup> transition process is the most used transition for laser ionization detection of CO.<sup>2</sup> The spectroscopic constant is reported and the band origin of the B<sup>1</sup>Σ<sup>+</sup>–X<sup>1</sup>Σ<sup>+</sup> transition places at 115.05 nm<sup>3-5</sup>. This energy is in the vacuum ultraviolet region, but the transition is possible with two-photon absorption at 230.10 nm. Explicit two-photon absorption cross sections for linearly and circularly polarized rotating diatomic molecules were derived by Bray and Hochstrasser.<sup>6</sup> Because  $\Omega' = \Omega'' = 0$  for the B-X transition of CO, there are only O-, Q-, and S-branches ( $\Delta J = 0, \pm 2$ ) in the REMPI spectrum. Furthermore, the O- and S-branches are negligible in intensity for linearly polarized light. However, as shown in Figure 2-2,  $\nu' > 2$  in the B-X transition is

decomposed into C and O by predissociation. Therefore, it is difficult to detect CO with  $v' > 2$  in the UV region.

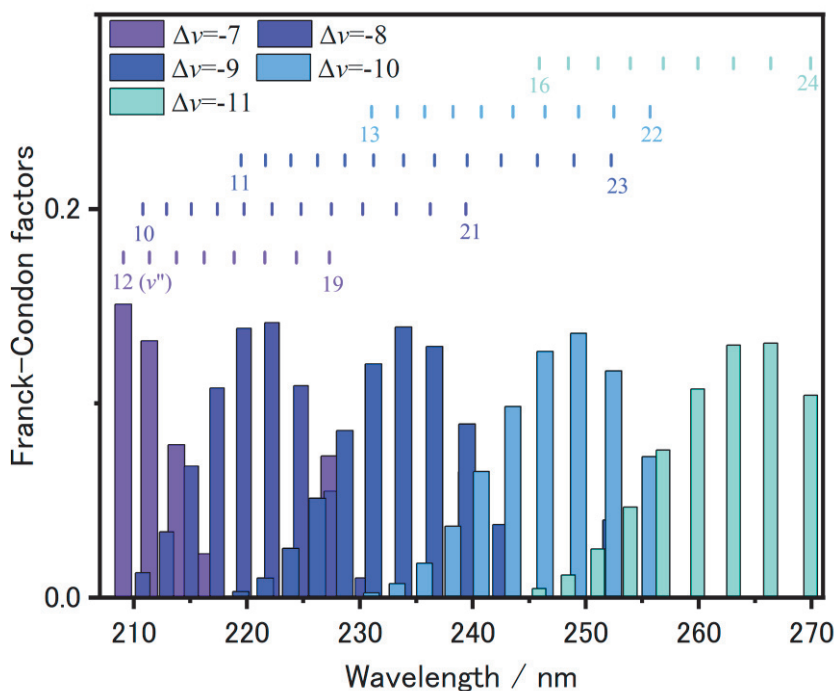


Figure 2-3. Frack-Condon factors for CO A-X transition and band origins.

Vibrationally excited states via the B state cannot be detected by predissociation, while very highly vibrationally excited CO with  $v \geq 10$  can be detected in the UV region by using  $A^1\Pi-X^1\Sigma^+$  Fourth positive system transitions. Figure 2-3 shows the position of the band head and the magnitude of the Franck-Condon factor. In the ultraviolet region, the P, Q, R-branch is observed because of the one-photon transition to the A state.

### 2.1.3 Time of Flight spectroscopy

Molecules and atoms ionized by resonance and non-resonance can be separated by mass by applying an electric field. Defining the electric field as  $V$ , the fragment mass as  $m$ , the, the electric charge as  $z$ , and the elementary charge as  $e$ , respectively, the kinetic

energy of fragment ions  $E = \frac{1}{2}mv^2$  is converted from the electric field by equation (1).

$$zeV = \frac{1}{2}mv^2 \quad (1)$$

If an ion detector is placed in the direction of acceleration of ions by an electric field, mass selection can be done by time of flight. If the flight distance to the detector is  $L$  and the time of flight is  $t$ , the following equation is obtained.

$$t = \frac{L}{v} = \sqrt{\left(\frac{m}{z}\right)\left(\frac{L^2}{2eV}\right)} \quad (2)$$

A mass spectrum can be obtained when the horizontal axis is time and the vertical axis is ion intensity. To obtain wavelength dependence, this TOF spectrum is used in combination with a non-resonant ionization method.

#### 2.1.4 Velocity-Map Imaging (VMI)

The dissociation mechanism is sensitive to the motion on the potential surface and can be considered by measuring the angular and velocity distribution of the dissociation products. If the ionized atoms or molecules have the same velocity component parallel to the detector after ionization, they can be mapped to the same spot on the detector independent of the initial position of the molecules. Furthermore, since it is possible to obtain the entire angular distribution in a single measurement, it has been an effective experimental technique for dissociation dynamics research since it was developed around 1990.<sup>7,8</sup>

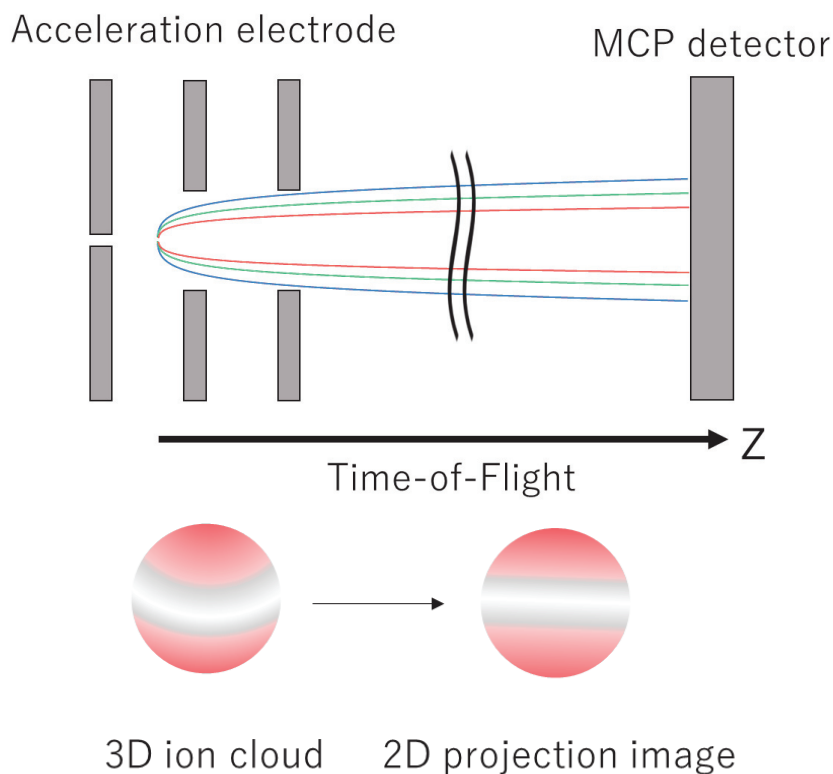


Figure 2-4. Schematic diagram of velocity map imaging (VMI) device.

Figure 2-4 shows a schematic diagram of the VMI system. The accelerating electrodes accelerate ions in the z-axis direction and the voltage is adjusted so that the velocity vectors  $(v_x, v_y)$  of the ions diffused by the dissociation are detected at the same spot. The ions arrive at the detector with a mass-dependent time of flight. The detected image is a two-dimensional image of a three-dimensional ion cloud projected in two dimensions, as shown in the figure. The observed ion scattering distribution image is reconstructed into a three-dimensional distribution by a mathematical method called the Abel transform; by extracting two-dimensional slices from the three-dimensional distribution, a velocity vector  $(v_x, v_y)$  image is obtained. By integrating the obtained images in the velocity and angle directions  $v$  and  $\theta$ , respectively, the velocity distribution  $P(v)$  and the angle distribution  $I(\theta)$  are obtained.

The radial distribution of CO fragments obtained from the scattering distribution

is calibrated to velocity based on previous studies, and the velocity per unit pixel is obtained exactly from the conversion factor. On the other hand, the velocity calibration of the unsaturated fragment  $M(\text{CO})_x$ , for which no previous study is available, is approximated from the mass ratio to the velocity calibrated CO fragment. The radial distance  $r$  depends on the fragment velocity  $v$  and time of flight  $t$ .

$$r \approx vt \quad (3)$$

Since the  $t$  is obtained from TOF, we obtain

$$v_{M(\text{CO})_x} = \sqrt{\frac{m_{\text{CO}}}{m_{M(\text{CO})_x}}} v_{\text{CO}} \quad (4)$$

Then, it is possible to approximate the unknown velocity calibration from the known velocity calibration.

### 2.1.5 VMI Experiment

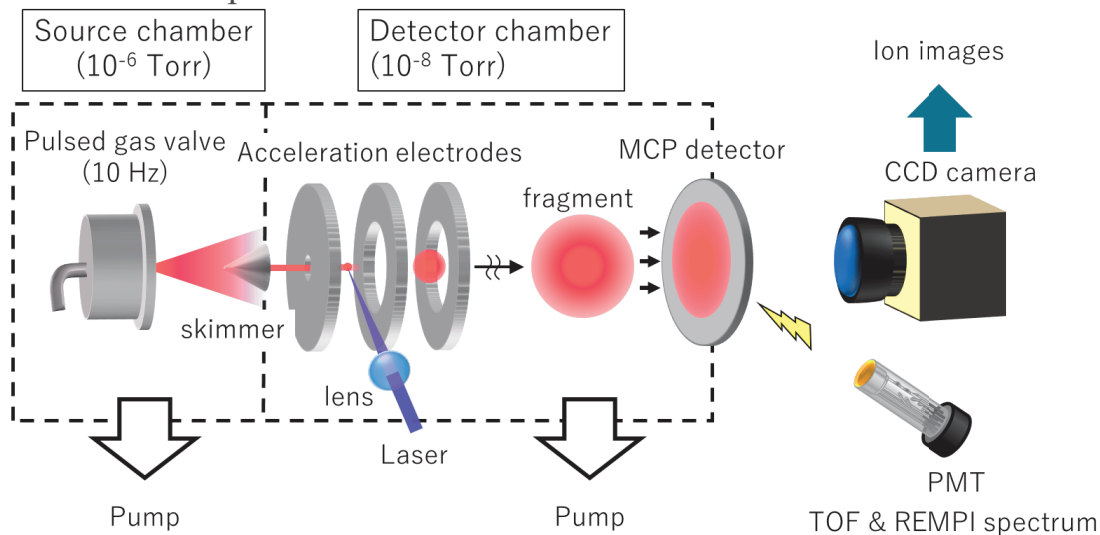


Figure 2-5. Schematic experimental setup.

The experimental setup is shown in Figure 2-5. The experiment was performed using a standard velocity-mapped imaging (VMI) apparatus consisting of a supersonic molecular beam source and an ion imaging system with a time-of-flight (TOF) mass spectrometer. The details of the experimental setup are also described elsewhere.<sup>9,10</sup> The

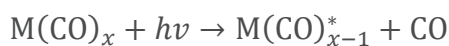
gas sample, diluted with He, was supersonically expanded in vacuum through a piezoelectric pulse valve at a stagnant pressure of 2 bar. The molecular beam was skimmed (1.5 mm diameter) before entering the ion imaging detector chamber. The internal pressures of the source and detector chambers were on the order of  $10^{-6}$  Torr and  $10^{-7}$  Torr, respectively, when the pulsed molecular beam was injected repeatedly at 10 Hz. The molecular beam intersected perpendicularly with the laser beam that was loosely focused between the VMI electrode plates. The laser beam was generated using a frequency doubled wavelength tunable dye laser (CobraStretch, Spectra Physics) excited by the third harmonic of an Nd:YAG laser (LAB-170, Spectra Physics). Photolysis and photoionization occur within the same laser pulse. The pulse width is approximately 10 ns. Photoionized fragments are quickly extruded into the MCP detector (chevron type, 40 mm dia., Photonis) by the VMI electric field generated by the three electrodes. Mass spectrometric separation of photoionized fragments is achieved by TOF in the field-free region (490 mm) and gating of the MCP detector (gate width 100 ns) by a high-voltage pulser module with a MOSFET transistor switch (HTS 31-06, Behlke). Mass analysis of photoionized fragments is achieved by time-of-flight (TOF) measurements in a 490 mm field-free space and microchannel plate (MCP) detector with a gate width controlled by a high-voltage pulser using a MOSFET transistor switch (HTS 31-06, Behlke) This is done by gate operation. The ion yield corresponding to the spectral intensity is obtained from the photomultiplier tube (PMT, R2496, Hamamatsu Photonics) emitted from the MCP. Scattering images are obtained from the emission from the ion hit positions using a CCD camera (C8800, Hamamatsu Photonics).

## 2.2. Velocity Distribution Analysis in the Center-of-Mass Coordinate System

The python language has a wide variety of libraries for machine learning, and there are also plenty of reference books available to make it easy for anyone to do machine learning.

### 2.2.1 Convolution of velocity distribution by multi-step dissociation

In the photodissociation of the transition metal carbonyl complex  $M(\text{CO})_x$ , sequential dissociation proceeds easily.



The asterisk indicates an internally hot state, and sequential dissociation proceeds when the internal energy exceeds the bond dissociation energy. The velocity distribution of the dissociation products after the 1st photodissociation detected in the molecular beam photodissociation experiment does not reflect the velocity distribution in the center of mass (CM) coordinate system due to the bottom-up of the recoil velocity by the 1st photodissociation. Then, the CM velocity distribution of the second-order dissociation products is considered from the coupled vector model. Here, the velocity vector of each  $M(\text{CO})_{x-n}$  ( $n \geq 0$ ) in the experimental system is denoted by  $\mathbf{v}$ , the velocity vector in the CM system by  $\mathbf{u}$ , and  $n$  as a subscript can be expressed as follows: the velocity vector of the unsaturated  $M(\text{CO})_{x-1}$  produced by the first-order photodissociation of  $M(\text{CO})_x$  is denoted by  $\mathbf{v}_1$ , and the velocity vector of the unsaturated  $M(\text{CO})_{x-1}$  recoil velocity vector due to the dissociation of  $M(\text{CO})_{x-2}$  is  $\mathbf{u}_2$ , and the observed velocity vector of unsaturated  $M(\text{CO})_{x-2}$  is  $\mathbf{v}_2$ . In the molecular beam experiment, the velocity vector  $\mathbf{v}_1$  of the fragment corresponding to the 1st photodissociation process is  $\mathbf{v}_1 = \mathbf{u}_1$  since the parent molecule

has no initial velocity. The following relationship equation holds for  $\mathbf{v}_1$ ,  $\mathbf{u}_2$ , and  $\mathbf{v}_2$  as shown in the figure 2-6.

$$\mathbf{v}_1 + \mathbf{u}_2 = \mathbf{v}_2 \quad (5)$$

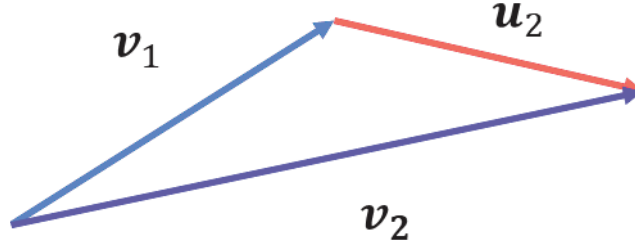


Figure 2-6 Vector coupling model for second-order dissociation

The velocity vector distribution  $P_2^{LAB}(\mathbf{v}_2)$  is obtained by convolving  $P_1^{LAB}(\mathbf{v}_1)$  and  $P_2^{CM}(\mathbf{u}_2)$  with the following formula,

$$P_2^{LAB}(\mathbf{v}_2) = \int P_1^{LAB}(\mathbf{v}_1) P_2^{CM}(\mathbf{u}_2) d\mathbf{v}_1 \quad (6)$$

In the polar coordinate representation  $d\mathbf{v}_1 = v_1^2 \sin \theta dv_1 d\theta d\phi$ ,

$$P_2^{LAB}(\mathbf{v}_2) = \int_0^\infty \int_0^\pi \int_0^{2\pi} P_1^{LAB}(\mathbf{v}_1) P_2^{CM}(\mathbf{u}_2) v_1^2 \sin \theta d\phi d\theta dv_1 \quad (7)$$

When  $P_1^{LAB}(\mathbf{v}_1)$  and  $P_2^{CM}(\mathbf{u}_2)$  are isotropic scattering distributions,  $P_1^{LAB}(\mathbf{v}_1)$  is independent of  $\theta$  and  $\phi$ . On the other hand,  $P_2(\mathbf{u}_2)$  can be integrated only with  $\phi$  from the following equation, since  $\mathbf{u}_2 = \mathbf{v}_2 - \mathbf{v}_1$  from the coupled vector model.

$$u_2 = |\mathbf{u}_2| = |\mathbf{v}_2 - \mathbf{v}_1| = \sqrt{|\mathbf{v}_2|^2 - 2|\mathbf{v}_2||\mathbf{v}_1| \cos \theta + |\mathbf{v}_1|^2} \quad (8)$$

Therefore, equation (7) can be further transformed to following equation

$$P_2^{LAB}(\mathbf{v}_2) = 2\pi \int_0^\infty \left[ P_1^{LAB}(\mathbf{v}_1) v_1^2 \int_0^\pi P_2^{CM}(\mathbf{u}_2) \sin \theta d\theta \right] dv_1 \quad (9)$$

In the case of isotropic scattering distribution, the velocity distribution  $P(v)$  and the velocity vector distribution  $P(\mathbf{v})$  have the following relationship.

$$P(v) = 4\pi v^2 P(\mathbf{v}) \quad (10)$$

Therefore, transforming equation (9) into a velocity distribution yields

$$\frac{P_2^{LAB}(v_2)}{4\pi v_2^2} = 2\pi \int_0^\infty \left[ \frac{P_1^{LAB}(v_1)}{4\pi v_1^2} v_1^2 \int_0^\pi \frac{P_2^{CM}(u_2)}{4\pi u_2^2} \sin \theta \, d\theta \right] dv_1 \quad (11)$$

For isotropic scattering distribution, it is possible to obtain  $P_2^{CM}(u_2)$  analytically by measuring only the velocity distribution.

### 2.2.2 Extracting velocity distributions in the CM system by multiple regression analysis

It is difficult to directly obtain the velocity distribution in the center of mass coordinates of a secondary dissociation fragment from Eq. (11). However, it is possible to obtain an approximate solution by regression analysis. Regression analysis is a method of modeling and analyzing the relationship between two or more variables in statistics. Regression analysis estimates the relationship between variables and is widely used in various analyses. the  $P_2^{CM}(u_2)$  extraction method consists of three steps; (1) creation of a group of independent functions in the center of mass coordinate system (2) 3D convolution (3) fitting by multiple regression analysis.

Since  $P_2^{CM}(u_2)$  can be expressed as a linear combination of any group of independent functions  $q_s$ , we have

$$P_2^{CM}(\mathbf{u}_2) = \sum_i w_i q_i(\mathbf{u}_2) \quad (12)$$

where  $q_i(u_2)$  is any independent function and  $w_i$  are the coefficients.

Substituting this equation into Eq. (9) yields

$$P_2^{LAB}(v_2) = 2\pi \int_0^\infty \left[ P_1^{LAB}(v_1) v_1^2 \int_0^\pi \sum w_i q_i(\mathbf{u}_2) \sin \theta \, d\theta \right] dv_1 \quad (13)$$

Applying  $\int [f(x) + g(x)] dx = \int f(x) dx + \int g(x) dx$ ,

$$\begin{aligned} P_2^{LAB}(v_2) &= 2\pi w_1 \int_0^\infty \left[ P_1^{LAB}(v_1) v_1^2 \int_0^\pi q_1(\mathbf{u}_2) \sin \theta \, d\theta \right] dv_1 \\ &+ 2\pi w_2 \int_0^\infty \left[ P_1^{LAB}(v_1) v_1^2 \int_0^\pi q_2(\mathbf{u}_2) \sin \theta \, d\theta \right] dv_1 \end{aligned} \quad (14)$$

$$+ \dots + 2\pi w_n \int_0^\infty \left[ P_1^{LAB}(\mathbf{v}_1) v_1^2 \int_0^\pi q_n(\mathbf{u}_2) \sin \theta \, d\theta \right] dv_1$$

Here, the following equation is defined,

$$2\pi w_i \int_0^\infty \left[ P_1^{LAB}(\mathbf{v}_1) v_1^2 \int_0^\pi q_i(\mathbf{u}_2) \sin \theta \, d\theta \right] dv_1 \equiv w_i Q_i(\mathbf{v}_2) \quad (15)$$

Then, we get

$$\begin{aligned} P_2^{LAB}(\mathbf{v}_2) &= w_1 Q_1(\mathbf{v}_2) + w_2 Q_2(\mathbf{v}_2) + \dots + w_n Q_n(\mathbf{v}_2) \\ &= \sum_i w_i Q_i(\mathbf{v}_2) \end{aligned} \quad (16).$$

Converting  $q_i(\mathbf{u}_2)$  to  $Q_i(\mathbf{v}_2)$  does not change the coefficient  $w_i$ , thus optimizing the LAB system velocity distribution  $P_2^{LAB}(\mathbf{v}_2)$  by fitting with  $\sum_i w_i Q_i(\mathbf{v}_2)$  to obtain  $w_i$ , and applying this to Eq.(12), the CM velocity distribution  $P_2^{CM}(\mathbf{u}_2)$  is obtained.

### 2.2.3 Error evaluation and gradient descent method

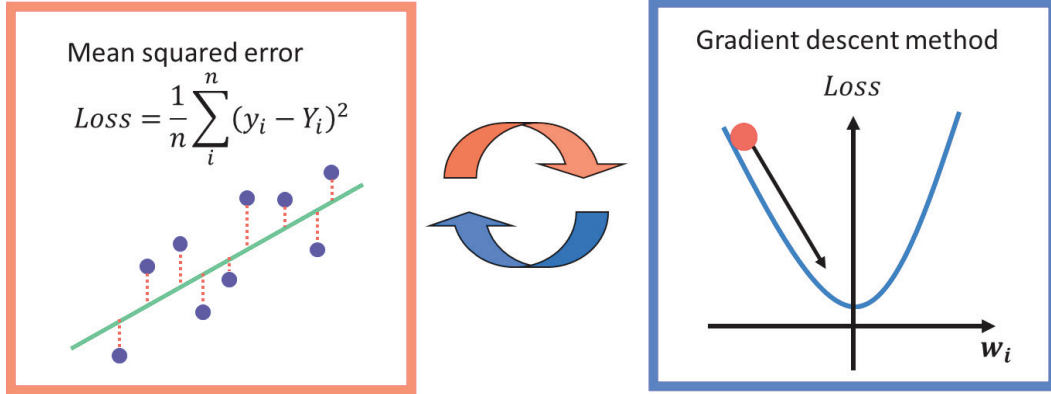


Figure 2-7 The optimization process of  $w_i$ .

Optimization is performed by iterating two steps: evaluating the error by loss function and calculating the error gradient by gradient descent method, and then updating the parameters (Figure 2-7). These methods are used in various situations such as regression analysis and machine learning. There are various methods of loss function, such as mean square error (MSE), root mean square error (RMSE), and coefficient of

determination (R2), but in regression analysis, MSE is treated as the most common loss function. MSE is given by the following equation

$$\text{Loss} = \frac{1}{n} \sum_{i=1}^n (y_i - Y_i)^2 \quad (17)$$

$y_i$  and  $Y_i$  are the  $i$ -th predicted and correct values, respectively. Since the difference is evaluated as a quadratic function, the larger the value deviates from the correct value, the more sensitive the evaluation property is. Based on the evaluated error, the parameters are updated by the gradient descent method. The gradient descent method is an optimization algorithm that minimizes the value of the loss function by calculating the gradient (steepest direction of descent) of the loss function and updating the parameters gradually along that gradient. This method is particularly effective when the loss function has the form of a convex function with respect to the parameters. While there are various methods available for gradient descent, Adam is an optimization method with an adaptive learning rate that combines the advantages of moments and RMSprop for efficient convergence.<sup>11</sup>

#### 2.2.4 Program Environment

Python 3 was used in the analysis. The integrated development environment (IDE) was Google Colaboratory<sup>12</sup>. It is a cloud IDE, so it does not depend on PC specs. It also has many advantages such as free use of graphics processing unit (GPU). However, the calculation itself can be performed in other environments. We used tensorflow/keras to perform multiple regression analysis. keras is a neural network library that can be run on TensorFlow and has a feature that allows you to write code without being aware of the detailed mathematical formulas included in machine learning models<sup>13</sup>.

## 2.3. Model validation

### 2.3.1 Simple fitting model

The model was validated by the model before actually applying it to the experimental data. The figure 2-8 shows the hypothetical velocity distributions  $P_1^{LAB}(v_1)$ ,  $P_2^{CM}(u_2)$  and  $P_2^{LAB}(v_2)$ , where  $P_2^{LAB}(v_2)$  was obtained computationally from Eq. (11). The purpose of this validation is to regressively extract  $P_2^{CM}(u_2)$  from  $P_2^{LAB}(v_2)$  and  $P_1^{LAB}(v_1)$ .

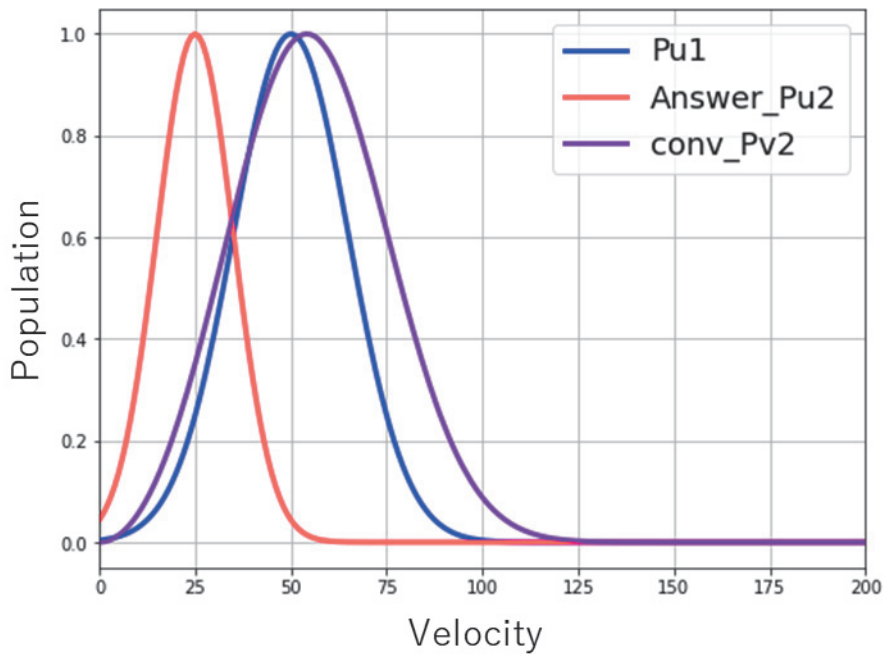


Figure 2-8 Hypothetical velocity distribution. The blue line is  $P_1^{LAB}(v_1)$ , the red line is  $P_2^{CM}(u_2)$ , and the purple line is  $P_2^{LAB}(v_2)$ .

The model was validated through the data processing steps shown in the figure 2-9.

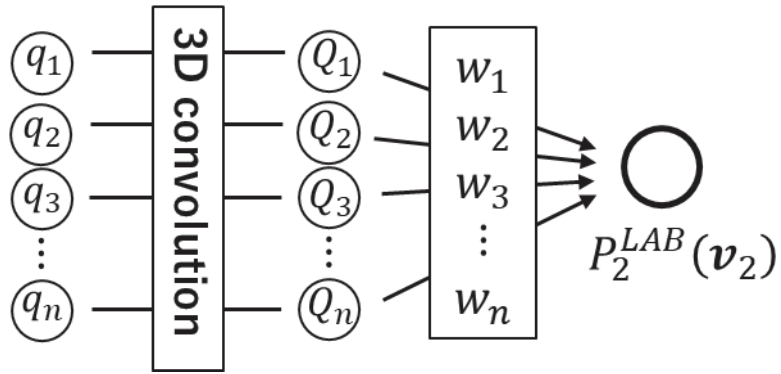


Figure 2-9 Image of data processing process.

First, the function group  $q_i$  applied the following functions.

$$q_i = \begin{cases} 1 & 2i \leq \text{Velocity} < 2i + 2 \\ 0 & \text{else} \end{cases} \quad (18)$$

$$i = 1, 2, 3 \dots 50$$

The following basis function groups  $Q_i$  in the LAB system were created from the summation of discretized numbers based on equation (15), respectively. Figure 2-10 shows some of the results.

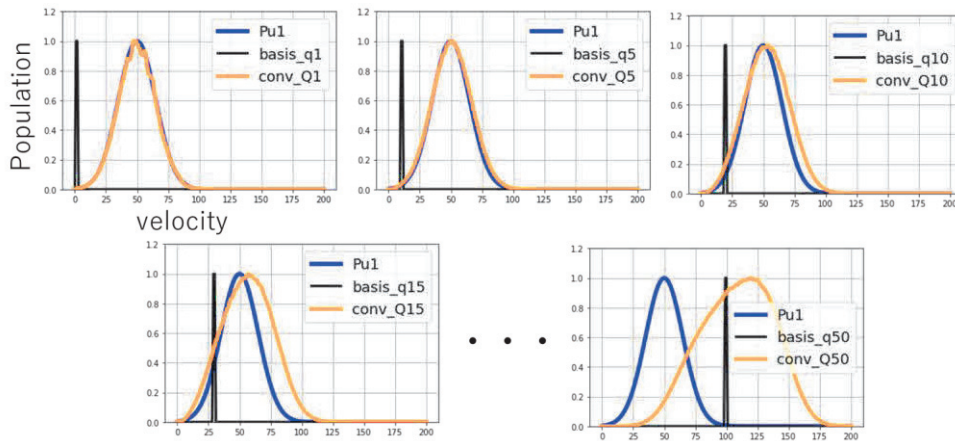


Figure 2-10 Result of converting  $q_i$  to  $Q_i$  using Eq. (15). The black line is  $q_i$ , the blue line is  $P_1^{LAB}(v_1)$ , and the yellow line is  $Q_i$ .

When  $i$  is small, there is a noticeable noise around the peak. This is due to insufficient discretization of the angles. However, since a finer discretization requires more time for

computation, the optimization was performed as is in the introductory stage of the computational model building.

Figure 2-11 shows the results of weight optimization using these weights. However, the weights  $w_i$  are non-negative. The number of parameter updates is fixed at 400.

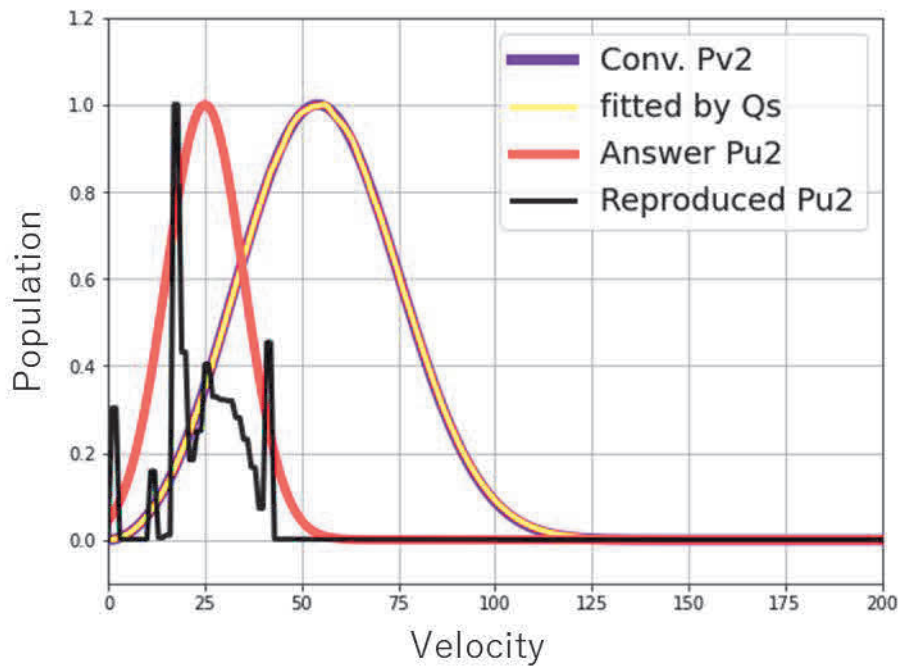


Figure 2-11. Fitting result. The black line is reproduced  $P_2^{CM}(u_2)$  by  $q_i$ , the red line is original  $P_2^{CM}(u_2)$ , the purple line is  $P_2^{LAB}(v_2)$ , and the yellow line is fitted result to  $P_2^{LAB}(v_2)$ .

The results did not reproduce the original distribution. This is because  $Q_i$  and  $Q_{i+1}$  are highly correlated. Therefore, the fitting associated with the initial parameters results in so-called overfitting, which is biased toward one distribution. To avoid overfitting, a common measure is to reduce the complexity of the model or to use regularization techniques to reduce the flexibility of the model, which was examined next.

### 2.3.2 Regularized Model

When the correlation between explanatory variables is large, the weights are biased toward only one of the variables. One way to avoid overfitting due to this multicollinearity is to add a regularization term to the loss function that serves as a penalty term for error evaluation. Ridge regression is a regression analysis method that adds a penalty term to suppress over-learning when explanatory variables are strongly correlated.

The error evaluation function in Ridge regression is as follows

$$Loss = \frac{1}{n} \sum_i^n (y_i - Y_i)^2 + \lambda \sum_i^n w_i^2 \quad (19)$$

The first term on the right-hand side is the loss function, here MSE. The second term is a penalty term called the L2 regularization term.  $\lambda$  is the regularization parameter, the larger this value, the stronger the penalty.  $\sum_i^n w_i^2$  is the sum of squares of the coefficients of the explanatory variables, and the more biased the coefficients are, the greater the penalty. In other words, overfitting can be avoided by suppressing the bias of the coefficients by providing a penalty term as in the above equation. There is also lasso regression, which uses a penalty term based on the sum of the absolute values of the coefficients of the explanatory variables, but this will only be introduced here.

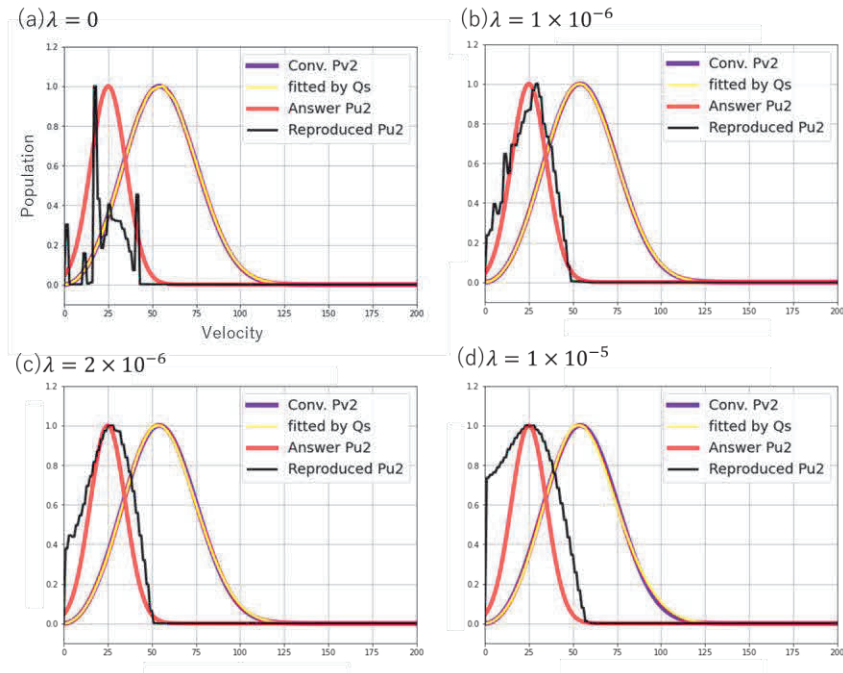


Figure 2-12 Fitting result with Regularized Model. The magnitudes of the penalty term are (a) 0, (b)  $1 \times 10^{-6}$ , (c)  $2 \times 10^{-6}$ , (d)  $1 \times 10^{-5}$ .

Applying the appropriate parameters through ridge regression resulted in a suppression of overlearning, as shown in Figure 2-12. However, if the value of  $\lambda$  is too large, reproduced  $P_2^{CM}(u_2)$  becomes broad, and if the value of  $\lambda$  is too small, reproduced  $P_2^{CM}(u_2)$  becomes overfitting. Therefore reproduced  $P_2^{CM}(u_2)$  becomes somewhat arbitrary.

### 2.3.3 Model with reduced parameters

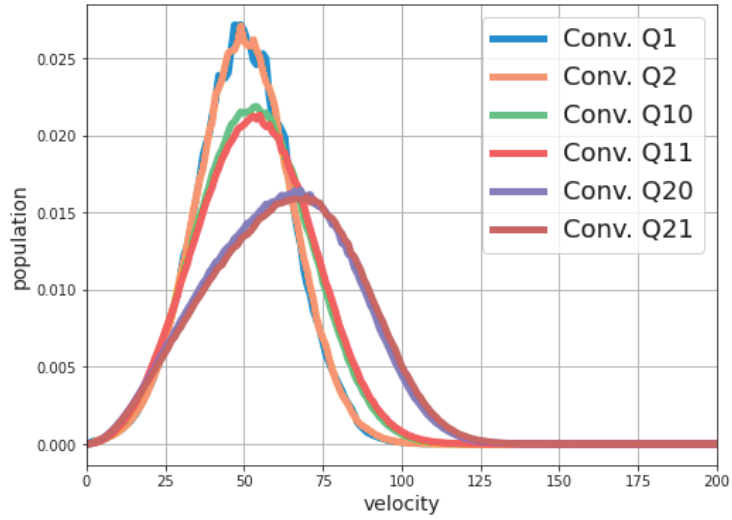


Figure 2-13. Neighboring  $Q_i$  distributions ( $i = 1, 2, 10, 11, 20, 21$ ).

As shown in the figure 2-13, the correlation between neighboring  $Q_i$  and  $Q_{i+1}$  is strong, causing overfitting. Therefore, optimization was performed using 25 parameters where  $i$  is odd ( $i = 1, 3, 5, \dots, 49$ ). The optimization was performed without a penalty term, i.e.,  $\lambda = 0$ .

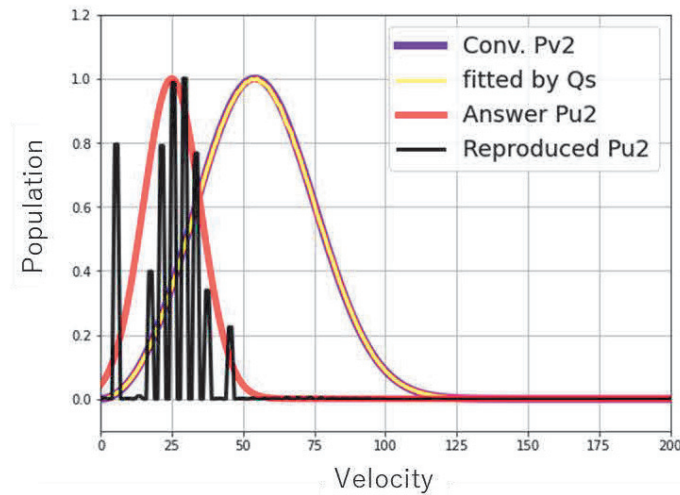


Figure 2-14. Fitting result with reduced parameters model.

The results shown in Figure 2-14 were effective in reducing overfitting. However, on the low speed side, results due to over fitting have been obtained previously.

### 2.3.4. Mixture of regularized model and reduced number of parameters model

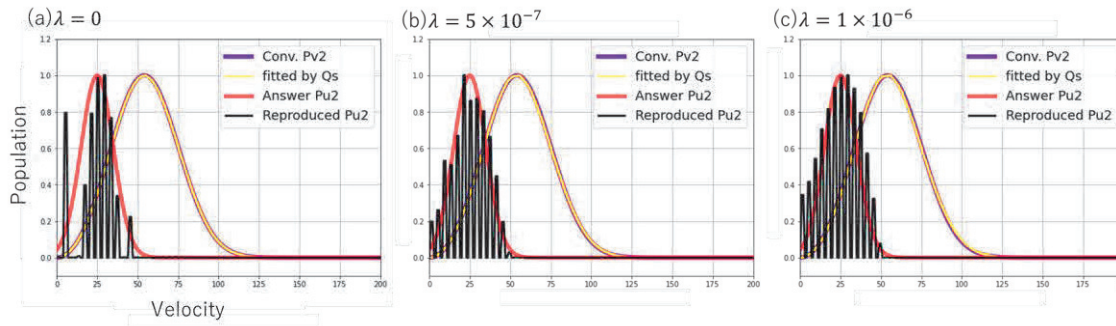


Figure 2-15. Fitting result with mixture of regularized model and reduced number of parameters model. The magnitudes of the penalty term are (a) 0, (b)  $5 \times 10^{-7}$ , (c)  $1 \times 10^{-6}$ .

Fitting was performed by simultaneously applying the model used in 2.3.2 and 2.3.3 with the addition of a penalty term and a reduced number of parameters. The most reproducible results were obtained as shown in Figure 2-15. However, the results were still overestimated at low speeds. Also,  $\lambda$  is arbitrary. Therefore, it is questionable to what extent the results are reproduced when the experimental values are applied.

### 2.3.5 Multiple Outputs Model

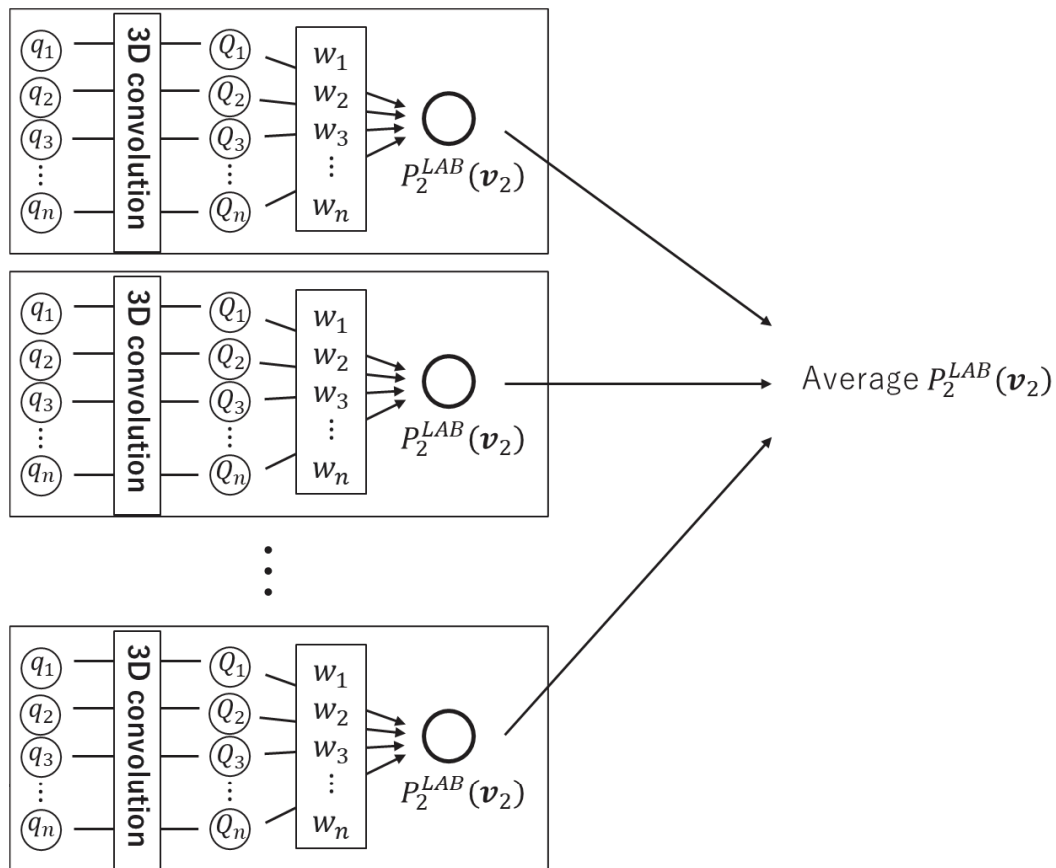


Figure 2-16 Image of data processing process of multiple outputs model.

In optimization processes with complex models and a large number of parameters, inappropriate initial values can lead the optimization process in an unfavorable direction, causing the algorithm to converge to a locally optimal solution rather than the overall optimal solution. Therefore, we studied a model in which the outputs are made numerous and the average value of the outputs is used as the result, so that it does not depend on the initial values. Figure 2-16 shows an image of the data processing.

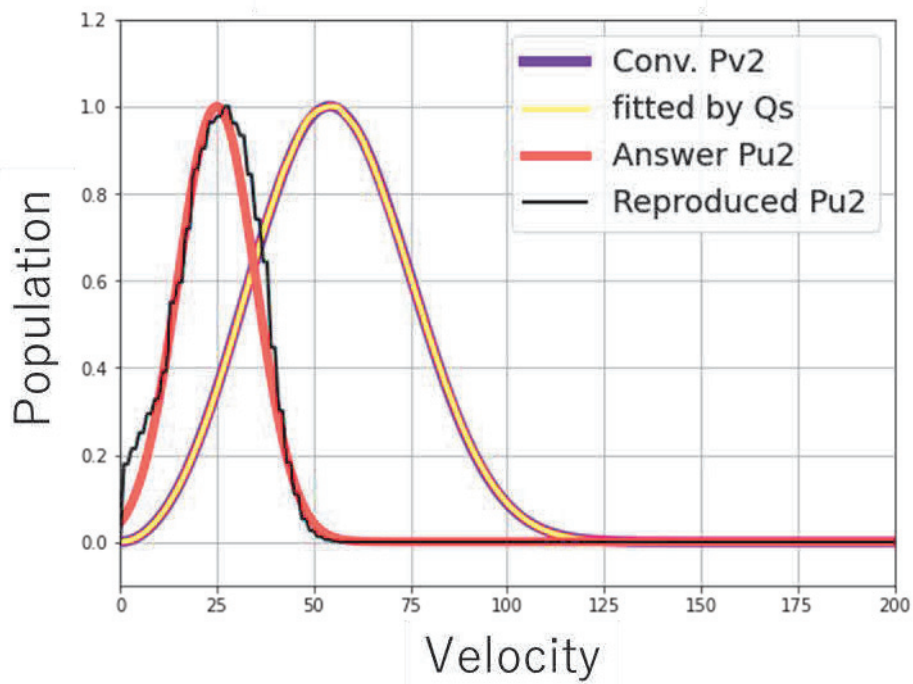


Figure 2-17. Fitting result with Multiple Outputs Model

When the result is the average of the number of 500 outputs, the result of the optimization is as follows. The over fitting result that had plagued us in the past was eliminated. Also, the need to add a penalty term was eliminated, and the optimization could be performed without arbitrary parameters. However, there is still an overestimation on the lower speed side. This is due to the insufficient discretization of the calculation of  $Q_i$ .

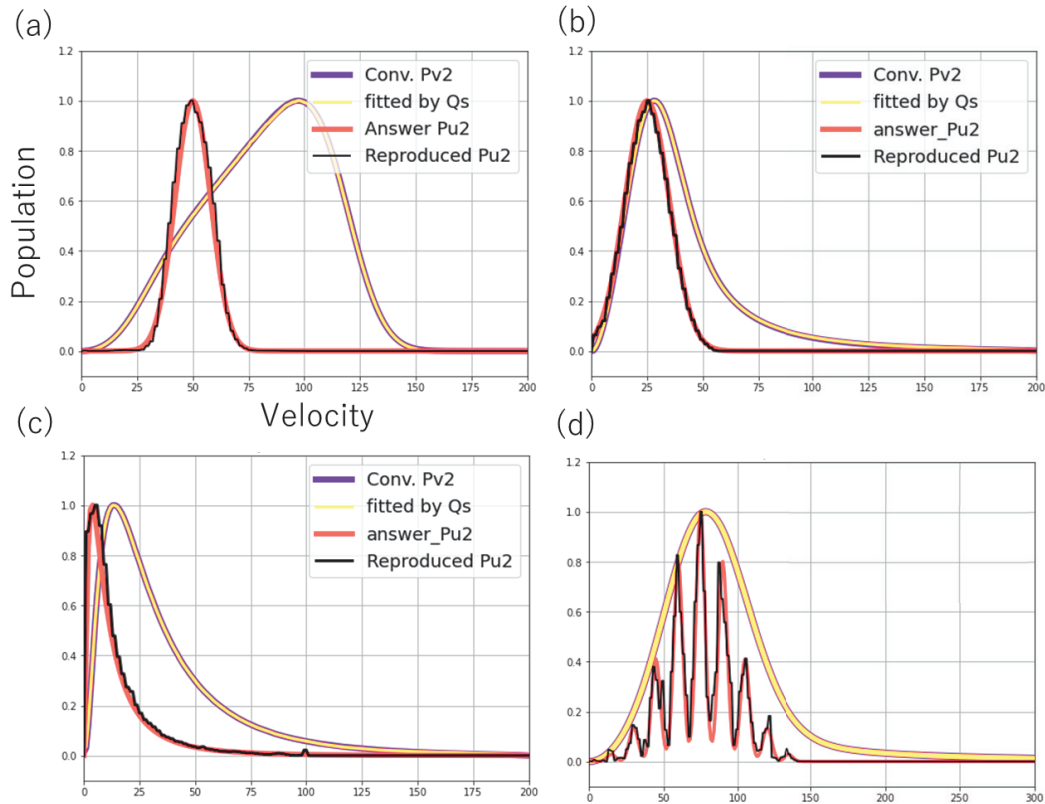


Figure 2-18. Fitting result with Multiple Outputs Model and increased integration accuracy.  $P_2^{LAB}(v_2)$  are generated by convolution of (a)Gauss + Gauss, (b)Lognormal + Gauss, (c) Lognormal + Lognormal, (d)multiple-Gauss + Gauss.

When the discretization performed in the calculation of  $Q_i$  was made finer to increase the accuracy of the calculation, highly reproducible fitting results were obtained. In Figure 2-18(d), however, the number of basis functions was increased from 50 to 100. Although a considerable number of parameter update steps were required, even strictly complex functions could be reproduced for ideal functions without noise.

### 2.3.6 Removal of non-negative restriction on $w_i$

The model so far has been sufficient to reproduce the velocity in the center of mass coordinate system. When considering applying this to experimental data, it is not certain whether the distribution data obtained is insufficient distribution. For example, it

is possible that some of the fragments produced do not energetically reach the ionization threshold by subsequent photoabsorption and do not ionize. An insufficient distribution may appear as a non-physical distribution as a result of the fitting. For example, consider the case where the velocity distribution of the precursor molecule has two components ( $P_1^{LAB}(v_1) = P_{1a}^{LAB}(v_1) + P_{1b}^{LAB}(v_1)$ ). Suppose that each of these dissociates to have a velocity distribution in the CM system of  $P_2^{CM}(u_2)$ . By convolution of these distributions, the velocity distribution in the LAB system of the fragment after dissociation is formed from two components ( $P_2^{LAB}(v_2) = P_{2a}^{LAB}(v_2) + P_{2b}^{LAB}(v_2)$ ). The behavior of  $P_2^{CM}(u_2)$  in

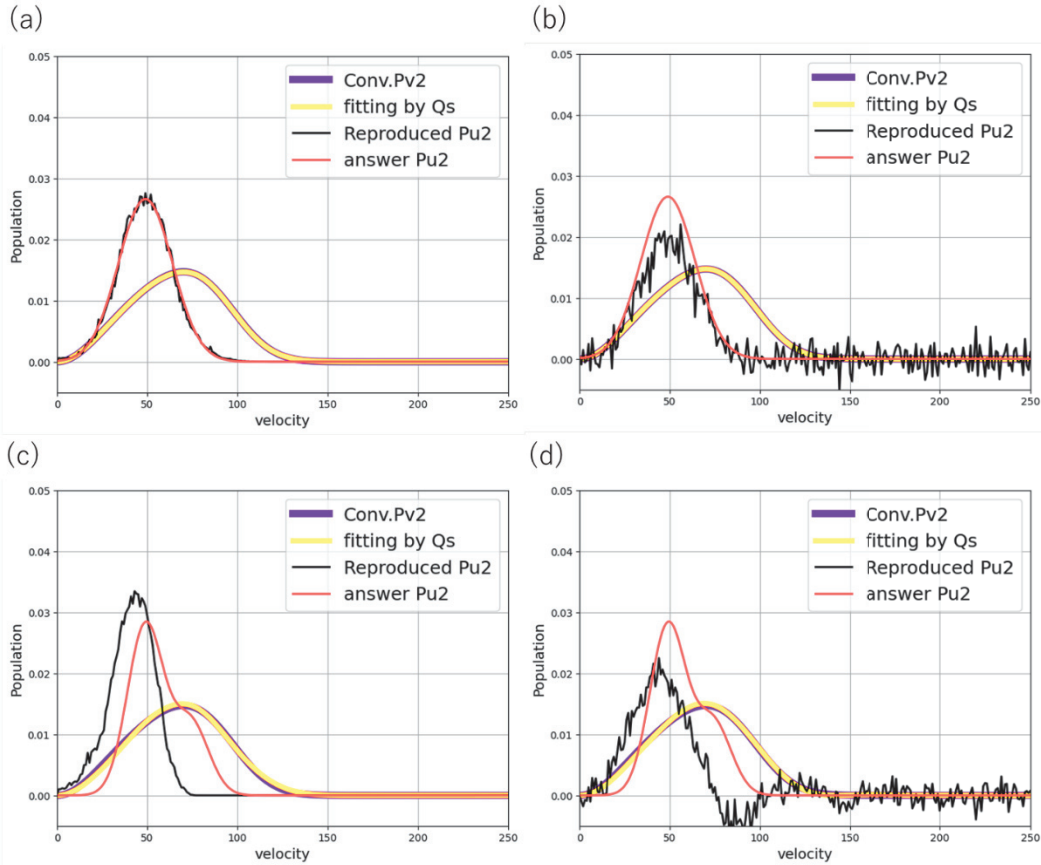


Figure 2-19. Fitting result with removal of non-negative restriction on  $w_i$ . (a) model with non-negative limit on  $w_i$  (b) model without non-negative limit on  $w_i$  (c) model with non-negative limit on  $w_i$  and insufficient  $P_2^{LAB}(v_2)$ , and (d) model with non-negative limit on  $w_i$  and insufficient  $P_2^{LAB}(v_2)$ .

the nonnegative limit of  $w_i$  was examined when the  $P_2^{LAB}(v_2)$  component did not cross the ionization threshold and fitted for an insufficient distribution.

Figure 2-19 shows the fitting results including models with insufficient  $P_2^{LAB}(v_2)$ . When there is no deficiency in the distribution being obtained, it reproduces equally well with or without non-negative restrictions on the weights. Non-negative restrictions on the weights, when there are deficiencies, result in a misperception as if the distribution is obtained correctly. On the other hand, in the absence of nonnegative restrictions, the distribution was unphysical with negative values. This property is a criterion for determining whether the experimental data obtained is insufficient.

### 2.3.7 Censoring of iterative calculations

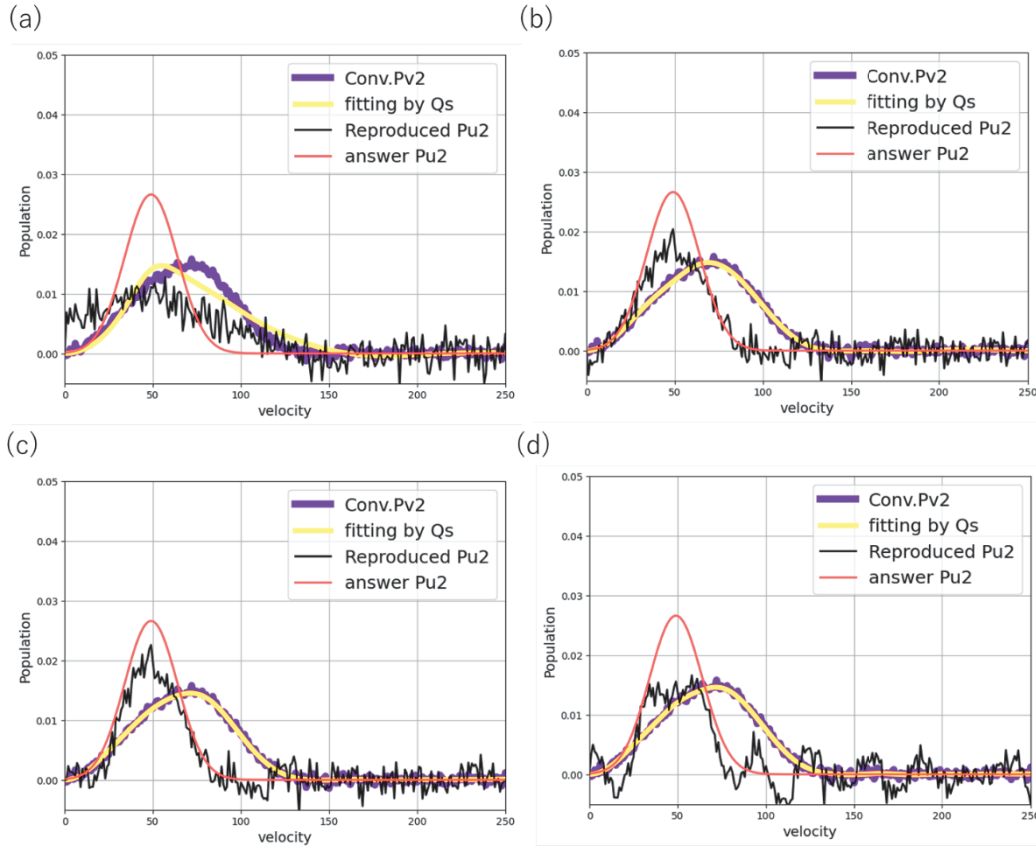


Figure 2-20. Fitting results for (a) 10 times, (b) 100 times, (c) 1000 times and (d) 10000 times iteration.

In the previous calculations, the calculations were performed in the ideal case without noise. Figure 2-20 shows the results of fitting  $P_2^{LAB}(v_2)$  with random noise. Attempts to reproduce up to noise indicate overfitting as the number of calculation steps increases. When applied to experimental data, the number of iterations should be determined based on the model. However, as the number of calculations increases, the amount of change in error decreases exponentially, and hence the degree of structural change in the graph also decreases exponentially.

## References

1. Krupenie PH. The Band Spectrum of Carbon Monoxide. US Govt. Printing Office, Washington: 1966.
2. Wurm S, Feulner P, Menzel D. Resonance-enhanced multiphoton ionization spectroscopy of X(1)Sigma(+) and a (3)Pi carbon monoxide using electron stimulated desorption as a source for rovibronically excited species. *Journal of Chemical Physics* 1996;105(16):6673-6687, doi:10.1063/1.472334
3. MinaCamilde N, Manzanares C, Caballero JF. Molecular constants of carbon monoxide at  $v=0, 1, 2,$  and  $3$  - A vibrational spectroscopy experiment in physical chemistry. *Journal of Chemical Education* 1996;73(8):804-807, doi:10.1021/ed073p804
4. Plyler EK, Blaine LR, Connor WS. VELOCITY OF LIGHT FROM THE MOLECULAR CONSTANTS OF CARBON MONOXIDE. *Journal of the Optical Society of America* 1955;45(2):102-106, doi:10.1364/josa.45.000102
5. Rank DH, Guenther AH, Saksena GD, et al. TERTIARY INTERFEROMETRIC WAVELENGTH STANDARDS FROM MEASUREMENTS ON LINES OF THE 2-0 BAND OF CARBON MONOXIDE AND DERIVED WAVELENGTH STANDARDS FOR SOME LINES OF THE 1-0 BAND OF CARBON MONOXIDE - THE VELOCITY OF LIGHT DERIVED FROM A BAND SPECTRUM METHOD .4. *Journal of the Optical Society of America* 1957;47(8):686-689, doi:10.1364/josa.47.000686
6. Bray RG, Hochstrasser RM. 2-PHOTON ABSORPTION BY ROTATING DIATOMIC-MOLECULES. *Molecular Physics* 1976;31(4):1199-1211, doi:10.1080/00268977600100931
7. Chandler DW, Houston PL. TWO-DIMENSIONAL IMAGING OF STATE-SELECTED PHOTODISSOCIATION PRODUCTS DETECTED BY MULTIPHOTON IONIZATION. *Journal of Chemical Physics* 1987;87(2):1445-1447, doi:10.1063/1.453276
8. Eppink A, Parker DH. Velocity map imaging of ions and electrons using electrostatic lenses: Application in photoelectron and photofragment ion imaging of molecular oxygen. *Review of Scientific Instruments* 1997;68(9):3477-3484, doi:10.1063/1.1148310
9. Sumida M, Masumoto S, Kato M, et al. Internal and Translational Energy Partitioning of the NO Product in the S2 Photodissociation of Methyl Nitrite. *Chemical Physics Letters* 2017;674(58-63, doi:10.1016/j.cplett.2017.02.044
10. Kohge Y, Hanada T, Sumida M, et al. Photodissociation dynamics of nitromethane at 213 nm studied by ion-imaging. *Chemical Physics Letters* 2013;556(49-54, doi:10.1016/j.cplett.2012.11.076
11. Kingma DP, Ba J. Adam: A Method for Stochastic Optimization. In *Proceedings of the*

3rd International Conference for Learning Representations—ICLR 2015, San Diego, CA, USA, 7–9 May 2015

12. Google. Colaboratory: Frequently Asked Questions. <https://research.google.com/colaboratory/faq.html>.
13. François Chollet *et al.*, *Keras*. <https://keras.io/>; 2015.

# Chapter 3

Identification of High- $\nu$  Excited CO Generation Processes  
in the Ultraviolet Photodissociation of  $\text{Fe}(\text{CO})_5$

### 3-1. Introduction

Photolysis of transition-metal carbonyls,  $M(\text{CO})_n$ , efficiently generates coordinatively unsaturated transition-metal carbonyls,  $M(\text{CO})_{n' < n}$ , and CO, both of which serve as important building blocks of stable organometallic complexes in a wide variety of chemical syntheses because of their high reactivity.<sup>1</sup> The major mechanism of photolysis of transition-metal carbonyls is multistep dissociations,<sup>2</sup> where all possible sizes of coordinatively unsaturated complexes ( $M(\text{CO})_{n-1}$ ,  $M(\text{CO})_{n-2}$ , ...) can be generated with their counter-products of CO. One of the most extensively studied transition-metal carbonyls is  $\text{Fe}(\text{CO})_5$  (iron pentacarbonyl),<sup>3</sup> for which  $\text{Fe}(\text{CO})_4$ ,  $\text{Fe}(\text{CO})_3$ , and  $\text{Fe}(\text{CO})_2$  have been detected in gas-phase photodissociation dynamics experiments.<sup>4</sup> The photoabsorption cross sections of the metal-centered (MC) and metal-to-ligand charge transfer (MLCT) transitions of these unsaturated complexes are considered to be as large as that of the  $\text{Fe}(\text{CO})_5$  parent because they have analogous electronic excited state characteristics originating from the d-orbital of the Fe center. Loss of CO can proceed even by photoexcitation to non-dissociative excited states because the dense electronic excited states of the unsaturated carbonyls can easily be converted into a dissociative excited state as well as the  $\text{Fe}(\text{CO})_5$  parent.<sup>5-8</sup> As a result, a mixture of the  $\text{Fe}(\text{CO})_n$  intermediates and CO with different generation origins is formed in pulsed laser photolysis experiments. Photodissociation of the individual unsaturated  $\text{Fe}(\text{CO})_n$  complexes has not been examined selectively in previous experimental studies.

The unsaturated complexes of  $\text{Fe}(\text{CO})_4$ ,  $\text{Fe}(\text{CO})_3$ ,  $\text{Fe}(\text{CO})_2$ , and  $\text{FeCO}$  were identified in the gas-phase photodissociation of  $\text{Fe}(\text{CO})_5$  with time-resolved infrared (TRIR) spectroscopy at the photolysis wavelengths of 193, 266, and 248 nm:  $\text{Fe}(\text{CO})_5 +$

$h\nu \rightarrow \text{Fe}(\text{CO})_4 + \text{CO} \rightarrow \text{Fe}(\text{CO})_3 + 2\text{CO} \rightarrow \text{Fe}(\text{CO})_2 + 3\text{CO}$ .<sup>10,11</sup> The photon energy of 193 nm ( $h\nu = 620 \text{ kJ/mol}$ ) is so close to the energy threshold for eliminating all the carbonyl ligands as internally cold CO that the atomic Fe fragment is unlikely to be generated;  $\text{Fe}(\text{CO})_5 \rightarrow \text{Fe} + 5\text{CO}$ :  $\Delta_r H^\circ = 611 \text{ kJ mol}^{-1}$ .<sup>12-16</sup> In fact, the branching ratio of the Fe atom fragmentation pathways at 193 nm was negligibly small under similar photolysis condition as in TRIR studies.<sup>13,17-19</sup> However, the atomic Fe photofragments were measured at the photodissociation wavelengths of 280 nm and 248 nm (smaller photon energy than 193 nm by 190 kJ/mol and 137 kJ/mol, respectively) with higher photon densities than those used in the TRIR studies.<sup>20,21</sup> These results unambiguously indicated the participation of multiple photons in the  $\text{Fe}(\text{CO})_5$  photodissociation experiments under higher pulse energy condition. The photolysis laser power dependence of the Fe fragment signal illustrated two distinct processes in the  $\text{Fe}(\text{CO})_5$  photolysis: (i) multiple photodissociation (sequential one-photon photodissociations) of the unsaturated complexes and (ii) multiphoton excitation of the parent  $\text{Fe}(\text{CO})_5$  followed by dissociation producing the unsaturated complexes. The latter process can cause ionization of the unsaturated intermediates, linking the neutral and ionic fragmentations.<sup>21</sup> The energetics of the ladder structures associated with CO loss of neutral and ionic unsaturated carbonyls is shown in Figure 3-1.

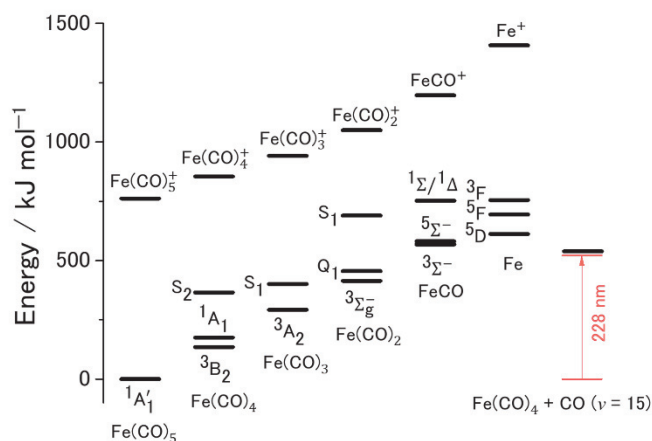


**Figure 3-1.** Energy level diagram of the iron carbonyl species. Low-lying electronic states and ionization potentials for  $\text{Fe}(\text{CO})_{1-5}$  and  $\text{Fe}$  are shown with respect to the ground state of  $\text{Fe}(\text{CO})_5$ . Singlet and quintet states whose electronic terms are unavailable are designated as S and Q, respectively. The photon energy of 228 nm and the energy threshold for  $\text{Fe} + \text{CO}$  ( $\nu = 15$ ) relating to this study are shown for comparison. The numerical data used is summarized in Supporting Information.

The photoabsorption and the subsequent reactions of the coordinatively unsaturated  $\text{Fe}(\text{CO})_n$  intermediates were shown to undergo a “ladder switching” process in the early photodissociation studies, which employed photoionization detection for the transition-metal complexes with nanosecond pulsed lasers.<sup>22-27</sup> The typical result of  $\text{Fe}(\text{CO})_5$  photodissociation was characterized by a dominant signal of the bare  $\text{Fe}^+$  fragment with negligibly small  $\text{Fe}(\text{CO})_n^+$  signals as a result of the sequential photodissociation of the  $\text{Fe}(\text{CO})_n$  intermediates in a single laser pulse with the temporal width of  $\approx 10$  ns. The product mass spectra with the nanosecond laser irradiation, whose photon flux was  $10^{10}$   $\text{W}/\text{cm}^2$  at most, were not ascribed to two-photon absorption of  $\text{Fe}(\text{CO})_5$ , which would be followed by dissociative ionization generating the  $\text{Fe}(\text{CO})_n^+$  signal. These results were contrasted with the product mass pattern in the short-pulse laser

experiments,<sup>26,28</sup> where the  $\text{Fe}(\text{CO})_n^+$  products originating from the multiphoton absorption of  $\text{Fe}(\text{CO})_5$  were dominant. Nanosecond duration is long enough for the  $\text{Fe}(\text{CO})_n$  intermediate generated by the  $\text{Fe}(\text{CO})_5$  photodissociation to absorb another photon, which causes sequential photodissociation. One or two CO fragments are released due to the first one-photon dissociation of  $\text{Fe}(\text{CO})_5$  on the timescale of several ps.<sup>29,30</sup> Then, more CO can be produced due to the sequential photodissociation of  $\text{Fe}(\text{CO})_{n<5}$  in the same nanosecond laser pulse. The CO products and the  $\text{Fe}(\text{CO})_n$  intermediates generated in the concurrent photodissociation could hardly be discerned straightforwardly. Thus, observation of the photodissociation of the individual coordinatively unsaturated  $\text{Fe}(\text{CO})_{n<5}$  complexes has been limited.

Many theoretical studies of  $\text{Fe}(\text{CO})_5$  have been performed to understand the photochemistry. Calculations based on density functional theory (DFT) have been widely applied to the electronic state structures of transition-metal carbonyls including  $\text{Fe}(\text{CO})_5$ , where the accuracy of various functionals was examined.<sup>12,31-41</sup> Comparison of the bond length and the bond dissociation energy of Fe–CO in unsaturated  $\text{Fe}(\text{CO})_{n<5}$  complexes between the different calculation methods demonstrated the validity of the DFT calculation for  $\text{Fe}(\text{CO})_n$ . The electronic excited states of  $\text{Fe}(\text{CO})_5$  and  $\text{Fe}(\text{CO})_4$  were recently characterized in detail on the basis of coupled-cluster response theory in a comprehensive study by Malcomson et al., who presented the two-photon absorption cross sections ( $\sigma^{\text{TPA}}$ ) as well as the one-photon absorption spectra.<sup>42</sup> Most of the bright states of both  $\text{Fe}(\text{CO})_4$  and  $\text{Fe}(\text{CO})_5$  were identified as the MLCT ( $\pi^*_{\text{CO}} - \text{d}$ ) states. The excited states with a large oscillator strength of  $\text{Fe}(\text{CO})_5$  were further assigned to the MLCT ( $\pi^*_{\text{axial CO}} - \text{d}$ ) and MLCT( $\pi^*_{\text{equatorial CO}} - \text{d}$ ) states, which reproduce well two overlapped peaks of the experimental absorption spectrum.<sup>43</sup> Figure 3-2 shows the UV-

Vis absorption spectra of  $\text{Fe}(\text{CO})_5$ . The theoretical photoabsorption of  $\text{Fe}(\text{CO})_4$  in the

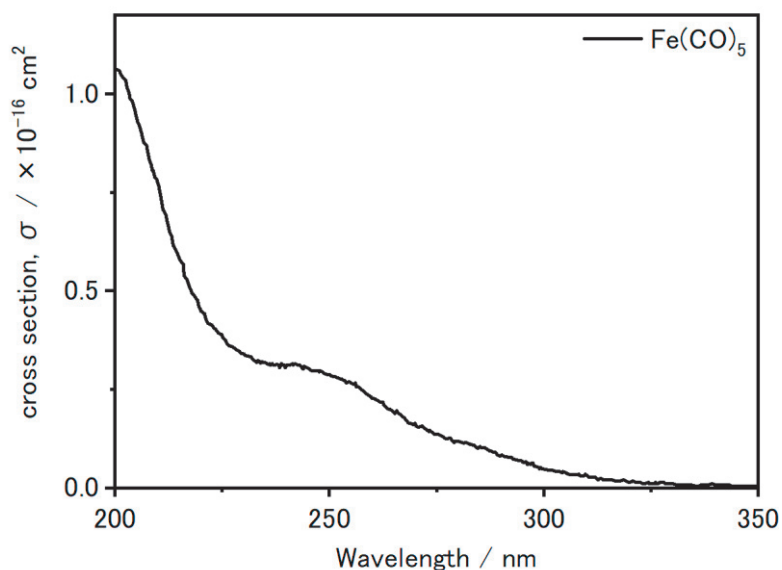


**Figure 3-2.** Absorption spectra of  $\text{Fe}(\text{CO})_5$ .

200–300 nm region was comparably strong as that of  $\text{Fe}(\text{CO})_5$  in the 200–240 nm region:  $\sigma_{\text{abs}}(\text{Fe}(\text{CO})_4) = 4.6 \times 10^{-17} \text{ cm}^2$  at 270 nm and  $\sigma_{\text{abs}}(\text{Fe}(\text{CO})_5) = 6.9 \times 10^{-17} \text{ cm}^2$  at 220 nm. The spectral overlap of  $\text{Fe}(\text{CO})_5$  and  $\text{Fe}(\text{CO})_4$  was proposed as a possible source of the sequential photodissociation of the  $\text{Fe}(\text{CO})_4$  intermediates, which was indicated in the previous photodissociation experiments. The electronic excited states of the smaller unsaturated  $\text{Fe}(\text{CO})_n$  ( $n = 1-3$ ) are so far less investigated than  $\text{Fe}(\text{CO})_4$  and  $\text{Fe}(\text{CO})_5$ . A simple extension of the photochemistry of the larger iron carbonyls to the smaller ones provides an expectation that the  $\text{Fe}(\text{CO})_{n<4}$  complexes have strong MLCT absorption bands in the ultraviolet region causing CO loss. Although the final outcome involving various elementary processes has been experimentally presented in the results of previous  $\text{Fe}(\text{CO})_5$  photodissociation studies, the reaction mechanism of an individual  $\text{Fe}(\text{CO})_n + h\nu \rightarrow \text{Fe}(\text{CO})_{n-m} + m\text{CO}$  photodissociation is not known in detail.

The CO fragments can be a probe for elucidating the reaction mechanisms in the  $\text{Fe}(\text{CO})_5$  photodissociation, especially when the rovibrational state-resolved

measurement is applied. Waller and Hepburn measured the vacuum ultraviolet laser-induced fluorescence (VUV-LIF) spectra of the CO fragments at the photolysis wavelengths of 193, 248, 266, and 351 nm under one-photon absorption conditions.<sup>18</sup> The one-photon LIF detection scheme was advantageous for the low pulse energy photolysis, by which photodissociation of the  $\text{Fe}(\text{CO})_n$  intermediates in a single nanosecond laser pulse was suppressed. The statistical state distributions of the CO fragments were explained as the results of sequential dissociation mediated with the spin triplet electronic states.<sup>18</sup> Recent time-resolved photoelectron spectroscopy and TRIR spectroscopy studies support the fast dissociation of  $\text{Fe}(\text{CO})_5 + h\nu$  (266 nm)  $\rightarrow$   $\text{Fe}(\text{CO})_4 + \text{CO}$  within 100 fs in the singlet excited state<sup>7,29</sup>; subsequent dissociations of  $\text{Fe}(\text{CO})_4$  producing the CO fragments were indicated to also be so fast that intersystem crossing could not occur.<sup>6</sup> Whereas several experimental approaches have been thus conducted for the one-photon dissociation of  $\text{Fe}(\text{CO})_5$ , photodissociation of unsaturated intermediates, which have comparably large photoabsorption cross sections, is not fully investigated. The photoexcited  $\text{Fe}(\text{CO})_n$  intermediates are expected to release highly vibrationally excited CO ligands due to the large amount of available energy (Figure 3-1). The individual CO dissociation step of the  $\text{Fe}(\text{CO})_n$  intermediate can be identified based on internal state and translational energy distributions. In the present study, we applied state-resolved ion-imaging to the  $\text{Fe}(\text{CO})_5$  photodissociation to distinguish the dissociations of the unsaturated intermediates in the whole CO releases.

### 3-2. Experimental

The experiments were performed using a standard velocity-map imaging (VMI) apparatus, which consists of a supersonic molecular beam source and an ion-imaging system with a time-of-flight (TOF) mass spectrometer. The details of the experimental

setup are described elsewhere.<sup>44,45</sup> Liquid Fe(CO)<sub>5</sub> (Kanto Chemical, >95%) was used without further purification. The Fe(CO)<sub>5</sub> vapor was diluted in a He buffer to prepare a 0.25% Fe(CO)<sub>5</sub> mixture gas. The gas sample was supersonically expanded into vacuum through a piezoelectric pulsed valve at a stagnation pressure of 2 bar. The Fe(CO)<sub>5</sub> molecular beam was skimmed (1.5 mm in diameter) before entering an ion-imaging detector chamber. The inner pressures of the source and detector chambers were  $3 \times 10^{-6}$  Torr and  $1 \times 10^{-7}$  Torr, respectively, when the pulsed molecular beam was injected with a repetition rate of 10 Hz. The molecular beam was perpendicularly intersected by a loosely focused laser beam between the VMI electrode plates. The laser beam was generated using a frequency-doubled tunable dye laser (CobraStretch, Spectra Physics) pumped by the third harmonic of a Nd:YAG laser (LAB-170, Spectra Physics). We tuned the laser wavelengths in the 213–235 nm region, which was responsible both for the strong MLCT photoabsorption of Fe(CO)<sub>5</sub> and for the resonantly-enhanced multiphoton ionization (REMPI) of CO. The pump (photolysis) and probe (ionization detection) were carried out in a single laser pulse, whose temporal duration was approximately 10 ns. The pulse energy in the measurements was kept at 20  $\mu$ J/pulse. The peak intensity was evaluated to be  $2 \times 10^7$  W/cm<sup>2</sup> at most on the basis of a beam size of 0.1 mm  $\times$  0.1 mm. We chose the pulse energy condition so that the sequential photodissociations of the Fe(CO)<sub>n</sub> intermediates and the non-resonant ionization occur in a single nanosecond pulse.<sup>19,21,25,26</sup> The resultant Fe(CO)<sub>n</sub><sup>+</sup> signal was a few orders of magnitude smaller than the Fe<sup>+</sup> signal, which was consistent with the previous study.<sup>25</sup>

The CO fragments in the  $\nu = 0$  and 1 vibrational states were ionized by the [2 + 1] REMPI scheme via the  $\tilde{B}_{\square}^1\Sigma - \tilde{X}_{\square}^1\Sigma$  transition at around 230 nm. The high- $\nu$  states ( $\nu = 11$ –15) of the CO fragments were detected by the [1 + 1] REMPI scheme via the

$\tilde{A}^1\Pi - \tilde{X}^1\Sigma^+$  transition in the wavelength region from 213 to 230 nm.<sup>46,47</sup> The coordinatively unsaturated  $\text{Fe}(\text{CO})_n$  ( $n = 1-4$ ) complexes, which are counter-products of the CO photofragments, were non-resonantly ionized. The ions accelerated by a static electric field were mass-selectively detected using a microchannel plate (MCP) detector with a phosphor screen in the back. The positions of the light spots on the phosphor screen were recorded using a CCD camera (Hamamatsu C8800) to obtain the ion images. The intensity of light emitted from the phosphor screen was acquired by a photomultiplier tube (R2496, Hamamatsu) for the TOF and REMPI spectra. The observed images, which were two-dimensional projections of the scattering distributions, were converted to the kinetic energy release distributions and the angular distributions using the inverse Abel transformation. The velocity scale of the CO images was calibrated using photodissociation/ionization measurements of OCS molecules, whose bond dissociation energy to CO + S is well known.<sup>48</sup> The velocity scale of  $\text{Fe}(\text{CO})_n$  was calculated as a square-root mass-weighted velocity of the CO fragment ( $v_{\text{CO}}$ ),  $v(\text{Fe}(\text{CO})_n) = \sqrt{m_{\text{CO}}/m_{\text{Fe}(\text{CO})_n}} v_{\text{CO}}$ .

We performed quantum chemistry calculations for the vertical transition energy of FeCO and  $\text{Fe}(\text{CO})_2$  to obtain the photoabsorption spectra using the Gaussian 16 package.<sup>49</sup> The geometry of the electronic ground state was optimized using DFT with the B3LYP functional and the TZVP basis functions. The absorption cross section simulations were performed for the optimized geometries using time-dependent (TD) DFT with the B3LYP functional. Although both FeCO and  $\text{Fe}(\text{CO})_2$  have a triplet ( $^3\Sigma^-$  and  $^3\Sigma_g^-$ , respectively) electronic ground state, which were confirmed by high-resolution spectroscopy,<sup>50-52</sup> the nascent spin states of the FeCO and  $\text{Fe}(\text{CO})_2$  intermediates produced in the  $\text{Fe}(\text{CO})_5$  photodissociation are not experimentally established so far. We

simulated the photoabsorption spectra of FeCO and Fe(CO)<sub>2</sub> assuming independently three possible spin multiplicities (singlet, triplet, and quintet). The electronic transitions and the reactivity of the photoinitiated excited states were qualitatively characterized on the basis of the calculated orbitals relevant to the photoabsorption bands. Our theoretical approaches are based on the previous DFT studies for Fe(CO)<sub>5</sub>, Fe(CO)<sub>4</sub>, and other transition-metal carbonyls.<sup>12,35-38,40,53</sup>

### 3-3. Results and Discussion

#### 3-3-1. REMPI spectrum of CO fragments in vibrational state $\nu=0,1$

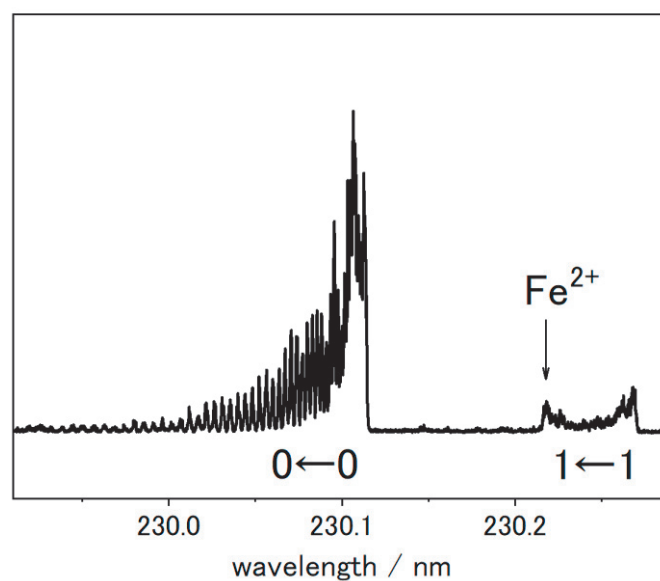


**Figure 3-3.**  $\tilde{B}_{\square}^1\Sigma - \tilde{X}_{\square}^1\Sigma$  REMPI spectrum of the CO fragment in the Fe(CO)<sub>5</sub> photolysis.

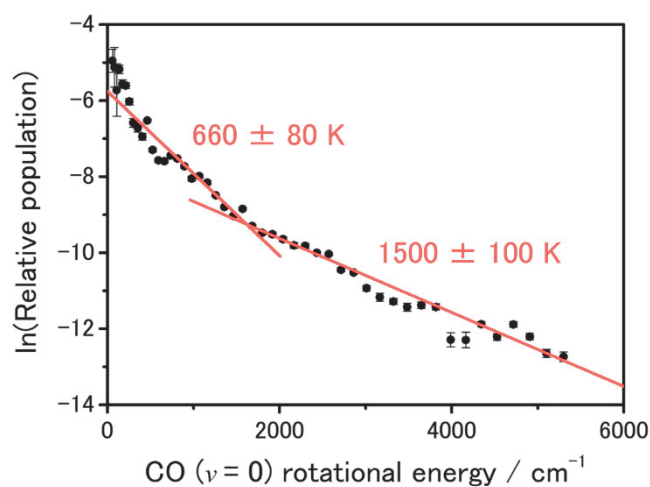


**Figure 3-4.** Boltzmann plot of the rotational state distribution of CO ( $v = 0$ ) fragment. The rotational state population are obtained by correcting the rotational line intensities of the 0–0 band with the Hönl-London factor.

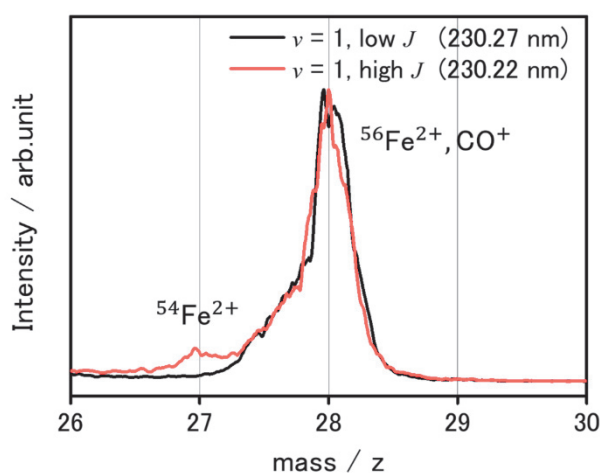


**Figure 3-5.** TOF-mass spectra of the photofragments in the  $\text{Fe}(\text{CO})_5$  photodissociation at the photolysis wavelengths of 230.27 nm (black curve) and 230.22 nm (red curve). The wavelengths of 230.27 nm and 230.22 nm correspond to the low rotational and high rotational transition regions of the [2 + 1] REMPI spectra via the  $\tilde{\text{B}}_0^1\Sigma - \tilde{\text{X}}_0^1\Sigma, v' = 0, v'' = 1$  band, respectively.

The  $[2 + 1] \tilde{B}^1\Sigma - \tilde{X}^1\Sigma$  REMPI spectrum of CO fragments, which were assigned to Q-branches of the 0–0 and 1–1 vibronic bands, is shown in Figure 3-3. Although the population analysis (Figure 3-4) remains qualitative partly because of the short lifetime of the  $\tilde{B}^1\Sigma$  state, the Boltzmann plot is similar to the previous results by Waller and Hepburn in that multiple temperature components are involved; the temperature components of the CO fragments varied with the photolysis wavelengths: (1926 K, 1429 K, and 427 K) at 193 nm and (1716 K, 1162 K, and 340 K) at 248 nm.<sup>18</sup> Two temperatures, 660 K for the lower rotational states ( $E_{\text{rot}} < 1800 \text{ cm}^{-1}$ ) and 1500 K for the higher rotational states ( $E_{\text{rot}} > 1800 \text{ cm}^{-1}$ ), are well fitted to the present plot at the photolysis wavelength of 230 nm. The result of the rotational state distribution of CO based on the REMPI detection scheme is consistent with the previous data obtained by VUV-LIF spectroscopy. The small peak in the higher  $J$  transition region of the 1–1 band at 230.22 nm was assigned to the resonant ionization of Fe via the  $^5F_1^o(\text{Fe}) - ^4P_{5/2}(\text{Fe}^+)$  transition generating  $\text{Fe}^{2+}$ , whose  $m/z$  is identical to that of  $\text{CO}^+$  ( $m/z = 28$ ). The assignment was confirmed by measurement of the corresponding peaks of the  $^{54}\text{Fe}$  and  $^{56}\text{Fe}$  isotopologues (Figure 3-5). Ionization at 230.22 nm yielded both peaks for  $m/z = 28$  ( $\text{CO}^+$  and  $^{56}\text{Fe}^{2+}$ ) and at  $m/z = 27$  ( $^{54}\text{Fe}^{2+}$ ). The relative intensity between  $m/z = 28$  and 27 was explained as the natural abundance of  $^{56}\text{Fe}$  (91.8%) and  $^{54}\text{Fe}$  (5.8%) isotopologues, indicating the resonant ionization of Fe at 230.22 nm. The peak at  $m/z = 27$  disappeared at 230.27 nm, which is off-resonant for Fe but on-resonant for CO. Thus, the prominent peak in the high  $J$  region of the REMPI spectra measured for  $m/z = 28$  (Figure 3-3) is assigned to  $\text{Fe}^{2+}$ .

### 3-3-2. REMPI spectrum of CO fragments in vibrational state $v \geq 11$

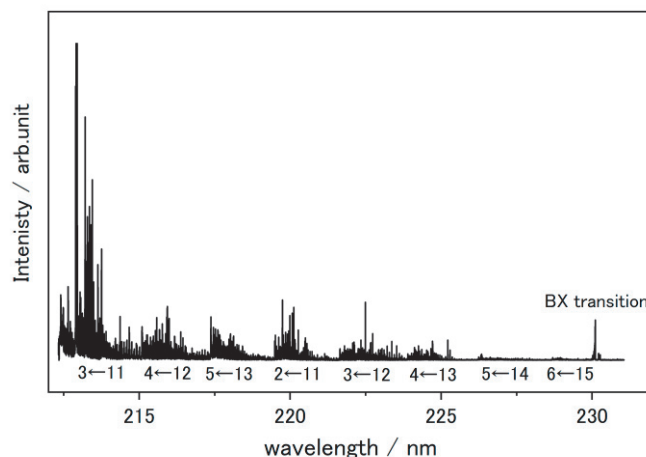


**Figure 3-6.** REMPI spectrum of the CO fragment in the  $\text{Fe}(\text{CO})_5$  photolysis. The vibrational band assignments for the  $\tilde{\text{A}}^1\Pi - \tilde{\text{X}}^1\Sigma^+$  transition are shown below the baseline.

We scanned the laser wavelength over a wide range of 213–235 nm, which corresponds to the MLCT transition of  $\text{Fe}(\text{CO})_5$ , to measure the REMPI spectrum of the CO fragments in a one-color scheme. Eight nearly equally spaced bands with highly rotationally excited structures with  $J$  up to  $\approx 40$  were observed, as shown in Figure 3-6. The weak bands at around 230 nm are the 0–0 and 1–1 bands of the  $[2 + 1] \tilde{\text{B}}^1\Sigma - \tilde{\text{X}}^1\Sigma$  transition. The other prominent bands in the shorter wavelength region were assigned to the  $[1 + 1] \tilde{\text{A}}^1\Pi - \tilde{\text{X}}^1\Sigma^+$  transition of the highly vibrationally excited states ( $v = 11$  to 15) on the basis of the literature.<sup>46,47</sup> The observed vibrational structures comprised two sequences: group A with  $\Delta v = -9$  (2–11, 3–12, 4–13, 5–14, and 6–15) and group B with  $\Delta v = -8$  (3–11, 4–12, and 5–13), in which three pairs with the common lower states ( $v'' = 11, 12$  and 13) were found. These high- $v$  bands exhibited qualitatively similar rotational distributions, indicating an identical production mechanism. We confirmed that the

efficient CO generation in the extremely high- $\nu$  states was peculiar to  $\text{Fe}(\text{CO})_5$  by comparing the results for  $\text{Cr}(\text{CO})_6$  and  $\text{CoC}_5\text{H}_5(\text{CO})_2$  under the same measurement condition.

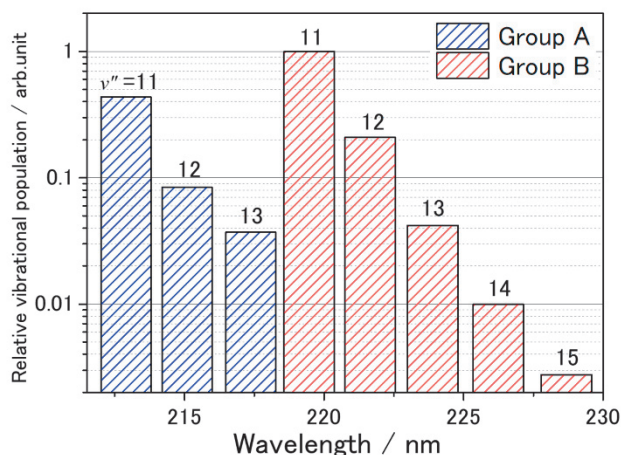


**Figure 3-7.** Vibrational state populations of the CO fragments with respect to the photolysis/ionization wavelength. The relative vibrational populations obtained from the  $\Delta\nu = -8$  sequence bands ( $\nu' - \nu'' = 3-11$ ,  $4-12$ , and  $5-13$ ) and the  $\Delta\nu = -9$  sequence bands ( $\nu' - \nu'' = 2-11$ ,  $3-12$ ,  $4-13$ ,  $5-14$ , and  $6-15$ ) are shown as Group A (blue shaded) and Group B (red shaded), respectively.

The vibrational state populations of the CO products determined from the vibrational band intensity corrected with the Franck–Condon factors<sup>47</sup> are shown in Figure 3-7. Although the photolysis wavelength dependence of the vibrational state distribution is not accurately obtained in the one-color scheme, a comparison of the band intensities in neighboring wavelength segments can give an approximate variation. Groups A and B have a common set of the lower  $\nu''$  states ( $\nu'' = 11, 12, 13$ ) but they are located in different photolysis wavelength regions. The relative intensities of the  $\nu'' = 11, 12, 13$  states in each group A and B were approximately matched, but the populations in group B were more than two times larger than group A, as is shown in Figure 3-7. On the

other hand, the photoabsorption of  $\text{Fe}(\text{CO})_5$  sharply increases from the group B region (219–225 nm) to the group A region (213–218 nm).<sup>43</sup> The wavelength dependences of the photoabsorption and the population ratio between the groups A and B indicate that the high- $\nu$  CO fragment is not directly generated from the  $\text{Fe}(\text{CO})_5$  parent molecule. We ascribe generation of the high- $\nu$  CO products to photodissociation of some coordinatively unsaturated intermediate:  $\text{Fe}(\text{CO})_x + h\nu \rightarrow \text{Fe}(\text{CO})_{x-1} + \text{CO} (\text{high-}\nu)$ , where  $\text{Fe}(\text{CO})_x$  is prepared by the first photodissociation of  $\text{Fe}(\text{CO})_5$  in the same laser pulse. Participation of the second or the subsequent photon under the present experimental condition is supported by the detection of the CO ( $\nu = 15$ ) fragment and the atomic Fe fragments, both of which are energetically inhibited by one-photon dissociation of  $\text{Fe}(\text{CO})_5$  (Figure 3-1). The increase of the CO ( $\nu = 11$  and 12) production in the group B region (219–225 nm) compared with the group A region (213–218 nm) with a similar population of the  $\nu = 13$  state at 218 nm and 224 nm (Figure 3-7) can be explained assuming that the absorption cross section of the relevant coordinatively unsaturated intermediate is maximized at around 225 nm. The assumption will be examined below with additional experimental and theoretical results.

### 3-3-3. Photolysis wavelength dependence of the $\text{Fe}(\text{CO})_n^+$ yield

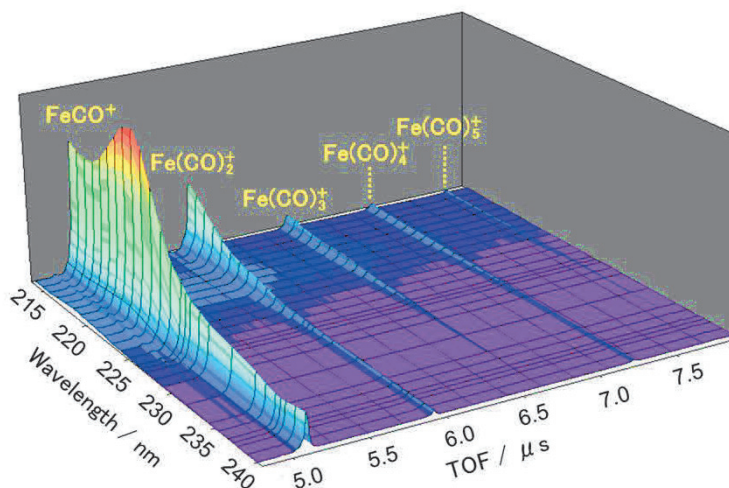


**Figure 3-8.** Photolysis yield spectra of  $\text{Fe}(\text{CO})_n^+$  in the ultraviolet irradiation of  $\text{Fe}(\text{CO})_5$ . Variation of the peak intensities of the TOF spectra for  $m/z = 84\text{--}196$  ( $\text{Fe}(\text{CO})_{n=1-5}$ ) are displayed with respect to the photolysis wavelength. The photolysis wavelength are varied in steps of 1 nm from 213 nm to 240 nm in the measurements.

The photolysis wavelength dependence of the  $\text{Fe}(\text{CO})_n^+$  yield, which was obtained by merging the TOF mass spectra measured at different wavelengths incremented by 1 nm, is shown in Figure 3-8. We considered that the photoabsorption of the  $\text{Fe}(\text{CO})_n$  intermediates appears in the wavelength dependence of the TOF mass spectra. The unsaturated  $\text{Fe}(\text{CO})_{n<5}$  complexes that are first generated by the  $\text{Fe}(\text{CO})_5$  photodissociation are likely to be internally excited, so that another photoabsorption in the single laser pulse can cause ionization, giving the ion yield spectra in Figure 3-8. Although the yield of  $\text{Fe}(\text{CO})_n$  and the ionization efficiency can also depend on the wavelength, their dependence is generally a monotonic increase as the wavelength shortens. The increasing intensities of  $\text{Fe}(\text{CO})_5^+$ ,  $\text{Fe}(\text{CO})_4^+$ , and  $\text{Fe}(\text{CO})_3^+$  in the shorter wavelength toward 210 nm is regarded as the ionization efficiency curve. In addition to the increasing yield curve, the  $\text{FeCO}^+$  yield spectrum exhibited a prominent peak at

around 220 nm, which we ascribed to the photoabsorption band of FeCO. The peak position of the FeCO<sup>+</sup> yield spectrum was coincident with the wavelength region for enhanced generation of the high- $\nu$  CO fragments, which was estimated from the wavelength dependence of the vibrational population (Figure 3-7). The coincidence indicates that the resonant photoexcitation of FeCO is responsible for both the high- $\nu$  CO formation ( $\text{FeCO} + h\nu \rightarrow \text{Fe} + \text{CO} (\text{high-}\nu)$ ) and ionization ( $\text{FeCO} + h\nu \rightarrow \text{FeCO}^+ + e^-$ ). Dissociative ionization of the larger carbonyls ( $\text{Fe}(\text{CO})_{n>1}^+ \rightarrow \text{Fe}(\text{CO})_{n-1}^+ + \text{CO}$ ) could contribute to the FeCO<sup>+</sup> signal in different ways from our interpretation. However, because the peak (resonance) structure in the yield spectrum was observed only in FeCO<sup>+</sup>, the spectral peak at around 220 nm is less likely to be assigned to any photoabsorption bands of Fe(CO)<sub>2</sub>, Fe(CO)<sub>3</sub>, and Fe(CO)<sub>4</sub>.

### 3-3-4. Verification by theoretical calculations of specific distributions

To ascertain the origin of the correlation between the high- $\nu$  CO generation and the FeCO<sup>+</sup> yield spectral peak at  $\approx 220$  nm, we executed theoretical calculations for FeCO and Fe(CO)<sub>2</sub>. The calculated low-lying electronic structures and the coordination geometries were first compared with the experimental and previous theoretical results to confirm the accuracy of our calculations. The FeCO molecule has low-lying electronic states with different spin multiplicities ( ${}^5\Sigma^-$  and  ${}^3\Sigma^-$ ), of which the triplet state is the ground state.<sup>50,51,54-56</sup> The energy gap between the  $\tilde{X}{}^3\Sigma^-$  and  $\tilde{a}{}^5\Sigma^-$  states was experimentally determined as 1135 cm<sup>-1</sup> by Villalta and Leopold.<sup>55</sup> We optimized the FeCO geometry in the lowest singlet, triplet and quintet states and calculated the energy gaps of the spin states at the optimized structure. The results are summarized in Table 3-1. The optimized structural parameters were in good agreement with the previous study.<sup>56</sup>

Method	Spin state	$T_e$ (eV)	$r_e(\text{Fe-C})$ (Å)	$r_e(\text{C-O})$ (Å)
<i>This study</i>				
	Triplet	0	1.766	1.152
B3LYP/TZVP	Quintet	0.14	1.901	1.148
	Singlet	1.65	1.694	1.154
<hr/> <i>Experimental</i>				
Photoelectron <sup>1)</sup>	$^5\Sigma^-$	0.14	--	--
IR (diode laser) <sup>2)</sup>	$^3\Sigma^-$	--	1.727	1.159
<hr/> <i>Theoretical</i>				
	$^3\Sigma^-$	--	--	--
SOCI/cc-pVTZ <sup>3)</sup>	$^5\Sigma^-$	0.04	--	--
	$^1\Sigma/{}^1\Delta$	1.91	--	--

**Table 3-1.** Calculated results for term energies and optimized structures of Fe(CO).<sup>1)</sup> Reference 54. <sup>2)</sup> Reference 50. <sup>3)</sup> Reference 56.

The experimental  $\tilde{X}^3\Sigma^- - \tilde{a}^5\Sigma^-$  energy gap was well reproduced by our calculation (1160  $\text{cm}^{-1}$ ). The singlet state is not experimentally corroborated but was theoretically predicted to be located at 15 400  $\text{cm}^{-1}$  above the  $\tilde{X}^3\Sigma^-$  state,<sup>57</sup> for which we obtained a similar singlet-triplet energy interval of 13 300  $\text{cm}^{-1}$ . The electronic term was denoted as  ${}^1\Sigma/{}^1\Delta$ , since it was not uniquely identified. The results of the comparison between our calculations and the previous studies indicate that the present calculation method is valid for the electronic properties of FeCO. Then, we applied the theoretical approach to the spectral simulation. The calculated oscillator strength of FeCO from the  $\tilde{X}^3\Sigma^-$ ,  $\tilde{a}^5\Sigma^-$ ,

and the lowest singlet states are shown in Figure 3-9a.

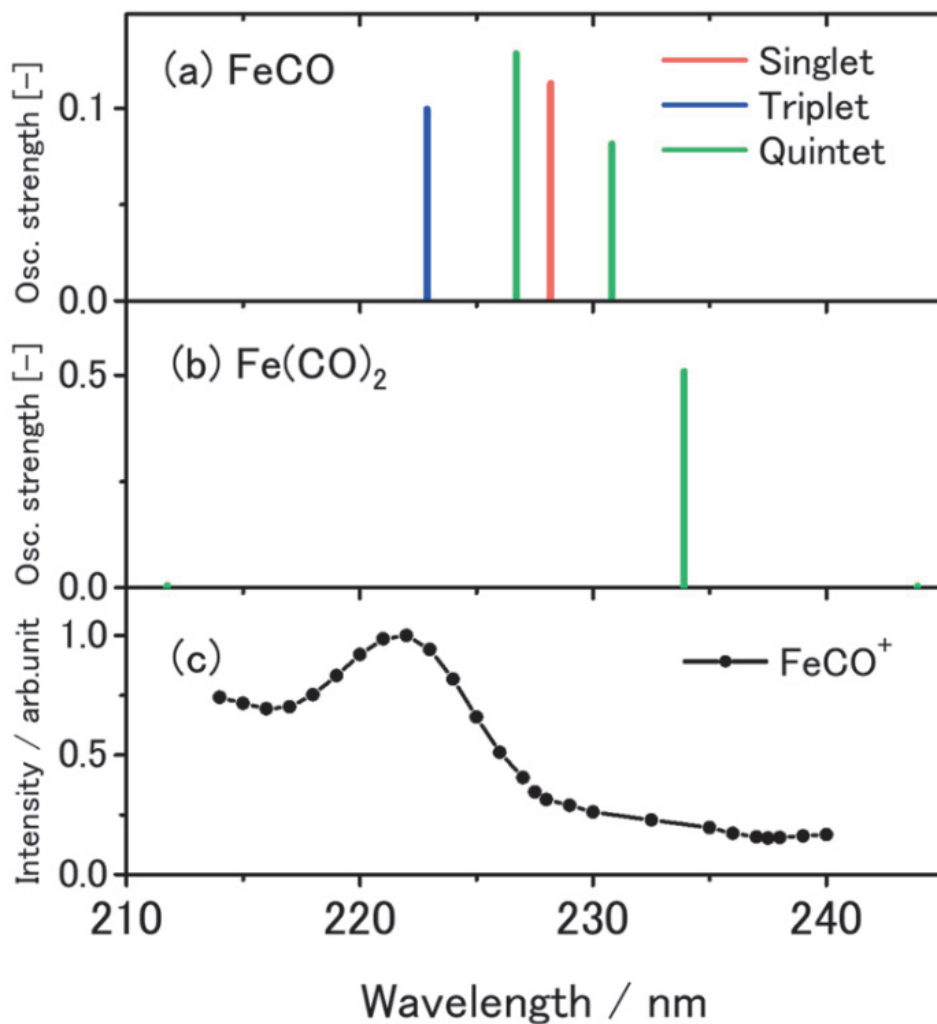


**Figure 3-9.** Theoretical oscillator strengths of (a) FeCO and (b) Fe(CO)<sub>2</sub> in each spin multiplicity: singlet (red), triplet (blue), and quintet (green). Electronic transitions from the lowest states in each spin multiplicity is shown at the energy difference to the upper states. (c) FeCO<sup>+</sup> yield spectrum.

Species	Vertical energy	Predominant transition							
FeCO (S)	228.19 nm		←		40%		←		40%
FeCO (T)	222.88 nm		←		20%		←		20%
			←		40%				
FeCO (Q)	230.81 nm		←		80%				
	226.70 nm		←		90%				
	226.70 nm		←		90%				
Fe(CO) <sub>2</sub> (Q)	237.31 nm		←		60 %				

**Figure 3-10** Molecular orbitals of FeCO and Fe(CO)<sub>2</sub> relevant to ultraviolet photoabsorption. Fraction (%) of the dominant molecular orbitals and the vertical energy (in nm) are shown for the electronic transitions from the lowest electronic state with each spin multiplicity (S: singlet, T: triplet, Q: quintet).

The photoabsorption bands of FeCO were theoretically predicted to appear in the 220–230 nm region with the comparably large oscillator strengths to the MLCT transitions of Fe(CO)<sub>5</sub>. The calculated oscillator strength of Fe(CO)<sub>2</sub> and the experimental result of the FeCO<sup>+</sup> yield spectrum are shown for comparison in Figures 3-9b and 3-9c, respectively. The CO loss in the quartet photoexcited state was implied by the anti-bonding molecular orbital ( $\pi_{\text{Fe-C}}^*$ ) with a node on the coordination bond (Figure 3-10). Although photodissociation in the triplet and singlet states was not confirmed in terms of the nodal pattern of the calculated orbitals, the photoexcitation of the high-lying singlet state is expected to result in CO loss based on the energetics. The molecular orbitals have another node on the C–O bond ( $\pi_{\text{C-O}}^*$ ), which can cause the vibrational excitation of the CO fragment. These results of the photoexcited states were in qualitative agreement with the theoretical study of FeCO by Ulusoy and Wilson using the time-dependent configuration interaction (TDCI) methodology coupled with the explicit spin-orbit interaction

Hamiltonian in the  $\tilde{X}^3\Sigma^-$  and  $\tilde{a}^5\Sigma^-$  states can exhibit distinct absorption bands in the ultraviolet region.<sup>57</sup> The lowest singlet state, which is energetically isolated from the low-lying  $\tilde{X}^3\Sigma^-$  and  $\tilde{a}^5\Sigma^-$  manifolds, was also predicted to have a photoabsorption band at a shorter wavelength ( $\approx 195$  nm) by the TDCI calculation. The corresponding band in our calculation appeared at  $\approx 225$  nm. We examined the photoabsorption of  $\text{Fe}(\text{CO})_2$  with the same calculation method; the photoabsorption of  $\text{Fe}(\text{CO})_2$  was found only for the low-lying quintet ( $\tilde{a}^5\Sigma_g^+$ ) state<sup>58</sup> in the 200–300 nm region. However, a plausible peak, which would be ascribed to the photoabsorption of  $\text{Fe}(\text{CO})_2$ , was not observed in the  $\text{Fe}(\text{CO})_2^+$  yield spectrum (Figure 3-8). The absence of a probable  $\text{Fe}(\text{CO})_2$  band in the experimental spectrum may suggest that  $\text{Fe}(\text{CO})_2$  is generated either in the  $\tilde{X}^3\Sigma_g^-$  state or a high-lying lowest singlet state, which is metastable, under the present photolysis conditions. Although the experimental result of  $\text{Fe}(\text{CO})_2$  was not fully explained, our DFT calculation supports that the vibrationally excited CO fragments can be generated following the FeCO photoabsorption at around 220 nm.

### 3-3-5. Scattering image of CO and Fe(CO)<sub>n=0-4</sub> photofragments

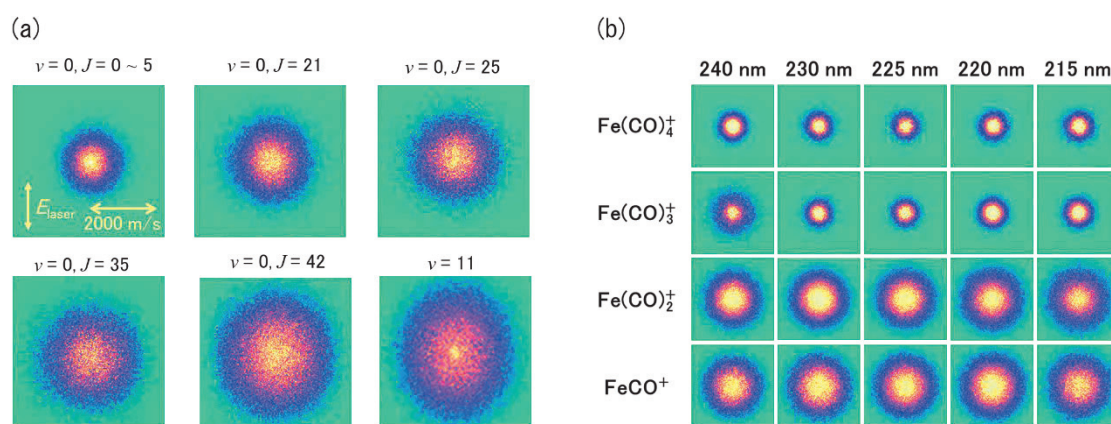


**Figure 3-11** (a) Rotationally state-resolved scattering images of the CO photofragments in the  $\nu = 0$  states. The image data of the CO fragment in the  $\nu = 11$  state is shown as an example of the scattering images of the highly vibrationally excited states. (b) Scattering images of Fe(CO)<sub>n=0-4</sub> fragments at different photolysis wavelengths.

The results of ion-imaging for the CO ( $\nu = 0$  and 11) products and other coordinatively unsaturated complexes are shown in Figure 3-11. The angular distributions of these fragments were isotropic ( $\beta \approx 0$ ). The CO photofragments in the low vibrational states are contributed from several photolytic processes of Fe(CO)<sub>n=1-5</sub>. The recoil velocity of the CO fragment increases with increasing internal energy. The Fe(CO)<sub>n=1-5</sub> fragment shows a tendency for the recoil velocity to increase with decreasing CO coordination number, i.e., with progressive dissociation.

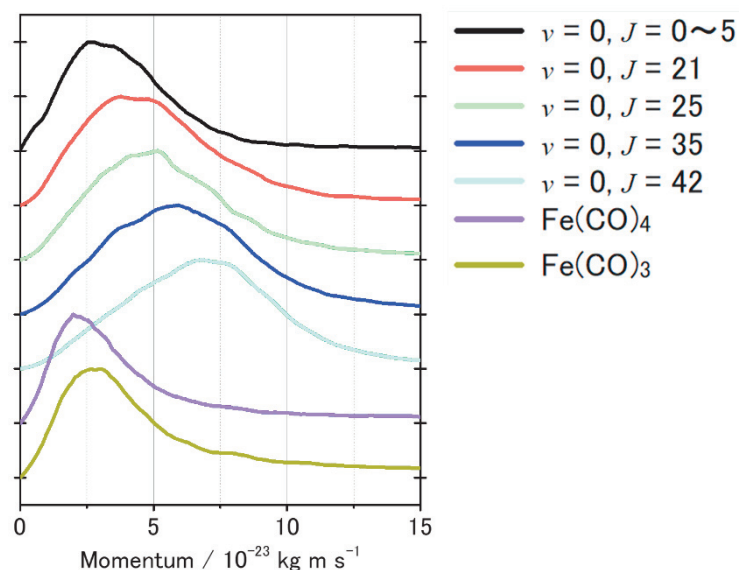


**Figure 3-12** Linear momentum distributions of the CO photofragments in the  $v = 0$  state obtained from the state-resolved scattering distributions.

The momentum distribution of CO fragments for vibrational state  $v=0$  and  $\text{Fe}(\text{CO})_{3,4}$  is shown in Figure 3-12. The released momentum distributions of the low- $J$  CO fragments showed relatively large overlap with those of  $\text{Fe}(\text{CO})_3$  and  $\text{Fe}(\text{CO})_4$ , both of which are widely accepted as the major products in the first photodissociation of  $\text{Fe}(\text{CO})_5$  in previous studies.<sup>6,7,29</sup> The results of the momentum matching imply that the first photodissociation of  $\text{Fe}(\text{CO})_5$  partly generates the CO product with low rotational excitation. Decrease of the degree of the momentum matching to  $\text{Fe}(\text{CO})_4$  and  $\text{Fe}(\text{CO})_3$  as the higher internal energy is regarded as a result of increasing contribution of the secondary photodissociation of the  $\text{Fe}(\text{CO})_{n<4}$  intermediates ( $\text{Fe}(\text{CO})_{n<4} + h\nu \rightarrow \text{Fe}(\text{CO})_{n-1} + \text{CO}$ ), which could be internally excited at the first photodissociation of  $\text{Fe}(\text{CO})_5$  in the same laser pulse. We decomposed the rotational state distributions (Figure 3-4) into two temperature components. Examination of both the final state distribution and the released momentum distribution suggests that the lower temperature component is possibly originated from the first photodissociation of the  $\text{Fe}(\text{CO})_5$  parent.

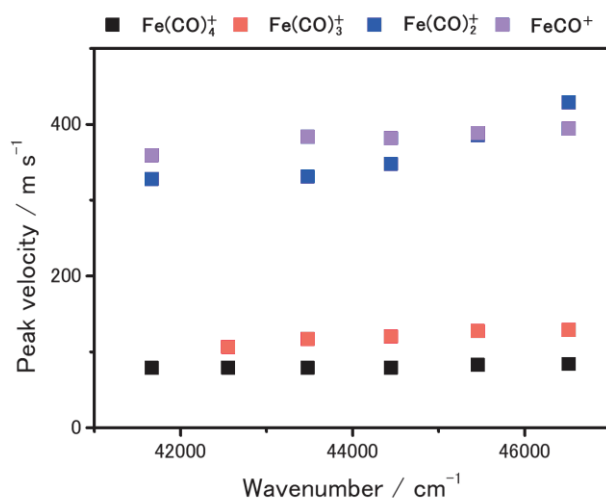


**Figure 3-13** Peak recoil velocity of the  $\text{Fe}(\text{CO})_{n=0-4}$  fragments obtained from the image data.

The peak recoil velocity of  $\text{Fe}(\text{CO})_{n=1-4}$  photofragments for each wavelength (Figure 3-11b) is shown in Figure 3-13. Relatively slow recoil velocities ( $\approx 100$  m/s) of  $\text{Fe}(\text{CO})_3$  and  $\text{Fe}(\text{CO})_4$ , both of which yield average of the translational energy releases of  $\approx 4$  kJ/mol, support a previous interpretation that CO loss at the first photodissociation of  $\text{Fe}(\text{CO})_5$ ,  $\text{Fe}(\text{CO})_5 + h\nu \rightarrow \text{Fe}(\text{CO})_4 + \text{CO}$  and  $\rightarrow \text{Fe}(\text{CO})_3 + 2\text{CO}$ , proceeds on the singlet potential energy surfaces.<sup>6,7,29</sup> Given the relative energies of the singlet states of  $\text{Fe}(\text{CO})_3$  (399 kJ/mol) and  $\text{Fe}(\text{CO})_4$  (175 kJ/mol) to the ground state of  $\text{Fe}(\text{CO})_5$  ( $\widehat{X}_{\text{Fe}}^1A'_1$ ), the effective available energy for  $\text{Fe}(\text{CO})_4 + \text{CO}$  and  $\text{Fe}(\text{CO})_3 + 2\text{CO}$  at the photolysis wavelength of 230 nm ( $h\nu = 520$  kJ/mol) is 345 kJ/mol and 121 kJ/mol, respectively (Figure 3-1). The peak  $v_{\text{recoil}}$  data in Figure 3-13 yielded fractions of the translational energy to the available energy ( $f_{\text{trans}}$ ) as 1.1 % for the  $\text{Fe}(\text{CO})_4 + \text{CO}$  pathway and as 4.6 % for the  $\text{Fe}(\text{CO})_3 + 2\text{CO}$  pathway. The approximate  $f_{\text{trans}}$  values are reasonable for the size of  $\text{Fe}(\text{CO})_5$ , supporting the generation of  $\text{Fe}(\text{CO})_4$  and  $\text{Fe}(\text{CO})_3$  in the singlet states.

### 3-4. Conclusion

We investigated the photoelimination of the CO ligands from  $\text{Fe}(\text{CO})_5$  in the gas phase. The  $\text{Fe}(\text{CO})_{n<5}$  intermediates generated by sequential CO loss of  $\text{Fe}(\text{CO})_5$  are subject to a second photodissociation under the laser photolysis condition. The resultant admixture of the CO fragments and the  $\text{Fe}(\text{CO})_{n<5}$  intermediates with different generation origins has not been experimentally resolved in the laser-based photodissociation studies, hindering the detailed examination of the photochemistry of the coordinatively unsaturated carbonyls. The photochemical phenomenon is a common characteristic of transition-metal carbonyls. We observed highly vibrationally excited CO ( $\nu = 11\text{--}15$ ) photofragments, whose generation was maximized at the photolysis wavelength of approximately 220 nm. The peak at 220 nm appeared also in the  $\text{FeCO}^+$  yield spectrum, whereas the spectra of other  $\text{Fe}(\text{CO})_{n=2-4}^+$  exhibited a monotonic increase with shorter wavelength, which was ascribed to the wavelength-dependence of the ionization efficiency above the ionization potentials. We considered that photochemistry at 220 nm gave rise to the correlated generation of the high- $\nu$  CO fragments and  $\text{FeCO}^+$ . The TD-DFT calculations corroborated the photoabsorption band of  $\text{FeCO}$  at around 220 nm. The energetics of the photoinitiated singlet excited states was well matched with the thresholds for high- $\nu$  CO loss and ionization, supporting our interpretation of  $\text{FeCO} + h\nu$  (220 nm)  $\rightarrow \text{Fe} + \text{CO}$  ( $\nu = 11\text{--}15$ ), and  $\rightarrow \text{FeCO}^+ + e^-$ . Our interpretation was further reinforced by the matched momentum distribution of the high- $\nu$  CO and Fe fragments. We note that the  $\text{Fe}(\text{CO})_n^+$  intensity in Figure 3-8 was so weak compared with bare  $\text{Fe}^+$  product that the signal had not been examined in the previous nanosecond photodissociation studies. In the present study, experimental evidence of the photodissociation of the coordinatively unsaturated carbonyl ( $\text{FeCO}$ ), which had not so

far been measured, was found in the measurement of the wavelength-dependence of the faint signals.

### Supporting information

	Spin state	$\Delta E$ kJ mol <sup>-1</sup>	Spin state	$\Delta E$ kJ mol <sup>-1</sup>	Spin state	$\Delta E$ kJ mol <sup>-1</sup>	APE kJ mol <sup>-1</sup>
Fe(CO) <sub>5</sub>	$^1A'_1$	0					762
Fe(CO) <sub>4</sub>	$^3B_2$	135	$^1A_1$	176	S2	366	855
Fe(CO) <sub>3</sub>	$^3A_2$	292	S1	401			934
Fe(CO) <sub>2</sub>	$^3\Sigma_g^-$	414	Q1	455	S1	670	1050
Fe(CO)	$^3\Sigma_g^-$	568	$^5\Sigma_g^-$	581	$^3\Sigma/{}^1\Delta$	752	1196
Fe	$^5D$	612	$^5F$	695	$^3F$	755	1408

**Table S1.** The experimental and theoretical data of Fe(CO)<sub>n</sub> and Fe(CO)<sub>n</sub><sup>+</sup> (n = 0, 1, 2, 3, 4 and 5)<sup>13, 16, 18, 54, 56 59, 60</sup>. APE is the appearance energy of Fe(CO)<sub>n</sub><sup>+</sup>.

### References

1. Zhou MF, Andrews L, Bauschlicher CW. Spectroscopic and theoretical investigations of vibrational frequencies in binary unsaturated transition-metal carbonyl cations, neutrals, and anions. *Chemical Reviews* 2001;101(7):1931-1961, doi:10.1021/cr990102b
2. Wrighton M. PHOTOCHEMISTRY OF METAL-CARBONYLS. *Chemical Reviews* 1974;74(4):401-430, doi:10.1021/cr60290a001
3. Leadbeater N. Enlightening Organometallic Chemistry: the Photochemistry of Fe(CO)<sub>5</sub> and the Reaction Chemistry of Unsaturated Iron Carbonyl Fragments. *Coordination Chemistry Reviews* 1999;188(35-70), doi:10.1016/s0010-8545(98)00217-3

4. Fuss W, Trushin SA, Schmid WE. Ultrafast photochemistry of metal carbonyls. *Research on Chemical Intermediates* 2001;27(4-5):447-457, doi:10.1163/156856701104202093
5. Trushin SA, Fuss W, Schmid WE, et al. Femtosecond Dynamics and Vibrational Coherence in Gas-phase Ultraviolet Photodecomposition of Cr(CO)<sub>6</sub>. *J Phys Chem A* 1998;102(23):4129-4137, doi:10.1021/jp973133o
6. Trushin SA, Fuss W, Kompa KL, et al. Femtosecond Dynamics of Fe(CO)<sub>5</sub> Photodissociation at 267 nm Studied by Transient Ionization. *J Phys Chem A* 2000;104(10):1997-2006, doi:10.1021/jp992474u
7. Cole-Filipiak NC, Tross J, Schrader P, et al. Ultraviolet photodissociation of gas-phase iron pentacarbonyl probed with ultrafast infrared spectroscopy. *J Chem Phys* 2021;154(13), doi:10.1063/5.0041074
8. Ershov KS, Kochubei SA, Baklanov AV. Tungsten Isotope-Specific UV-Photodecomposition of W(CO)<sub>6</sub> at 266 nm. *J Phys Chem A* 2019;123(36):7751-7757, doi:10.1021/acs.jpca.9b06793
9. Sun Y, Tang H, Chen K, et al. Two-State Reactivity in Low-Valent Iron-Mediated C-H Activation and the Implications for Other First-Row Transition Metals. *Journal of the American Chemical Society* 2016;138(11):3715-3730, doi:10.1021/jacs.5b12150
10. Weitz E. TRANSIENT INFRARED-SPECTROSCOPY AS A PROBE OF COORDINATIVELY UNSATURATED METAL-CARBONYLS IN THE GAS-PHASE. *Journal of Physical Chemistry* 1994;98(44):11256-11264, doi:10.1021/j100095a005
11. RYTHER RJ, WEITZ E. Reaction kinetics of coordinatively unsaturated iron carbonyls formed on gas-phase excimer laser photolysis of iron pentacarbonyl. *J Phys Chem* 1991;95(24):12, doi:10.1021/j100177a043
12. Gonzalez-Blanco O, Branchadell V. Density functional study of the Fe-CO bond dissociation energies of Fe(CO)<sub>5</sub>. *Journal of Chemical Physics* 1999;110(2):778-783, doi:10.1063/1.478045
13. Ryther RJ, Weitz E. DIODE-LASER PROBES OF THE PRODUCT DISTRIBUTION OF COORDINATIVELY UNSATURATED IRON CARBONYLS PRODUCED FOLLOWING EXCIMER LASER PHOTOLYSIS OF FE(CO)<sub>5</sub> IN THE GAS-PHASE. *Journal of Physical Chemistry* 1992;96(6):2561-2567, doi:10.1021/j100185a031
14. Behrens RG. THERMODYNAMICS OF TRANSITION-METAL CARBONYLS .2. MN(CO)<sub>5</sub>X, TC(CO)<sub>5</sub>X, RE(CO)<sub>5</sub>X (X=CL, BR, I). *Journal of the Less-Common Metals* 1978;61(2):321-339, doi:10.1016/0022-5088(78)90227-8
15. Housecroft CE, Wade K, Smith BC. REORGANIZATION ENERGIES AND SITE PREFERENCES OF CARBONYL LIGANDS - BOND-ENERGIES OF THE BRIDGING AND TERMINAL CARBONYL GROUPS OF THE IRON CARBONYLS FE<sub>2</sub>(CO)<sub>9</sub> AND FE(CO)<sub>5</sub>.

- Journal of Organometallic Chemistry 1979;170(1):C1-C5, doi:10.1016/s0022-328x(00)83196-4
16. K. Norwood, Ali A, Flesch GD, et al. A photoelectron-photoion coincidence study of iron pentacarbonyl. *Journal of the American Chemical Society* 1990;112(21):7
  17. Yardley JT, Gitlin B, Nathanson G, et al. Fragmentation and Molecular Dynamics in the Laser Photodissociation of Iron Pentacarbonyl. *J Chem Phys* 1981;74(1):370-378, doi:10.1063/1.440843
  18. Waller IM, Hepburn JW. State-Resolved Photofragmentation Dynamics of Fe(CO)<sub>5</sub> at 193, 248, 266, and 351 nm. *Journal of Chemical Physics* 1988;88(10):6658-6669, doi:10.1063/1.454406
  19. Ray U, Brandow SL, Bandukwalla G, et al. A CROSSED LASER-MOLECULAR BEAM STUDY OF THE PHOTODISSOCIATION DYNAMICS OF FE(CO)<sub>5</sub> AT 193 NM. *J Chem Phys* 1988;89(7):4092-4101, doi:10.1063/1.454845
  20. Venkataraman BK, Bandukwalla G, Zhang ZJ, et al. ONE-PHOTON AND 2-PHOTON PHOTODISSOCIATION OF FE(CO)<sub>5</sub> AT 248-NM - APPLICATION OF AN ACCURATE METHOD FOR CALCULATING ANGLE RESOLVED VELOCITY DISTRIBUTIONS FOR MULTIPLE SEQUENTIAL BOND RUPTURE PROCESSES. *J Chem Phys* 1989;90(10):5510-5526, doi:10.1063/1.456404
  21. Whetten RL, Fu KJ, Grant ER. PHOTO-DISSOCIATION DYNAMICS OF FE(CO)<sub>5</sub> - EXCITED-STATE LIFETIMES AND ENERGY DISPOSAL. *J Chem Phys* 1983;79(10):4899-4911, doi:10.1063/1.445582
  22. Willey KF, Brummel CL, Winograd N. Photoionization mechanisms for Cr(CO)<sub>6</sub> using high intensity laser pulses in the near-IR. *Chemical Physics Letters* 1997;267(3-4):359-364, doi:10.1016/s0009-2614(97)00089-4
  23. Gobeli DA, Yang JJ, El-Sayed MA. LASER MULTIPHOTON IONIZATION DISSOCIATION MASS-SPECTROMETRY. *Chemical Reviews* 1985;85(6):529-554, doi:10.1021/cr00070a002
  24. Engelking PC. ATOMIC IRON TRANSITIONS IN THE MULTI-PHOTON IONIZATION SPECTRA OF IRON CARBONYL AND FERROCENE NEAR 300 NM. *Chemical Physics Letters* 1980;74(2):207-210, doi:10.1016/0009-2614(80)85143-8
  25. Duncan MA, Dietz TG, Smalley RE. EFFICIENT MULTI-PHOTON IONIZATION OF METAL-CARBONYLS COOLED IN A PULSED SUPERSONIC BEAM. *Chemical Physics* 1979;44(3):415-419, doi:10.1016/0301-0104(79)85224-6
  26. Banares L, Baumert T, Bergt M, et al. The Ultrafast Photodissociation of Fe(CO)<sub>5</sub> in the Gas Phase. *J Chem Phys* 1998;108(14):5799-5811, doi:10.1063/1.475991
  27. Leutwyler S, Even U. LASER MULTI-PHOTON DISSOCIATION AND IONIZATION OF POLYNUCLEAR METAL-CARBONYLS IN SUPERSONIC BEAMS.

Chemical Physics Letters 1981;84(1):188-193, doi:10.1016/0009-2614(81)85398-5

28. Banares L, Baumert T, Bergt M, et al. Femtosecond photodissociation dynamics of Fe(CO)(5) in the gas phase. *Chemical Physics Letters* 1997;267(1-2):141-148, doi:10.1016/s0009-2614(97)00067-5
29. Wernet P, Leitner T, Josefsson I, et al. Direct Evidence for Sequential Dissociation of Gas-phase Fe(CO)<sub>5</sub> via a Singlet Pathway upon Excitation at 266 nm. *J Chem Phys* 2017;146(21):211103, doi:10.1063/1.4984774
30. Leitner T, Josefsson I, Mazza T, et al. Time-resolved electron spectroscopy for chemical analysis of photodissociation: Photoelectron spectra of Fe(CO)(5), Fe(CO)(4), and Fe(CO)(3). *J Chem Phys* 2018;149(4), doi:10.1063/1.5035149
31. Fournier R. THEORETICAL-STUDY OF THE MONOCARBONYLS OF 1ST-ROW TRANSITION-METAL ATOMS. *J Chem Phys* 1993;99(3):1801-1815, doi:10.1063/1.465297
32. Li J, Schreckenbach G, Ziegler T. A REASSESSMENT OF THE FIRST METAL-CARBONYL DISSOCIATION-ENERGY IN M(CO)(4) (M=NI, PD, PT), M(CO)(5) (M=FE, RU, OS), AND M(CO)(6) (M=CR, MO, W) BY A QUASI-RELATIVISTIC DENSITY-FUNCTIONAL METHOD. *Journal of the American Chemical Society* 1995;117(1):486-494, doi:10.1021/ja00106a056
33. Ziegler T. APPROXIMATE DENSITY FUNCTIONAL THEORY AS A PRACTICAL TOOL IN MOLECULAR ENERGETICS AND DYNAMICS. *Chemical Reviews* 1991;91(5):651-667, doi:10.1021/cr00005a001
34. Zalis S, Farrell IR, Vlcek A. The involvement of metal-to-CO charge transfer and ligand-field excited states in the spectroscopy and photochemistry of mixed-ligand metal carbonyls. A theoretical and spectroscopic study of W(CO)(4)(1,2-ethylenediamine) and W(CO)(4)(N,N'-bis-alkyl-1,4-diazabutadiene). *Journal of the American Chemical Society* 2003;125(15):4580-4592, doi:10.1021/ja021022j
35. Carreon-Macedo JL, Harvey JN. Computational study of the energetics of Fe-3(CO)(4), Fe-1(CO)(4) and Fe-1(CO)(4)(L), L = Xe, CH<sub>4</sub>, H<sub>2</sub> and CO. *Physical Chemistry Chemical Physics* 2006;8(1):93-100, doi:10.1039/b513325d
36. Harvey JN. DFT computation of relative spin-state energetics of transition metal compounds. In: *Principles and Applications of Density Functional Theory in Inorganic Chemistry I*. (Kaltsoyannis N, McGrady JE. eds.) 2004; pp. 151-183.
37. Yang L, Feng JK, Ren AM. Theoretical studies of ground and excited electronic states of complexes M(CO)(4)(phen) (M=Cr, Mo, W; phen=1,10-phenanthroline). *Synthetic Metals* 2005;152(1-3):265-268, doi:10.1016/j.synthmet.2005.07.091
38. Kim J, Kim TK, Lee YS, et al. Density functional and ab initio study of Cr(CO)(n) (n=1-6) complexes. *J Phys Chem A* 2007;111(21):4697-4710, doi:10.1021/jp066081o

39. Calaminici P, Janetzko F, Koster AM, et al. Density functional theory optimized basis sets for gradient corrected functionals: 3d transition metal systems. *J Chem Phys* 2007;126(4), doi:10.1063/1.2431643
40. Crespo-Otero R, Barbatti M. Cr(CO)(6) photochemistry: Semi-classical study of UV absorption spectral intensities and dynamics of photodissociation. *J Chem Phys* 2011;134(16), doi:10.1063/1.3582914
41. Narendrapurapu BS, Richardson NA, Copan AV, et al. Investigating the Effects of Basis Set on Metal-Metal and Metal-Ligand Bond Distances in Stable Transition Metal Carbonyls: Performance of Correlation Consistent Basis Sets with 35 Density Functionals. *Journal of Chemical Theory and Computation* 2013;9(7):2930-2938, doi:10.1021/ct4002398
42. Malcomson T, McKinlay RG, Paterson MJ. One- and Two-Photon-Induced Photochemistry of Iron Pentacarbonyl Fe(CO)(5) : Insights from Coupled Cluster Response Theory. *Chemphotochem* 2019;3(9):825-832, doi:10.1002/cptc.201900111
43. Kotzian M, Rosch N, Schroder H, et al. OPTICAL-SPECTRA OF TRANSITION-METAL CARBONYLS - CR(CO)6, FE(CO)5, AND NI(CO)4. *Journal of the American Chemical Society* 1989;111(20):7687-7696, doi:10.1021/ja00202a004
44. Sumida M, Masumoto S, Kato M, et al. Internal and Translational Energy Partitioning of the NO Product in the S2 Photodissociation of Methyl Nitrite. *Chemical Physics Letters* 2017;674(58-63), doi:10.1016/j.cplett.2017.02.044
45. Kohge Y, Hanada T, Sumida M, et al. Photodissociation dynamics of nitromethane at 213 nm studied by ion-imaging. *Chemical Physics Letters* 2013;556(49-54), doi:10.1016/j.cplett.2012.11.076
46. Birge RT. The band spectra of carbon monoxide. *Physical Review* 1926;28(6):1157-1181, doi:10.1103/PhysRev.28.1157
47. Krupenie PH. The Band Spectrum of Carbon Monoxide. US Govt. Printing Office, Washington: 1966.
48. Katayanagi H, Suzuki T. Non-adiabatic bending dissociation of OCS: the effect of bending excitation on the transition probability. *Chemical Physics Letters* 2002;360(1-2):104-110, doi:10.1016/s0009-2614(02)00788-1
49. M. J. Frisch GWT, H. B. Schlegel, G. E. Scuseria, M. A. Robb, J. R. Cheeseman, G. Scalmani, V. Barone, G. A. Petersson, H. Nakatsuji, X. Li, M. Caricato, A. V. Marenich, J. Bloino, B. G. Janesko, R. Gomperts, B. Mennucci, H. P. Hratchian, J. V. Ortiz, A. F. Izmaylov, J. L. Sonnenberg, D. Williams-Young, F. Ding, F. Lipparini, F. Egidi, J. Goings, B. Peng, A. Petrone, T. Henderson, D. Ranasinghe, V. G. Zakrzewski, J. Gao, N. Rega, G. Zheng, W. Liang, M. Hada, M. Ehara, K. Toyota, R. Fukuda, J. Hasegawa, M. Ishida, T. Nakajima, Y. Honda, O. Kitao, H. Nakai, T. Vreven, K. Throssell, J. A. Montgomery, Jr., J. E. Peralta, F. Ogliaro, M. J. Bearpark, J.

- J. Heyd, E. N. Brothers, K. N. Kudin, V. N. Staroverov, T. A. Keith, R. Kobayashi, J. Normand, K. Raghavachari, A. P. Rendell, J. C. Burant, S. S. Iyengar, J. Tomasi, M. Cossi, J. M. Millam, M. Klene, C. Adamo, R. Cammi, J. W. Ochterski, R. L. Martin, K. Morokuma, O. Farkas, J. B. Foresman, and D. J. Fox, Gaussian, Inc., Wallingford CT, 2016. Gaussian 16, Revision C.01.
50. Kasai Y, Obi K, Ohshima Y, et al. PURE ROTATIONAL SPECTRUM OF FE<sub>2</sub>CO. *Journal of Chemical Physics* 1995;103(1):90-95, doi:10.1063/1.469626
  51. Tanaka K, Shirasaka M, Tanaka T. Millimeter-wave spectroscopy of the iron carbonyl radical (FeCO). *J Chem Phys* 1997;106(17):6820-6824, doi:10.1063/1.473709
  52. Tanaka K, Tachikawa Y, Sakaguchi K, et al. Time-resolved infrared diode laser spectroscopy of the  $\nu(3)$  band of the jet-cooled Fe(CO)(2) radical produced by ultraviolet photolysis of Fe(CO)(5). *J Chem Phys* 1999;111(9):3970-3977, doi:10.1063/1.479699
  53. Matveev A, Staufer M, Mayer M, et al. Density functional study of small molecules and transition-metal carbonyls using revised PBE functionals. *Int J Quantum Chem* 1999;75(4-5):863-873, doi:10.1002/(sici)1097-461x(1999)75:4/5<863::aid-qua51>3.0.co;2-t
  54. Tanaka K, Sakaguchi K, Tanaka T. Time-resolved infrared diode laser spectroscopy of the  $\nu(1)$  band of the iron carbonyl radical (FeCO) produced by the ultraviolet photolysis of Fe(CO)(5). *J Chem Phys* 1997;106(6):2118-2128, doi:10.1063/1.473143
  55. Villalta PW, Leopold DG. A STUDY OF FE<sub>2</sub>CO- AND THE (3)SIGMA(-) AND (5)SIGMA(-) STATES OF FE<sub>2</sub>CO BY NEGATIVE-ION PHOTOELECTRON-SPECTROSCOPY. *J Chem Phys* 1993;98(10):7730-7742, doi:10.1063/1.464580
  56. Hirano T, Okuda R, Nagashima U, et al. Geometries and electronic structures of the ground and low-lying excited states of FeCO: An ab initio study. *JOURNAL OF CHEMICAL PHYSICS* 2012;137(24), doi: 10.1063/1.4769283
  57. Ulusoy IS, Wilson AK. Spin trapping and flipping in FeCO through relativistic electron dynamics. *Physical Chemistry Chemical Physics* 2019;21(14):7265-7271, doi:10.1039/c8cp06583g
  58. Barnes LA, Rosi M, Bauschlicher CW. AN ABINITIO STUDY OF FE(CO)<sub>1</sub>, FE(CO)<sub>5</sub>, AND CR(CO)<sub>6</sub>. *J Chem Phys* 1991;94(3):2031-2039, doi:10.1063/1.459924
  59. M. Fieber-Erdmann, E. Holub-Krappe, G. Broker, G. Dujardin, A. Ding, Fragmentation spectroscopy of photoionized Fe(CO)<sub>5</sub>: a molecular model for a heterogeneous cluster, *Int. J. Mass Spectrom. Ion Processes* 1995; 149/150:513-520
  60. Karan E. Lewis, David M. Golden, and Gregory P. Smith, Organometallic bond dissociation energies: laser pyrolysis of iron pentacarbonyl, chromium hexacarbonyl, molybdenum hexacarbonyl, and tungsten hexacarbonyl, *Journal of the American Chemical Society* 1984;106(14):3905-3912

## Chapter 4

# Primary and Secondary Processes in the Ultraviolet Photodissociation of $\text{CpCo}(\text{CO})_2$

## 4-1. Introduction

Transition-metal complexes typically possess dense electronic state structures originating from the *d*-orbitals of their metal centers.<sup>1-4</sup> The electronically excited states exhibiting significant absorption cross sections from the ground state are mostly located in the visible and ultraviolet regions, where photochemistry is initiated by ultrafast internal conversion between the energetically close electronic states.<sup>5-8</sup> Internal conversion, whose rate is strongly correlated with the state density, can compete with ligand loss on specific potential energy surfaces. The electronic ground state and low-lying excited states can be responsible for the metal–ligand dissociation if the potential energy surface is repulsive. Transition-metal carbonyls, whose photochemistry has been extensively studied as typical transition-metal complexes, undergo ultrafast internal conversion upon metal-to-ligand charge transfer (MLCT) photoexcitation in the ultraviolet region followed by CO loss.<sup>8-17</sup> Despite the efficient use of transition-metal carbonyl photolysis for CO production, the specific electronic states driving CO production remain incompletely determined. Notably, identifying the potential energy surface on which CO loss proceeds will enable the identification of the generated states in coordinatively unsaturated complexes, which play essential roles in the photochemistry of transition-metal complexes due to the high reactivity.<sup>10,13</sup> In this regard, the mechanism of photo-induced CO loss of transition-metal carbonyls has yet to be elucidated in detail, for which laser-based reaction dynamics approaches should be potentially powerful.

The intrinsic properties of transition-metal carbonyl photochemistry, involving the competition between sequential dissociation and second photodissociation, pose significant challenges in resolving the electronic states of the photoproducts and unsaturated complexes. In particular, the second photodissociation occurs when

unsaturated complexes produced from the first photodissociation undergo dissociation within an identical laser pulse, and this phenomenon becomes unavoidable in nanosecond laser experiments for transition-metal complexes.<sup>18</sup> Previous studies have employed a ladder switching model to examine successive photodissociation of transition-metal complexes terminating in the atomic metal generation.<sup>18-21</sup> The nanosecond pulse duration provides ample time for the unsaturated carbonyls to absorb an additional photon, facilitated by their large absorption cross section, which is comparably large to that of the saturated transition-metal carbonyls due to metallic *d*-orbitals. Standard laser ionization detection pulse energies provide sufficient photoabsorption rates for transition-metal carbonyls and intermediates, generating a mixture of complexes with varying coordination numbers. Due to overlapping final state distributions and kinetic energy release distributions of CO fragments and coordinatively unsaturated complexes with different origins, a conventional analysis cannot be applied to laser-based reaction dynamics studies. Competition between the first photodissociation, sequential dissociation, and second photodissociation of intermediates remains unavoidable in pulsed laser photodissociation experiments. These experiments, however, offer a state-resolved understanding of CO loss. Separate measurement of concurrent processes in a single laser pulse requires alternative methods to conventional ones. In our previous study on Fe(CO)<sub>5</sub> photodissociation, we observed distinct variations in the ion-images of unsaturated intermediates with respect to photolysis wavelengths, providing key insights into the involved.<sup>22</sup>

Most heteroleptic carbonyl complexes exhibit MLCT bands that are relevant to charge transfer to individual ligands in the ultraviolet region. Tuning the photolysis wavelengths can enable the selection of excited states that involve specific charge-

transferred ligands, provided that different charge distributions sufficiently modify the electronic energies. For example, in the cobalt carbonyl analog  $\text{CoNO}(\text{CO})_3$ , the charge transfer to the CO ligands induces a strong absorption band in the deep ultraviolet region, whereas the charge transfer to the NO ligand induces a relatively weak band in the near-ultraviolet region.<sup>23,24</sup> Exploring photolysis wavelength dependence is expected to provide insights into controlling the photochemical outcome of heteroleptic carbonyls. However, such an approach, based on a direct relationship between the photolysis wavelengths and charge distribution on CO ligands, is not directly applied in homoleptic carbonyls. Furthermore, metal complexes with too many CO ligands would exhibit several sequential CO loss pathways, preventing the conduct of selective measurements. We previously analyzed the ion-imaging data combined with photolysis wavelength dependence during the photodissociation study of  $\text{Fe}(\text{CO})_5$  as a typical homoleptic carbonyl complex.<sup>22</sup> Here, we extended to apply the similar experimental and analysis approaches to the photodissociation of  $\text{CpCo}(\text{CO})_2$ , in which the releasing CO ligands are limited to two. Another ligand of Cp (cyclopentadienyl,  $\text{C}_5\text{H}_5$ ) is coordinated to the Co center with the  $\eta^5$  form, which is less dissociative than the CO ligands. We regard the  $\text{CpCo}(\text{CO})_2$  complex as a simple system for investigating the photodissociation dynamics of heteroleptic transition-metal carbonyls.

#### 4-2. Experimental and Calculation methods

Velocity mapping ion-imaging of the  $\text{CpCo}(\text{CO})_2$  photodissociation fragments was performed for the CO ligands and coordinatively unsaturated complexes. The details of the experimental setup were described elsewhere.<sup>25</sup> We used commercial  $\text{CpCo}(\text{CO})_2$  liquid (>90%, Sigma-Aldrich), whose vapor pressure at room temperature was approximately 1 Torr, to prepare a gaseous sample of 0.01% concentration diluted with a

He buffer without further purification. The molecular beam of  $\text{CpCo}(\text{CO})_2$  was generated using a piezoelectric pulsed valve with a stagnation pressure of 2 bar. The  $\text{CpCo}(\text{CO})_2$  molecular beam collimated by a skimmer on the wall dividing the source chamber and the detector chamber was introduced in the velocity-mapping electrodes, where a photolysis laser pulse intersected with the molecular beam. We confirmed that cluster formation in the molecular beam was negligible under these conditions by measuring the stagnation pressure dependence on the CO fragment spectra. The pressures of the source and detector chambers were  $3 \times 10^{-6}$  Torr and  $1 \times 10^{-7}$  Torr, respectively, when the pulsed valve was operated at a repetition rate of 10 Hz.

The laser pulse was an output of a frequency-doubled dye laser (CobraStretch, Sirah) pumped by the third harmonics of a YAG laser system (LAB 170, Spectra Physics). We examined the wavelength region of 210 – 240 nm, where the MLCT bands of  $\text{CpCo}(\text{CO})_2$  are located. The laser pulse served as the pump (photolysis) and probe (ionization) pulses in the present measurements of  $\text{CpCo}(\text{CO})_2$  photodissociation and product ionization successively occurred in a single laser pulse, with an approximately 10 ns duration. We detected CO photofragments and coordinatively unsaturated complexes,  $\text{CpCoCO}$ ,  $\text{CpCo}$ ,  $\text{CoC}_3\text{H}_3$ , and  $\text{CoC}_2\text{H}_n$ , as their ion signals. The CO fragments were state-selectively ionized with the  $[2 + 1]$  resonantly-enhanced multiphoton ionization (REMPI) scheme via the  $\tilde{\text{B}}_{\text{g}}^1\Sigma^+ - \tilde{\text{X}}_{\text{g}}^1\Sigma^+$  transition located in the examined wavelength region. The pulse energy was kept at 60  $\mu\text{J}/\text{pulse}$  to suppress the multiphoton processes of the  $\text{CpCo}(\text{CO})_2$  parent. CO predissociation in the  $\tilde{\text{B}}_{\text{g}}^1\Sigma^+$  state limited us to measure the ro-vibrationally state-resolved REMPI spectra only for the  $\nu = 0$  and  $\nu = 1$  vibrational states. The state-resolved ion-imaging of the CO photofragment was performed based on the REMPI spectra. The velocity distributions were obtained

with the inverse Abel transform applying to the observed image data. The velocity scale of the observed images was calibrated with the recoil velocity of the CO photofragment in the OCS photodissociation measured under the same detection conditions and the literature value of the CO + S bond dissociation energy.<sup>26</sup>

The scattering images of the coordinatively unsaturated products were measured using a non-resonant ionization scheme. Notably, pulse energy of 60  $\mu\text{J/p}$  corresponds to a photon flux of  $7.6 \times 10^7 \text{ W/cm}^2$  in our focusing condition (0.1 mm in diameter), by which two-photon absorption of the  $\text{CpCo(CO)}_2$  parent and unsaturated products are unlikely based on the comparison with the well-known  $\text{Fe(CO)}_5$  complex.<sup>18,27</sup> However, the unsaturated products that absorbed the second photon within the same laser pulse underwent secondary photodissociation and photoionization, yielding the  $\text{CpCoCO}^+$ ,  $\text{CpCo}^+$ ,  $\text{CoC}_3\text{H}_3^+$ , and  $\text{CoC}_2\text{H}_n^+$  ion signals. We measured the time-of-flight (TOF) mass spectra of these unsaturated complex ions as a function of the photolysis wavelength at 2.5 or 5 nm intervals in the 210 – 240 nm region. We used the energetics data of the unsaturated complexes, such as the bond dissociation energy and ionization potential in previous studies<sup>28-30</sup> for analyzing the wavelength dependence of the product ion yield spectra and translational energy releases.

We measured the ion-images of CO,  $\text{CpCoCO}$ ,  $\text{CpCo}$ ,  $\text{CoC}_3\text{H}_3$ , and  $\text{CoC}_2\text{H}_n$ . Three generation origins were involved in the measurements of the individual products: the first and secondary dissociations and sequential dissociation (see Figure 4-1). The first photodissociation specifically refers to the CO loss of the parent  $\text{CpCo(CO)}_2$  photodissociation:  $\text{CpCo(CO)}_2 + h\nu \rightarrow \text{CpCoCO} + \text{CO}$ . The signal due to Cp loss in the  $\text{CpCo(CO)}_2$  photodissociation generating  $\text{Co(CO)}_2$  was undetected. Part of the  $\text{CpCoCO}$  intermediate with sufficient internal energy underwent sequential dissociation to  $\text{CpCo} +$



where  $\mathbf{v}_1 = \mathbf{u}_2 + \mathbf{v}_2$ . We followed the formulation developed by Venkataraman et al. for the Fe(CO)<sub>5</sub> photodissociation study.<sup>32</sup> We assumed isotropic angular distributions (no  $\theta$ -dependence) in  $P_1^{LAB}(\mathbf{v}_1)$  and  $P_2^{CM}(\mathbf{u}_2)$  since significant anisotropy was unobserved in the imaging results. Thus, the formula employed in the present image data analysis was simplified as follows:

$$P_2^{LAB}(\mathbf{v}_2) = 2\pi \int_0^\infty P_1^{LAB}(\mathbf{v}_1) v_1^2 \int_0^\pi P_2^{CM}(\mathbf{u}_2) \sin \theta \, d\theta \, dv_1. \quad (2)$$

We applied a fitting procedure to the observed image data of CpCoCO and CpCo as  $P_1^{LAB}(v_1)$  and  $P_2^{LAB}(v_2)$ , respectively, to obtain the center-of-mass velocity distribution of CpCo as  $P_2^{CM}(u_2)$ , which was expanded by a set of fitting parameters ( $c_i$ ) with equally separated ( $\Delta v = 1 \text{ ms}^{-1}$ ) rectangular velocity basis functions ( $f_i$ ) as

$$P_2^{CM}(u_2) = \sum_i c_i f_i(v_i^{center}). \quad (3)$$

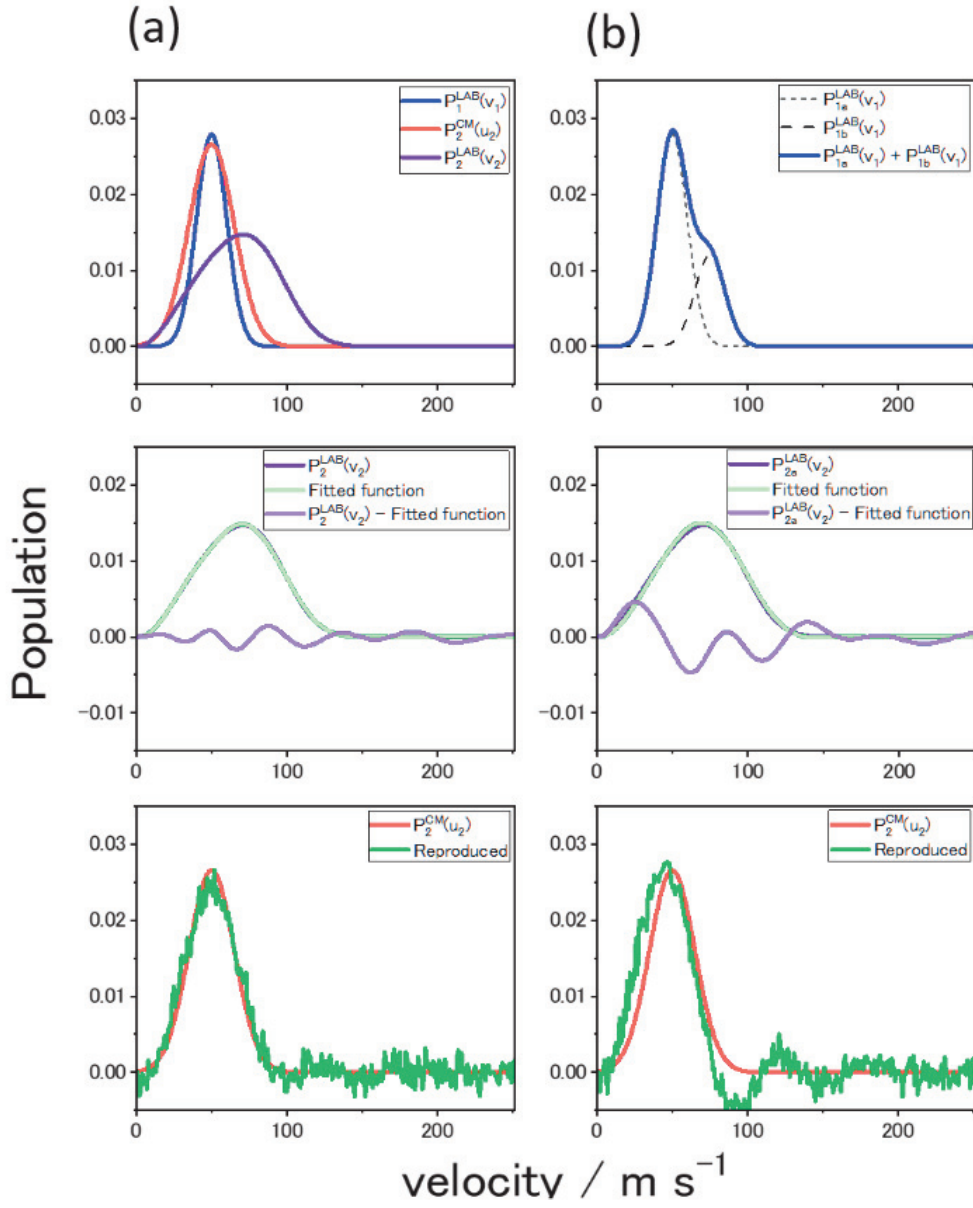


Figure 4-2. Forward convolution of model functions for the center-of-mass velocity distributions ( $P_2^{CM}(\mathbf{u}_2)$ , —) and the laboratory frame velocity distributions ( $P_1^{LAB}(\mathbf{v}_1)$ , —). The  $P_1^{LAB}(\mathbf{v}_1)$  functions correspond to the velocity distribution of the precursor, whose dissociation is assumed to release the final fragments with the  $P_2^{CM}(\mathbf{u}_2)$  function. We employed a single Gaussian function as  $P_1^{LAB}(\mathbf{v}_1)$  for this examination. The convolution (—) of  $P_1^{LAB}(\mathbf{v}_1)$  and  $P_2^{CM}(\mathbf{u}_2)$  yields a measurable distribution ( $P_2^{LAB}(\mathbf{v}_2)$ ).

Extraction of the  $P_2^{CM}(u_2)$  function from the convoluted function of  $P_2^{LAB}(v_2)$  and  $P_2^{CM}(u_2)$  was inspected for some model functions before applying the analysis to the experimental data (Figure 4-2). Forward convolution of model functions for the center-of-mass velocity distributions ( $P_2^{CM}(u_2)$ , —) and the laboratory frame velocity distributions ( $P_1^{LAB}(v_1)$ , —). The  $P_1^{LAB}(v_1)$  functions correspond to the velocity distribution of the precursor, whose dissociation is assumed to release the final fragments with the  $P_2^{CM}(u_2)$  function. We employed a single Gaussian function as  $P_1^{LAB}(v_1)$  for this examination. The convolution (—) of  $P_1^{LAB}(v_1)$  and  $P_2^{CM}(u_2)$  yields a measurable distribution ( $P_2^{LAB}(v_2)$ ). Angular distributions are assumed to be isotropic in the analysis. The dots (●) denote the coefficients of the basis functions determined by the fitting procedure, in which equally spaced narrow velocity distributions were used for reproducing the convoluted function (—). The reproduction results assuming (a) a single Gaussian that is identical to the input function and (b) two partially overlapped Gaussian functions as  $P_1^{LAB}(v_1)$  were compared in the bottom plots. The target  $P_2^{CM}(u_2)$  function was well reproduced by the fitted result (—) to the convoluted  $P_2^{LAB}(v_2)$  function ((a), bottom). Although the fitted coefficients look similar to the result of (a), the obtained  $P_2^{CM}(u_2)$  function in the (b) assumption yielded unphysical results with negative populations. The oscillatory behaviors around zero intensity in the higher velocity regions, which is a numerical artifact, can be an indication of several components in the velocity distribution of the precursor.

Quantum chemistry calculations for  $\text{CpCo}(\text{CO})_2$  and  $\text{CpCoCO}$  were performed using the Gaussian16 program package.<sup>33</sup> We used the 6-31+G(d) and 6-311++G(d, p) basis functions for Co and ligands, respectively. The results of the DFT calculations with the B3LYP, BVP86, and CAM-B3LYP functionals were compared to examine the

calculation accuracy, yielding qualitatively consistent data. Our calculations satisfactorily reproduced the structural parameters for the ground state  $\text{CpCo}(\text{CO})_2$  in the literature.<sup>30,34</sup> The optical oscillator strengths between the electronic ground and excited states for  $\text{CpCo}(\text{CO})_2$  were calculated with the TD-DFT level of theory at the optimized structure in the ground state. We found 27 singlet electronic states in the energy range of 7 eV above the ground state. The characters of the photoabsorption bands were examined based on the molecular orbitals associated with the electronic transitions. The excited state energy was calculated using the TD-CAM-B3LYP method. The potential energy curves of these singlet states were calculated with varying Co–CO bond lengths from 1.2 Å to 4.0 Å, with an increment of 0.1 Å while other structural parameters were optimized. We also executed the same calculations for  $\text{CpCoCO}$ , which is the product of CO loss of the  $\text{CpCo}(\text{CO})_2$  first photodissociation and the precursor of the second photodissociation producing  $\text{CpCo} + \text{CO}$ .

### 4-3. Results

#### 4-3-1. UV/Vis absorption spectrum of $\text{CpCo}(\text{CO})_2$

Figure 4-3 shows the experimental and theoretical photoabsorption spectra of the  $\text{CpCo}(\text{CO})_2$  vapor and molecular orbital associated with the photoabsorption bands. The ultraviolet absorption spectrum (Figure 4-3(a), red curve) was measured by a UV lamp spectrometer (Hitachi, U3000), in which a quartz cell was filled with the  $\text{CpCo}(\text{CO})_2$  vapor of 1 Torr. Four band features peaking at 200, 230, 250, and 290 nm were distinct in the 190 – 350 nm wavelength region. The simulated absorption spectrum (Figure 4-3(a), black curve) was synthesized with the oscillator strengths (Figure 4-3(a), stick) obtained from the DFT calculations and appropriate Gaussian envelopes. The overall features of

the four bands of the experimental spectrum were well reproduced by the calculation. The present calculations revealed that these four bands were contributed by several electronic transitions (shown by sticks in Figure 4-3(a)) which have the same electronic character. Figure 4-3(b) shows the molecular orbitals associated with the individual peaks. The nodal patterns and charge transfer of the molecular orbitals provide a qualitative characterization of the band peaks. The band peaked at 300 nm was characterized by the electron promotion to the anti-bonding orbitals concerning the Co–CO bond. The charge transfer from Co to the ligands was smaller than those of other bands. This band is responsible for the photodissociation study at 355 nm by Oana et al., in which the internal excitation of CpCoCO and CO was observed.<sup>35</sup> The Co–CO dissociativeness at the 300 nm band indicated by the present molecular orbital calculations corroborated previous experimental studies.<sup>35</sup> The two bands in the 210 – 240 nm region, for which the present measurements were conducted, were found to comprise several electronic transitions

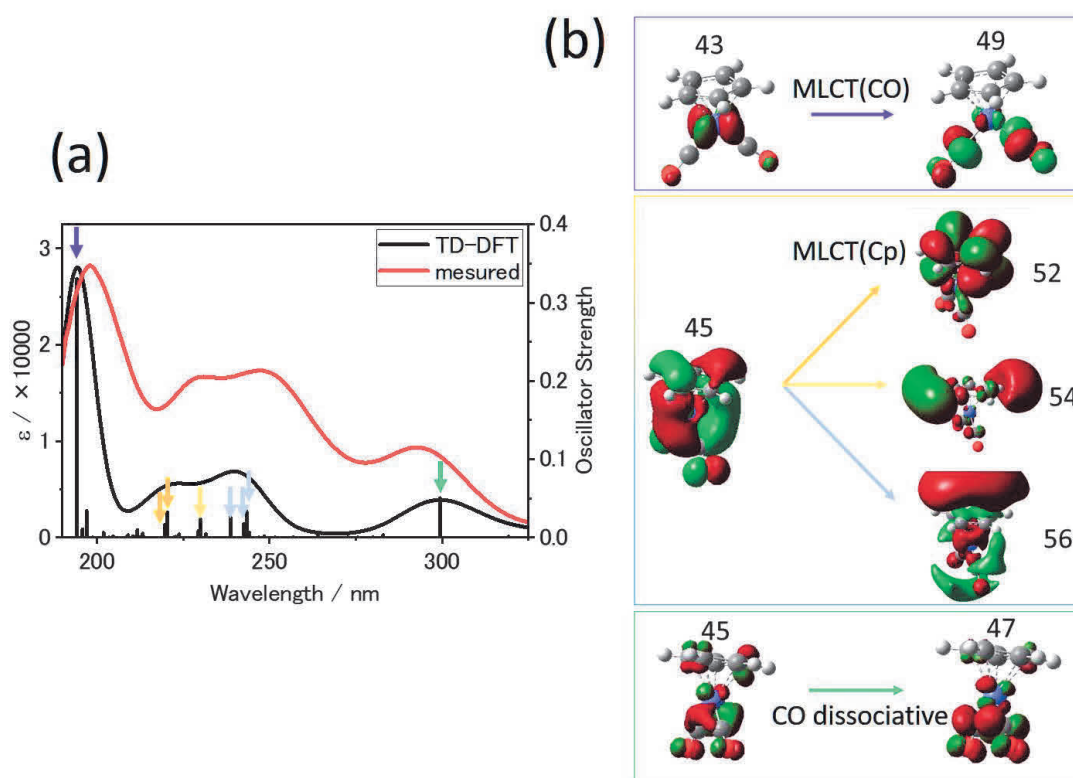


Figure 4-3 (a) Experimental and theoretical photoabsorption spectra of gaseous  $\text{CpCo}(\text{CO})_2$  in the ultraviolet region. The theoretical spectrum (black curve) was calculated using the oscillator strengths (stick) with Gaussian profile envelopes. (b) Molecular orbitals associated with the photoabsorption bands. The typical molecular orbitals of the four peaks in the spectra are shown with the corresponding colors of the arrows. The numbers designated on the molecular orbitals indicate the order of the energy.

characterized as charge transfers from the Co metal to the Cp ligand (MLCT(Cp)). The large electron density variation either in the in-plane or out-of-plane orbitals of Cp with close energies indicated Cp framework deformation upon photoexcitation. The strong 200 nm band was ascribed to a single electronic transition with an MLCT character to the CO ligand (MLCT(CO)). In contrast to the 210 – 240 nm bands, a structural change in the Cp ligand was unexpected in the 200 nm photochemistry.

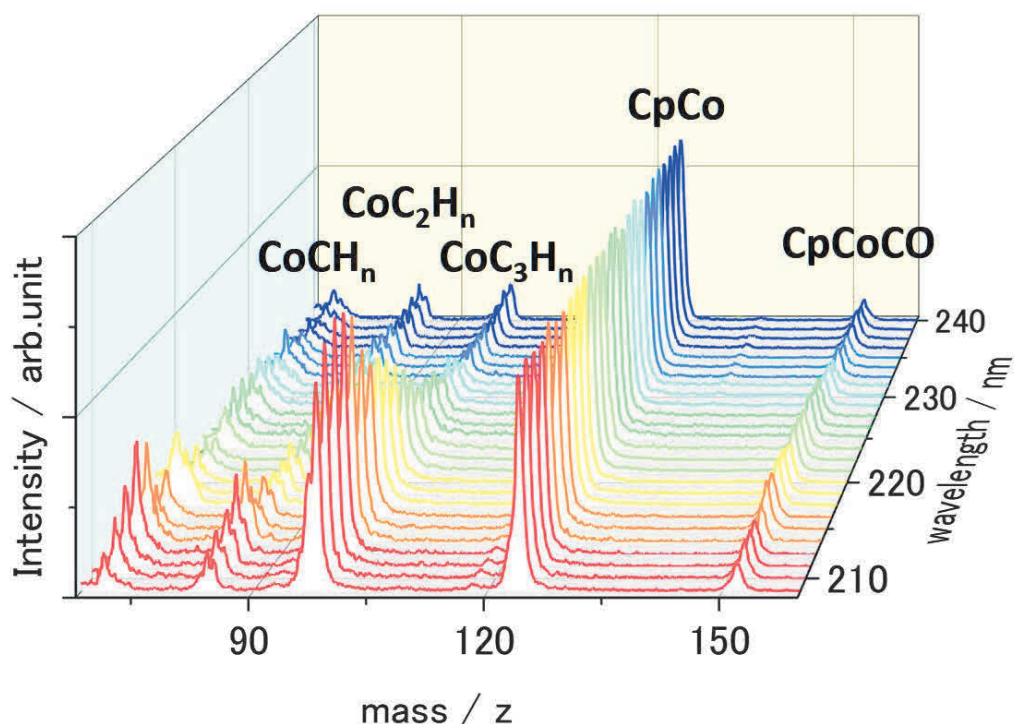


Figure 4-4 Product ion yield spectra in the  $\text{CpCo}(\text{CO})_2$  photolysis as a function of photolysis wavelength in the MLCT(Cp) band

#### 4-3-2. Photolysis yield spectra in $\text{CpCo}(\text{CO})_2$ photofragments

Figure 4-4 shows the fragment yield spectra in the 210 – 240 nm region, in which the mass spectra measured at varied photolysis wavelengths were normalized at the  $\text{CpCo}^+$  intensity. These fragment ions were first produced as neutral fragments in the  $\text{CpCo}(\text{CO})_2$  photodissociation; then, they were non-resonantly ionized in the same laser pulse. The most prominent peak in the MLCT(Cp) bands was the  $\text{CpCo}^+$  signal, which resulted from two CO ligand losses. The signal intensity of the single CO loss product ( $\text{CpCoCO}$ ) was as small as less than 10% of the two CO losses, suggesting the sequential dissociation and secondary photodissociation of  $\text{CpCoCO}$ . While the signal indicating Cp loss such as  $\text{Co}(\text{CO})_{1,2}^+$  was unobserved, the coordinatively unsaturated complexes with a partially decomposed Cp ligand ( $\text{CoC}_3\text{H}_n^+$ ,  $\text{CoC}_2\text{H}_n^+$ , and  $\text{CoCH}_n^+$ ) were detected with

comparable intensity to  $\text{CpCo}^+$ . The absence of Cp loss signal was consistent with the photodissociation result of  $\text{CpCo}(\text{CO})_2$  in the previous study;<sup>35</sup> however, Cp loss can undergo depending on relative reactivity to other ligands in the excited states.<sup>36</sup> Notably, the observed wavelength dependence of the fragment ion yields (Figure 4-4) can be ascribed to both the neutral fragmentations in potential pathways (Figure 4-1) and the ionization efficiency of the individual fragments. These processes occur via one-photon absorption in a single laser pulse. The ionization efficiency curve would increase moderately with the photon energy above the ionization threshold. The relative intensity of  $\text{CpCoCO}^+$  to that of  $\text{CpCo}^+$  was almost flat in the entire wavelength region, whereas the fragments with a partially decomposed Cp ligand exhibited peculiar variations with the wavelength. The observed fragment ions could not be attributed to the dissociative ionization resulting from the two-photon absorption, as the intensity of  $\text{CpCo}(\text{CO})_2^+$  is negligible, accounting for less than 1 % of other fragment ions. Here, we assumed that the fragment ion signal would be larger than the parent (precursor) ion if the dissociative ionization dominates the photochemistry. With regard to the energetics, the  $\text{CpCoCO}^+$  intensity appeared at 240 nm, whose two-photon energy of 10.3 eV was lower than the dissociative ionization threshold, and the relative intensities of  $\text{CpCo}^+$  and  $\text{CpCoCO}^+$  were much different from the dissociative ionization results.<sup>30</sup> Furthermore, although the two-photon absorption cross section data of  $\text{CpCo}(\text{CO})_2$  is not available, the previous theoretical and experimental studies<sup>2,22</sup> of an analogous transition-metal carbonyl ( $\text{Fe}(\text{CO})_5$ ) indicated that two-photon excitation followed by dissociative ionization was unlikely under the present laser conditions.

4-3-3. Photolysis wavelength dependence of recoil velocity in CpCoCO, CpCo, CoC<sub>3</sub>H<sub>3</sub> photofragments

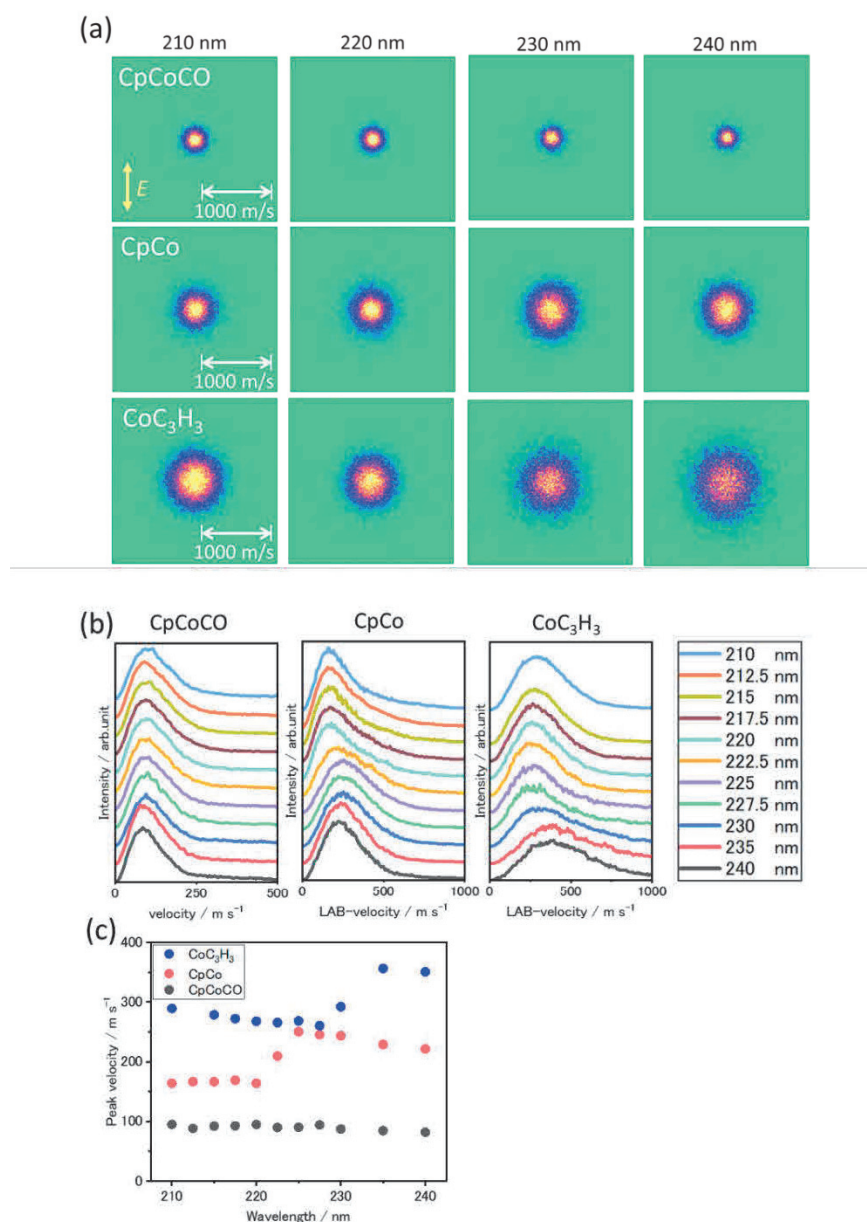


Figure 4-5 (a) Scattering images of the coordinatively unsaturated complexes:

(upper) CpCoCO, (middle) CpCo, and (lower) CoC<sub>3</sub>H<sub>3</sub> at various photolysis wavelengths (210nm, 220 nm, 230 nm, 240 nm) in the MLCT(Cp) band of CpCo(CO)<sub>2</sub>.

(b) Velocity distributions and (c) the peak velocity of the CpCoCO, CpCo, and CoC<sub>3</sub>H<sub>3</sub> fragments generated at various wavelengths in the CpCo(CO)<sub>2</sub> photolysis.

The ion-images of the CpCo, CpCoCO, and CoC<sub>3</sub>H<sub>3</sub> fragments (Figure 4-5(a)) also showed particular photolysis wavelength dependence in the 210 – 240 nm region. While the angular distributions of these three unsaturated complex fragments were constantly isotropic in the MLCT(Cp) band region, the velocity distributions of the CpCo and CoC<sub>3</sub>H<sub>3</sub> fragments shifted at certain wavelengths (Figure 4-5(b)). Such a discontinuous change at a specific wavelength was unobserved in the velocity distribution of the CpCoCO fragment, whose yield spectra were also insensitive to the photolysis wavelength. The wavelength dependence of the velocity distributions is represented as a plot of the maximum velocity in Figure 4-5(c). The single peak in Figure 4-5(b) contains several components attributed to different production origins (Figure 4-1). Among them, a part of the products whose sum of internal and photon energy exceeds the ionization energy can be non-resonantly ionized in the imaging measurements. Thus, the shifts in the peak velocity of the CoC<sub>3</sub>H<sub>3</sub> fragment at approximately 230 nm (5.39 eV, 520 kJ/mol) and the CpCo fragment at 225 nm (5.51 eV, 532 kJ/mol) were regarded as a result of the appearance of the energy components being ionized.

The velocity distribution of the CpCo fragments, which resulted from two CO losses, can be represented by a convoluted function of those of the first photodissociation and secondary processes. We used the image data of the CpCoCO fragment as the velocity distribution of the CpCoCO precursor in the laboratory-frame ( $P_1^{LAB}(v_1)$ ), on which the second CO loss (either  $\text{CpCoCO} \rightarrow \text{CpCo} + \text{CO}$ , or  $\text{CpCoCO} + h\nu_{2\text{nd}} \rightarrow \text{CpCo} + \text{CO}$ ) occurred with the velocity distribution in the center-of-mass frame ( $P_2^{CM}(u_2)$ ). The velocity distributions of the CpCo fragments were measured in the laboratory-frame ( $P_2^{LAB}(v_2)$ ). Using the experimental data of  $P_1^{LAB}(v_1)$  and  $P_2^{LAB}(v_2)$ , we obtained the  $P_2^{CM}(u_2)$  function by the fitting procedure. The results indicated that  $P_2^{CM}(u_2)$  for the second CO loss from CpCoCO (Figure 4-6, left) comprised two velocity components, which were maximized at 200 and 130  $\text{ms}^{-1}$ , respectively. We ascribed the faster

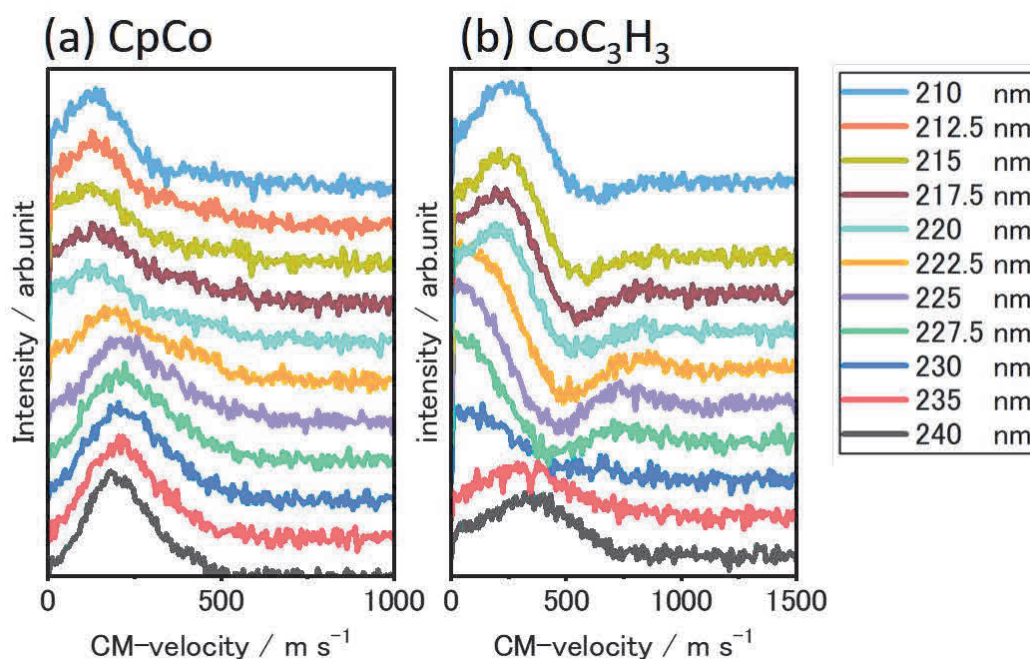


Figure 4-6 Center-of-mass velocity distributions of the CpCo and  $\text{CoC}_3\text{H}_3$  fragments generated at various wavelengths in the  $\text{CpCo}(\text{CO})_2$  photolysis.

component to the second photodissociation ( $\text{CpCoCO} + h\nu_{2\text{nd}} \rightarrow \text{CoCo} + \text{CO}$ ) and the slower one to sequential dissociation ( $\text{CpCoCO} \rightarrow \text{CoCo} + \text{CO}$ ). An attempt was also made to obtain the center-of-mass velocity distributions of the second photodissociation of CpCo ( $\text{CpCo} + h\nu_{2\text{nd}} \rightarrow \text{CoC}_3\text{H}_3 + \text{C}_2\text{H}_2$ ) by applying the same analysis method to the experimental data of the CpCo and  $\text{CoC}_3\text{H}_3$  fragments as  $P_1^{LAB}(v_1)$  and  $P_2^{LAB}(v_2)$ . The analysis yielded unphysical results with negative intensity in  $P_2^{CM}(u_2)$ , as is shown in the right-hand panel in Figure 4-6. The comparable contributions of the second photodissociation and sequential dissociation may have caused the numerical error (Figure 4-2). We examined the numerical analysis approach using several model functions for  $P_1^{LAB}(v_1)$  and  $P_2^{LAB}(v_2)$  to determine whether they could reproduce a known  $P_2^{CM}(u_2)$  input. The artificial intensity was often calculated for such  $P_1^{LAB}(v_1)$  that contains two or more components. Thus, this study did not further discuss the second photodissociation ( $\text{CpCo} + h\nu_{2\text{nd}} \rightarrow \text{CoC}_3\text{H}_3 + \text{C}_2\text{H}_2$ ).

#### 4-3-4. CO photofragment in $\nu = 0,1$

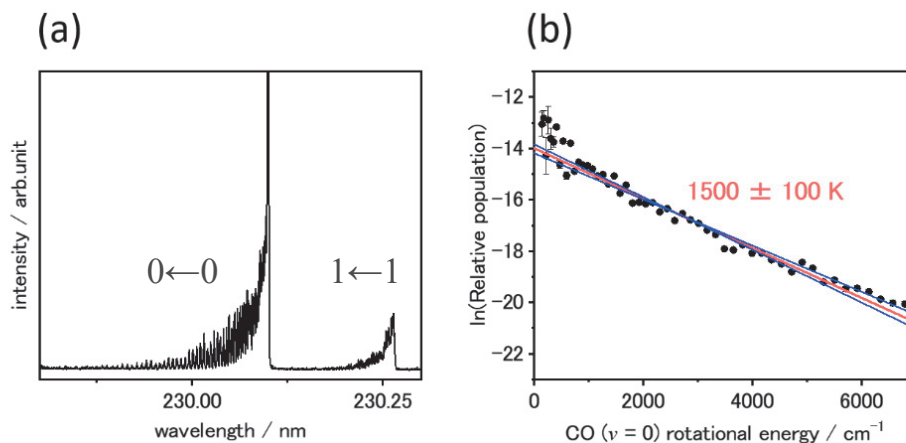


Figure 4-7 (a) REMPI spectra of the CO fragments in the  $\text{CpCo}(\text{CO})_2$  photolysis. (b) Boltzmann plot for the rotational state distribution of the CO fragments in the  $\nu = 0$  state. The red and blue lines indicate the rotational temperatures of 1500 K and (1400K, 1600K), respectively. The prominent peak at the low- $J$  transitions in the  $0_0^0$  band are not due to photofragments but contaminated CO in the sample.

In contrast to the coordinatively unsaturated fragments, state-resolved detection was attainable for the CO fragments, with REMPI spectra at the 230 nm region and a rotational Boltzmann plot for  $\nu = 0$  (Figure 4-7). The measurement of the CO REMPI spectra was spectroscopically limited to the  $\nu = 0$  and 1 vibrational states, in which the population in the highly rotationally excited  $J$  states was observed. Although the rotational structure was not clearly resolved, our analysis yielded the overall rotational temperature of  $1500 \pm 100$  K for the  $\nu = 0$  state (Figure 4-7(b)) and the vibrational state distribution of  $[\nu = 0] : [\nu = 1] \approx 4 : 1$ . The state-resolved scattering images were measured for several  $(\nu, J)$  states. The results are represented as the released linear momentum distributions in Figure 4-8. The linear momentum of the CO fragments increased for

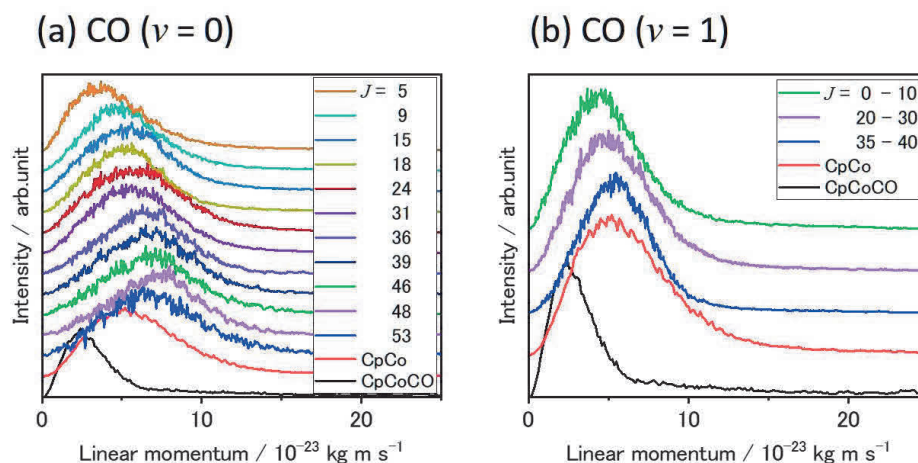


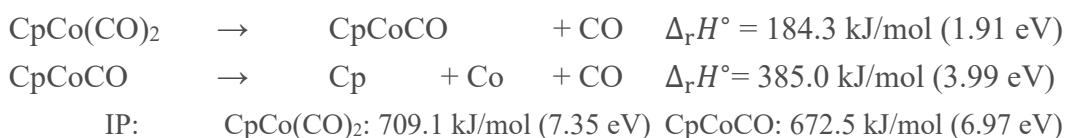
Figure 4-8 State-resolved linear momentum distributions of the CO fragments in the  $\text{CpCo}(\text{CO})_2$  photolysis. The linear momentum distributions of  $\text{CpCo}$  (red) and  $\text{CpCoCO}$  (black) are shown for comparison.

higher rotational  $J$  states. The rotational state-dependence of the linear momentum (and the kinetic energy) release was not readily explained. This may be due to the limited measurement of the CO states to  $\nu = 0$  and 1. An extended investigation into a wider range of the  $(\nu, J)$  states of the CO fragments would be desirable. Alternatively, we confined our discussion to the generation origin of the CO ( $\nu = 0$  and 1) fragments. The counterproduct of CO loss should be  $\text{CpCoCO}$  and  $\text{CpCo}$  based on our experimental result that other possible precursors such as  $\text{CoCO}$ ,  $\text{Co}(\text{CO})_2$ , and  $\text{C}_3\text{H}_3\text{Co}(\text{CO})_2$  were undetected. The linear momentum distributions of  $\text{CpCoCO}$  and  $\text{CpCo}$ , which were obtained from the ion-imaging results, are also shown for comparison in Figure 4-8. The linear momentum distributions of  $\text{CpCo}$  (Figure 4-8, red curve) and CO properly overlapped. The deviation was observed in the higher  $J$  ( $>30$ ) states in the  $\nu = 0$  state, which, however, significantly decreased the relative population. The difference in overlapping between  $\text{CpCo}$  and  $\text{CpCoCO}$  (Figure 4-8, black curve) was more clearly observed in the  $\nu = 1$  state. A good matching of the released momenta indicated a significant contribution of  $\text{CpCoCO} \rightarrow \text{CpCo} + \text{CO}$  ( $\nu = 0$  and 1) in the observed results.

## 4-4. Discussion

### 4-4-1. Competition of sequential dissociation and second photodissociation

Following the first photodissociation generating the CO fragments, the second photodissociation and sequential dissociation of the CpCoCO intermediate can compete, as is generally observed in ultraviolet photolysis of transition-metal carbonyls with a nanosecond laser pulse.<sup>32</sup> The experimental standard enthalpy of reaction ( $\Delta_r H^\circ$ ) and ionization potential (IP) in the literature<sup>28</sup> for the dissociations relevant to the present experiment are as follows:



The photon energy of 500 – 570 kJ/mol (210 – 240 nm) employed in this measurement energetically allowed the loss of two CO at most from the parent through the sequential CO loss ( $\text{CoCp(CO)}_2 + h\nu \rightarrow \text{CpCoCO} + \text{CO} \rightarrow \text{CoCp} + 2\text{CO}$ ). Since the CpCoCO intermediate, which is generated by the first photodissociation ( $\text{CpCo(CO)}_2 + h\nu \rightarrow \text{CpCoCO} + \text{CO}$ ), likely has a photoabsorption cross section as large as that of  $\text{CpCo(CO)}_2$ , the second photodissociation ( $\text{CpCoCO} + h\nu \rightarrow \text{CpCo} + \text{CO}$ ) indeed occurs within an identical pulse with a duration of 10 ns. We took an approach to distinguish these competing processes by measuring the photolysis wavelength dependence of the product velocity, which should vary at the energy threshold of each generation origin. The CpCoCO velocity, with the maximum value depicted in Figure 4-5(c)(●), was almost flat in the 210 – 240 nm region, indicating a single mechanism of the first photodissociation ( $\text{CpCo(CO)}_2 + h\nu \rightarrow \text{CpCoCO} + \text{CO}$ ) upon MLCT(Cp) excitation. This result contrasted with a perceptible decrease in the CpCo velocity at approximately 225 nm (Figure 4-

5(c))(●). We ascribed the apparent decrease in the CpCo velocity in the shorter wavelength region than 225 nm to the participation of ionization of the relatively slower CpCo fragment generated in the sequential dissociation ( $\text{CpCoCO} \rightarrow \text{CpCo} + \text{CO}$ ). Another possible origin of CpCo is the secondary photodissociation of CpCoCO ( $\text{CpCoCO} + h\nu_{2\text{nd}} \rightarrow \text{CpCo} + \text{CO}$ ), whose CpCo product should be much more internally energized to be photoionized with less photon energy. As shown above, the generation of the neutral CpCo fragment both in the sequential dissociation and secondary photodissociation can be energetically allowed even at a wavelength longer than 225 nm. However, the CpCo product in the one-photon sequential dissociation might not be detected in ion-imaging at 225 nm owing to the insufficient photon energy for ionization. The decrease in the translational energy release by the shorter wavelength irradiation, although which looks energetically reversed, can be accounted for by the effective ionization threshold of the slow and less internally excited CpCo fragment at 225 nm. The ionization energy of CpCo, which would provide a quantitative basis for our interpretation, was only not determined in the previous study for the energetics of  $\text{CpCo}(\text{CO})_2$  and its unsaturated complexes.<sup>28</sup> Referring to the ionization energies of 7.35 eV for  $\text{CpCo}(\text{CO})_2$  and 6.97 eV for CpCoCO, the photon energy of 225 nm (532 kJ/mol, 5.51 eV) was somewhat low for the CpCo ionization energy. However, the CpCo fragment ionized in this measurement acquired a fairly large internal energy, among which the electronic energy was more significant. The electronic ground state of CpCo is a triplet, above which the singlet state should be located as a metastable state. Assuming that the CpCo fragment in sequential dissociation is produced in the singlet state, the photon energy required for ionization is lower than the ionization energy by the singlet–triplet energy difference. The singlet–triplet energy difference of CpCo was evaluated as

1.5 eV by the DFT calculation (Table 1), which is comparable to the literature values of 0.6 eV for CpCo(CO)<sub>2</sub> and 1.11 eV for CpCoCO.<sup>37</sup> Thus, our approach was illustrated to differentiate, albeit indirectly, the CpCo fragments with different generation origins (sequential dissociation with one-photon energy and second photodissociation) based on their difference in the velocity distributions. The interpretation would be limited by the non-resonant ionization detection which may exhibit different detection efficiency

Table 1 (a) Singlet–triplet energy gaps, (b) the Co–ligand bond dissociation energy (BDE) of CpCo(CO)<sub>2</sub>, CpCoCO and CpCo, and (c) ionization energy of CpCo(CO)<sub>2</sub><sup>+</sup> and appearance energy of CpCoCO<sup>+</sup> and CpCo<sup>+</sup>. The energy gap in (a) is the relative energy to the minimum of the singlet ground state.

(a)				
	Spin state	$\Delta E$ /eV	Ref. 30 (Exp.)	Ref. 37 (Calc.)
CpCo(CO) <sub>2</sub>	Singlet	--	--	--
CpCoCO	Singlet	2.19	1.91	2.35
	Triplet	1.12		1.23
CpCo	Singlet	4.51		
	Triplet	3.02		
CoC <sub>3</sub> H <sub>3</sub>	Singlet	7.64		
	Triplet	7.35		

(b)		(c)	
	BDE / eV		APE/eV
CpCoCO—CO [S→S]	2.19	CpCo(CO) <sub>2</sub> <sup>+</sup>	7.35
CpCoCO—CO [S→T]	1.12	CpCoCO <sup>+</sup>	8.88
CpCo—CO [S→S]	2.32	CpCo <sup>+</sup>	10.38
CpCo—CO [T→T]	1.91		
CoC <sub>3</sub> H <sub>3</sub> —C <sub>2</sub> H <sub>2</sub> [S→S]	3.12		

depending on the internally excited states of the products. The independence of the CpCoCO signal on the wavelength (Fig. 4-5(c)(●)) can be regarded as a basis for the validity of the analysis.

The shift in the peak velocity of the CoC<sub>3</sub>H<sub>3</sub> fragment at 235 nm (Figure 4-5(c)(●)) was related to the energy threshold of the sequential dissociation (CpCo(CO)<sub>2</sub> + hν → CpCoCO + CO → CpCo + CO + CO). The CoC<sub>3</sub>H<sub>3</sub> generation is primarily attributed to the second photodissociation of CpCo (CpCo + hν<sub>2nd</sub> → CoC<sub>3</sub>H<sub>3</sub> + C<sub>2</sub>H<sub>2</sub>). Because the measured velocity of CoC<sub>3</sub>H<sub>3</sub> ( $V_{CoC_3H_3}^{LAB}$ ) is the sum of the velocity of the precursor ( $V_{CpCo}^{LAB}$ ) and center-of-mass velocity given by the photodissociation ( $v_{CoC_3H_3}^{COM}$ ), the slower CpCo precursor due to sequential dissociation can contribute to decreasing the average velocity of the whole CoC<sub>3</sub>H<sub>3</sub> products through the  $V_{CoC_3H_3}^{LAB} = V_{CpCo}^{LAB} + v_{CoC_3H_3}^{COM}$  relationship. The amount of the velocity shifts of CpCo at 225 nm and CoC<sub>3</sub>H<sub>3</sub> at 235 nm shown in Figure 4-5, both of which we ascribed to the sequential dissociation, were consistently similar to each other ( $\Delta v \approx 100$  m/s), supporting our explanation. Although the photon energy of 235 nm (509 kJ/mol, 5.28 eV) is too high for the energy threshold of sequential dissociation, compared to a known value of the ionic analog (CpCo(CO)<sub>2</sub><sup>+</sup> → CpCo<sup>+</sup> + 2CO) of 3.03 eV,<sup>28</sup> the sufficiently high internal energy of the precursors facilitates both steps of sequential CO loss. As a result, the products (CpCo and 2CO) are likely to be rovibrationally excited. The effective energy threshold of sequential dissociation can exceed the energetics, giving a basis for our interpretation of the velocity shift at 235 nm. Nevertheless, the determination of either the ionization energy of CpCo or the bond dissociation energy of CpCoCO → CpCo + CO has been desired as a critical value for the whole energetic of CpCo(CO)<sub>2</sub>, CpCo(CO)<sub>2</sub><sup>+</sup> and their unsaturated families.<sup>28</sup>

#### 4-4-2. Identification of the counterproduct of the second photodissociation

CO fragments can be generated in any of the first photodissociation, sequential dissociation, or second photodissociation. The results of the momentum overlapping of the CO ( $\nu = 0$  and 1) fragments with the CpCo product shown in Figure 4-8 (red curve) indicate their paired production. The photolysis wavelength of the momentum matching measurements was 230 nm, at which the CpCo velocity was biased to the faster side (Figure 4-5(c)(●)). We ascribed the faster CpCo fragment to the second photodissociation of CpCoCO in the previous section. Thus, the production origin of the low- $\nu$  CO is likely to be the second photodissociation of CpCoCO:  $\text{CpCoCO} + h\nu_{2\text{nd}} \rightarrow \text{CpCo} + \text{CO}(\nu = 0, 1)$ . Because of the limitation of the REMPI detection of CO in the  $\nu = 0$  and 1 states, the population of the higher vibrationally excited states ( $N_{\nu \geq 2}$ ) was not evaluated in the present measurements. Following the thermal distribution with the analyzed temperature of 1500 K (Figure 4-7), the  $N_{\nu=2}/N_{\nu=0}$  ratio was estimated as small as 0.05, implying a much smaller  $N_{\nu \geq 2}$  population. In addition, a fairly good momentum matching conversely suggested that the CO fragments in the first photodissociation, which was not measured, are likely populated in the  $\nu \geq 2$  states.

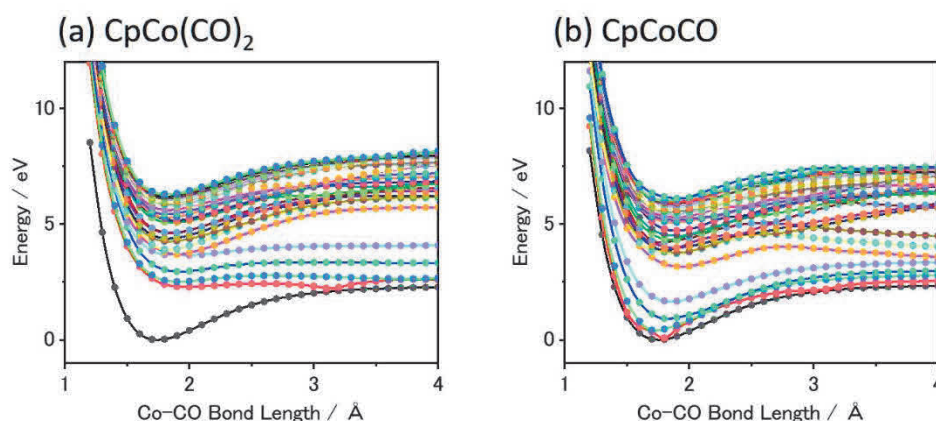


Figure 4-9 Potential energy curves of the Co-CO dissociation of (a) CpCo(CO)<sub>2</sub> and (b) CpCoCO calculated at the TD-DFT level of theory.

#### 4-4-3. Potential energy curves of the CO loss of CpCo(CO)<sub>2</sub> and CpCoCO

Figure 4-9 shows the potential energy curves responsible for CO loss calculated for the singlet ground and excited states of CpCp(CO)<sub>2</sub> and CpCoCO. Our calculations revealed dense electronic excited state structures above 4 eV for both CpCo(CO)<sub>2</sub> and CpCoCO, indicating efficient internal conversion upon photoexcitation in the 210 – 240 nm region. A qualitative difference in the electronic structures of CpCo(CO)<sub>2</sub> and CpCoCO was found in the lower excited states. The potential energy curves of the low excited states of CpCo(CO)<sub>2</sub> were mostly repulsive concerning the Co–CO bond with an apparent energy gap to the electronic ground state, while the quasi-bound regions converging to the ground state potential energy curve appeared in the lower excited states of CpCoCO. Given that internal conversion proceeds at a faster rate among energetically closer electronic states, the calculated potential energy curves imply that the first photodissociation ( $\text{CpCo(CO)}_2 + h\nu \rightarrow \text{CpCoCO} + \text{CO}$ ) likely occurs in the lower excited states following a fast electronic relaxation from the higher photoinitiated states, and the precursor of the second photodissociation (CpCoCO) is highly internally excited.<sup>10</sup> The prediction based on the experimental and theoretical results suggests that the relative time scale of CO dissociation to the internal conversion of transition-metal carbonyls can depend on the topology of potential energy curves and the energy gap to the ground state.

#### 4-4-4. Stability of CoC<sub>3</sub>H<sub>3</sub> as an intermediate in CpCo photodissociation

The signal of CoC<sub>3</sub>H<sub>3</sub><sup>+</sup> was detected with a relatively larger intensity in the product yield spectra (Figure 4-4). Since accurate ionization efficiency data are unavailable, the production branching ratio of CoC<sub>3</sub>H<sub>3</sub> to other coordinatively unsaturated complexes was not determined. The CoC<sub>3</sub>H<sub>3</sub> complex is so stable that the appearance energy was precisely measured as 16.8 eV.<sup>38</sup> We confirmed the stable structure of CoC<sub>3</sub>H<sub>3</sub>

by DFT calculations (Figure 4-10).

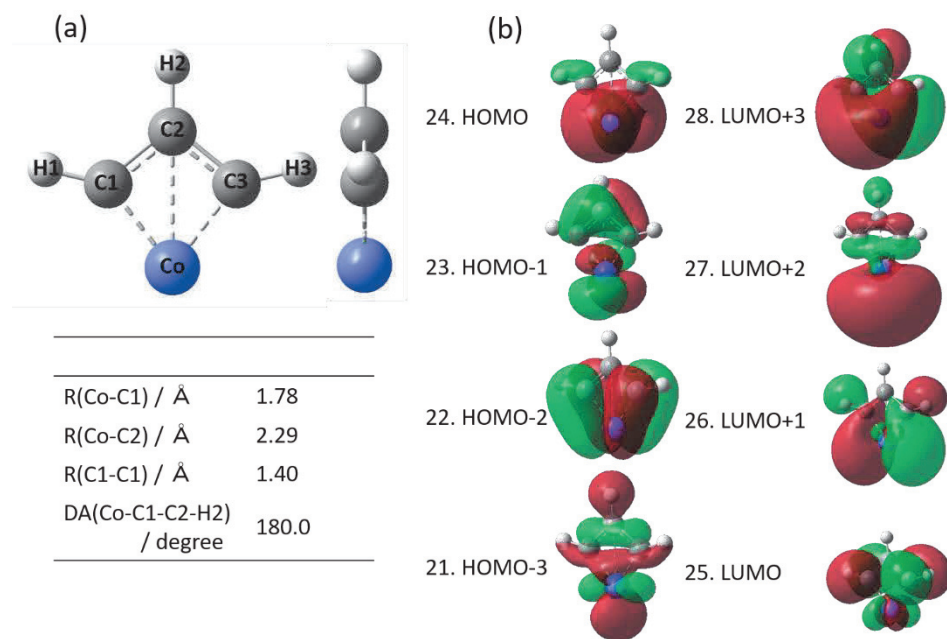


Figure 4-10 The molecular structure (a) and several molecular orbitals relevant to the ultraviolet absorptions (b) of  $\text{CoC}_3\text{H}_3$  calculated at the level of TD-DFT theory. The structural parameters shown in (a) are the optimized values in the singlet electronic ground state. The  $\text{CoC}_3\text{H}_3$  complex has a planar structure. The numbers at an individual molecular orbital denote the order of the orbital energy.

The  $\text{CoC}_3\text{H}_3$  complex is energetically optimized with the two carbon atoms bound to the Co center, exhibiting different bonding characteristics from the Cp ligand which has the  $\eta^5$  form. The generation of  $\text{CoC}_3\text{H}_3$  is presumably due to the photodissociation of CpCo ( $\text{CpCo} + h\nu_{2\text{nd}} \rightarrow \text{CoC}_3\text{H}_3 + \text{C}_2\text{H}_2$ ) based on the observed result; the similar velocity shifts of CpCo and  $\text{CoC}_3\text{H}_3$  (Figure 4-5) support that CpCo is the precursor of the  $\text{CoC}_3\text{H}_3$  product, and the absence of the  $\text{CoC}_3\text{H}_3(\text{CO})_{1,2}$  signals (Figure 4-4) indicates that the loss of CO precedes the decomposition of the Cp ligand. The decomposition of cyclic alkyl ligands due to ultraviolet photoexcitation was observed for metal ion complexes.<sup>39,40</sup> Although  $\text{C}_5\text{H}_5$  is generally known as a stable ligand especially in its anionic form, the

MLCT(Cp) excitation could cause the decomposition of the Cp framework and conformation conversion to the relatively stable  $C_3H_3$  coordination in the CpCo photodissociation.

#### 4-4-5. Contribution of the singlet and triplet states in the CpCo(CO)<sub>2</sub> photodissociation

The electronic ground state of CpCo(CO)<sub>2</sub> is singlet, whereas CpCoCO and CpCo have a triplet ground state and a low-lying singlet state as a metastable state. The reactivity of the CpCo(CO)<sub>2</sub> family in the singlet and triplet states was investigated by Carreon-Macedo and Harvey with the DFT and CCSD calculations, based on which the potential energy surfaces regarding ligand addition reactions were discussed.<sup>37</sup> The singlet–triplet energy gap of CpCo(CO)<sub>2</sub> and CpCoCO–CO bond dissociation energy were well reproduced by our DFT calculations. The singlet–triplet energy gaps and Co–ligand bond dissociation energies of CpCo(CO)<sub>2</sub>, CpCoCO, and CpCo are summarized in Table 1. The Co–CO bond dissociation energy, which was approximately 200 kJ/mol, was not significantly different in the singlet and triplet states or among the neutral and ionic unsaturated complexes. Our assumption that the CpCoCO and CpCo fragments are produced in the singlet states, for which only the singlet potential energy curves were considered (Figure 4-9), was based on the common photochemistry of transition-metal carbonyls. Photochemistry of Fe(CO)<sub>5</sub>, which is a typical transition-metal carbonyl, has been intensively investigated in theoretical and experimental studies,<sup>2,10,12,41,42</sup> in which one- and two-CO loss generating Fe(CO)<sub>4</sub> and Fe(CO)<sub>3</sub> in the singlet potential energy surfaces is corroborated. The spin-orbit interaction in the electronic excited states of CpCo(CO)<sub>2</sub> and CpCoCO would facilitate the participation of the triplet states in the

whole photochemistry. The Cp ligand could play a role in mixing the triplet character. However, since any results positively indicating the triplet state participation were unobtained in the present experiments, we assumed that the first and second photodissociation and sequential dissociations proceeded on the singlet potential energy surfaces. Theoretical studies with calculations of the spin-orbit interaction<sup>43</sup> are desired for elucidating the spin states relevant to the photochemistry of the MLCT(Cp) band.

#### 4-5. Conclusion

The photodissociation dynamics of  $\text{CpCo}(\text{CO})_2$  was investigated in the 210 – 240 nm region. Our quantum chemistry calculations characterized the photoabsorption band in the examined region as the MLCT(Cp) transition. The experiments under the one-color scheme, where photodissociations and ionizations were accomplished within a single laser pulse, revealed the generation of coordinatively unsaturated complexes and CO fragments. The relative yield spectra of these unsaturated complexes and their recoil velocity distributions were measured as a function of photon energy. The experimental results indicated that, following the first photodissociation ( $\text{CpCo}(\text{CO})_2 + h\nu \rightarrow \text{CpCoCO} + \text{CO}$ ), the CpCoCO unsaturated complex underwent sequential dissociation ( $\text{CpCoCO} \rightarrow \text{CpCo} + \text{CO}$ ) and second photodissociation ( $\text{CpCoCO} + h\nu_{2\text{nd}} \rightarrow \text{CpCo} + \text{CO}$ ,  $\text{CpCo} + h\nu_{2\text{nd}} \rightarrow \text{CoC}_3\text{H}_3 + \text{C}_2\text{H}_2$ ). The analysis based on the released momentum matching suggested that the CO ( $\nu = 0$  and 1) fragments were the counterproducts of CpCo in the second photodissociation of CpCoCO. The average recoil velocities of CpCo and  $\text{CoC}_3\text{H}_3$  exhibited step-like decreases at 225 nm and 235 nm, respectively, as the photon energy increased. The slow shifts were ascribed to the onset of ionization of the slow CpCo fragment in the sequential dissociation of CpCoCO

and the  $\text{CoC}_3\text{H}_3$  fragment in the second photodissociation of the CpCo precursor. The same amount of velocity shifts of the CpCo and  $\text{CoC}_3\text{H}_3$  fragments provided additional experimental support for the contribution from the common CpCoCO precursor. The measurement results contained some outcomes of the second photodissociation of the CpCoCO and CpCo unsaturated intermediates, which are usually selectively hard to observe in laser photolysis of the transition-metal complexes. The pathways of CO loss from CpCo(CO)<sub>2</sub> and CpCoCO were also theoretically investigated to explain the experimental results. A notable difference in the potential energy curves responsible for CO loss from CpCo(CO)<sub>2</sub> and CpCoCO was found in the low-lying excited states; a relatively large energy gap was formed between the ground state and repulsive excited states of CpCo(CO)<sub>2</sub>, whereas the potential energy curves with the bound state regions were relatively continuous from the excited states to the ground state of CpCoCO. Considering that internal conversion, which is a preceding photochemical process to others in transition-metal carbonyls, is faster among the states with the smaller energy difference, a probable reaction route of first CO loss is inferred to evolve in the low-lying repulsive excited states of CpCo(CO)<sub>2</sub>. Time-resolved experiments will be helpful in confirming our speculation as well as dynamics calculations for the excited states. The overall photochemistry of CpCo(CO)<sub>2</sub> and its unsaturated complexes were assumed to proceed in the spin singlet states in the calculations of the potential energy surfaces and the bond dissociation energies relevant to CO loss. The assumption of singlet state reactions can be a subject of future studies. CO loss, which is a major process in the photochemistry of metal carbonyl complexes, governs the generation of highly reactive unsaturated complexes. In this study, we demonstrated experimental discrimination of CO fragments with different generation origins (sequential dissociation and second

photodissociation) by measuring the wavelength dependence of the recoil velocity distributions of the coordinatively unsaturated intermediates.

## References

1. Rossi AR, Hoffmann R. Transition-Metal Pentacoordination. *Inorganic Chemistry* 1975;14(2):365-374, doi:10.1021/ic50144a032
2. Malcomson T, McKinlay RG, Paterson MJ. One- and Two-Photon-Induced Photochemistry of Iron Pentacarbonyl Fe(CO)(5) : Insights from Coupled Cluster Response Theory. *Chemphotochem* 2019;3(9):825-832, doi:10.1002/cptc.201900111
3. Daniel C, Benard M, Dedieu A, et al. Theoretical Aspects of the Photochemistry of Organometallics .3. Potential Energy Curves for the Photodissociation of Fe(CO)5. *J Phys Chem* 1984;88(21):4805-4811, doi:10.1021/j150665a004
4. Dick B, Freund HJ, Hohlneicher G. Calculation of Transition-metal Compounds Using an Extension of the CNDO Formalism.4. CNDO-CI-Calculations on Ni(CO)4 and Fe(CO)5 - Electronic Spectra and Photochemical Implications. *Molecular Physics* 1982;45(2):427-439, doi:10.1080/00268978200100341
5. Trushin SA, Kosma K, Fuss W, et al. Wavelength-independent ultrafast dynamics and coherent oscillation of a metal-carbon stretch vibration in photodissociation of Cr(CO)(6) in the region of 270-345 nm. *Chemical Physics* 2008;347(1-3):309-323, doi:10.1016/j.chemphys.2007.09.057
6. Vlcek A. The life and times of excited states of organometallic and coordination compounds. *Coordination Chemistry Reviews* 2000;200(933-977), doi:10.1016/s0010-8545(00)00308-8
7. Wrighton M. Photochemistry of Metal-Carbonyls. *Chemical Reviews* 1974;74(4):401-430, doi:10.1021/cr60290a001
8. Turner JJ, George MW, Poliakoff M, et al. Photochemistry of transition metal carbonyls. *Chemical Society Reviews* 2022;51(13):5300-5329, doi:10.1039/d1cs00826a
9. Trushin SA, Fuss W, Schmid WE, et al. Femtosecond Dynamics and Vibrational Coherence in Gas-phase Ultraviolet Photodecomposition of Cr(CO)6. *J Phys Chem A* 1998;102(23):4129-4137, doi:10.1021/jp973133o
10. Trushin SA, Fuss W, Kompa KL, et al. Femtosecond Dynamics of Fe(CO)5 Photodissociation at 267 nm Studied by Transient Ionization. *J Phys Chem A* 2000;104(10):1997-2006, doi:10.1021/jp992474u
11. Fuss W, Trushin SA, Schmid WE. Ultrafast photochemistry of metal carbonyls. *Research*

- on Chemical Intermediates 2001;27(4-5):447-457, doi:10.1163/156856701104202093
12. Wernet P, Leitner T, Josefsson I, et al. Direct evidence for sequential dissociation of gas-phase Fe(CO)<sub>5</sub> via a singlet pathway upon excitation at 266 nm. *J Chem Phys* 2017;146(21):211103, doi:10.1063/1.4984774
  13. Wernet P, Kunnus K, Josefsson I, et al. Orbital-specific mapping of the ligand exchange dynamics of Fe(CO)<sub>5</sub> in solution. *Nature* 2015;520(7545):78-81, doi:10.1038/nature14296
  14. Boylan MJ, Black JD, Braterman PS. Metal-carbonyl Photochemistry. 1. Photolysis of the Group-6 Hexacarbonyls in Hydrocarbon Glasses - the Species M(CO)<sub>5</sub>, M(CO)<sub>4</sub>, M(CO)<sub>3</sub>, and M(CO)<sub>5</sub>(OH<sub>2</sub>). *Journal of the Chemical Society-Dalton Transactions* 1980;9):1646-1650, doi:10.1039/dt9800001646
  15. Black JD, Boylan MJ, Braterman PS, et al. Metal carbonyl photochemistry. Part 2. Photochemistry of hexacarbonyls in glasses containing oxygen donors; the species [M(CO)<sub>5</sub>(mthf)] (M = Cr, Mo, W, or V-I), cis-[M(CO)<sub>4</sub>(mthf)<sub>2</sub>], and fac-[M(CO)<sub>3</sub>(mthf)<sub>3</sub>] (M = Cr, Mo, or W). *Journal of the Chemical Society-Dalton Transactions* 1980;9):1651-1654, doi:10.1039/dt9800001651
  16. Schlenker FJ, Bouchard F, Waller IM, et al. State Resolved Photofragmentation of Ni(CO)<sub>4</sub> at 193, 248, and 308 nm: A Detailed Study of the Photodissociation Dynamics. *J Chem Phys* 1990;93(10):7110-7118, doi:10.1063/1.459434
  17. Waller IM, Hepburn JW. State-Resolved Photofragmentation Dynamics of Fe(CO)<sub>5</sub> at 193, 248, 266, and 351 nm. *J Chem Phys* 1988;88(10):6658-6669, doi:10.1063/1.454406
  18. Whetten RL, Fu KJ, Grant ER. Photodissociation dynamics of Fe(CO)<sub>5</sub>: Excited state lifetimes and energy disposal. *J Chem Phys* 1983;79(10):4899-4911, doi:10.1063/1.445582
  19. Willey KF, Brummel CL, Winograd N. Photoionization mechanisms for Cr(CO)<sub>6</sub> using high intensity laser pulses in the near-IR. *Chemical Physics Letters* 1997;267(3-4):359-364, doi:10.1016/s0009-2614(97)00089-4
  20. Gobeli DA, Yang JJ, El-Sayed MA. Laser Multiphoton Ionization Dissociation Mass-Spectrometry. *Chemical Reviews* 1985;85(6):529-554, doi:10.1021/cr00070a002
  21. Duncan MA, Dietz TG, Smalley RE. Efficient Multi-Photon Ionization of Metal-Carbonyls Cooled in a Pulsed Supersonic Beam. *Chemical Physics* 1979;44(3):415-419, doi:10.1016/0301-0104(79)85224-6
  22. Nagamori K, Haze M, Nakata H, et al. Generation of Highly Vibrationally Excited CO in Sequential Photodissociation of Iron Carbonyl Complexes. *J Phys Chem A* 2022;126(2):306-313, doi:10.1021/acs.jpca.1c09922
  23. Nakata H, Nagamori K, Haze M, et al. Primary and Secondary Loss of CO and NO Ligands in the Ultraviolet Photodissociation of the Heteroleptic Co(CO)<sub>3</sub>NO Complex. *J Phys Chem A* 2020;124(51):10694-10704

24. Nakata H, Nagamori K, Yamasaki K, et al. Detection of direct NO ligand loss in the ultraviolet photodissociation of Co(CO)<sub>3</sub>NO. *Chemical Physics Letters* 2018;707(150-153, doi:10.1016/j.cplett.2018.07.049
25. Kohge Y, Hanada T, Sumida M, et al. Photodissociation dynamics of nitromethane at 213 nm studied by ion-imaging. *Chemical Physics Letters* 2013;556(49-54, doi:10.1016/j.cplett.2012.11.076
26. Katayanagi H, Suzuki T. Non-adiabatic bending dissociation of OCS: the effect of bending excitation on the transition probability. *Chemical Physics Letters* 2002;360(1-2):104-110, doi:10.1016/s0009-2614(02)00788-1
27. Banares L, Baumert T, Bergt M, et al. The Ultrafast Photodissociation of Fe(CO)<sub>5</sub> in the Gas Phase. *J Chem Phys* 1998;108(14):5799-5811, doi:10.1063/1.475991
28. Sztaray B, Szepes L, Baer T. Neutral cobalt-carbonyl bond energy by combined threshold photoelectron photoion coincidence and He(I) photoelectron spectroscopy. *J Phys Chem A* 2003;107(44):9486-9490, doi:10.1021/jp035965u
29. Li XR, Bancroft GM, Puddephatt RJ, et al. Variable-energy photoelectron spectroscopy of CpM(CO)<sub>2</sub> (M=Co, Rh, Ir): Molecular orbital assignments and all evaluation of the difference in ground-state orbital characters. *Organometallics* 1996;15(13):2890-2904, doi:10.1021/om960202x
30. Sztaray B, Baer T. Dissociation dynamics and thermochemistry of energy-selected CpCo(CO)<sub>2</sub>(+) ions. *Journal of the American Chemical Society* 2000;122(38):9219-9226, doi:10.1021/ja001077q
31. Leutwyler S, Even U. Laser Multi-Photon Dissociation and Ionization of Polynuclear Metal-Carbonyls in Supersonic Beams. *Chemical Physics Letters* 1981;84(1):188-193, doi:10.1016/0009-2614(81)85398-5
32. Venkataraman BK, Bandukwalla G, Zhang ZJ, et al. One-Photon and two-Photon Photodissociation of Fe(CO)<sub>5</sub> at 248-nm - Application of an Accurate Method for Calculating Angle Resolved Velocity Distributions for Multiple Sequential Bond Rupture Processes. *J Chem Phys* 1989;90(10):5510-5526, doi:10.1063/1.456404
33. M. J. Frisch GWT, H. B. Schlegel, G. E. Scuseria, M. A. Robb, J. R. Cheeseman, G. Scalmani, V. Barone, G. A. Petersson, H. Nakatsuji, X. Li, M. Caricato, A. V. Marenich, J. Bloino, B. G. Janesko, R. Gomperts, B. Mennucci, H. P. Hratchian, J. V. Ortiz, A. F. Izmaylov, J. L. Sonnenberg, D. Williams-Young, F. Ding, F. Lipparini, F. Egidi, J. Goings, B. Peng, A. Petrone, T. Henderson, D. Ranasinghe, V. G. Zakrzewski, J. Gao, N. Rega, G. Zheng, W. Liang, M. Hada, M. Ehara, K. Toyota, R. Fukuda, J. Hasegawa, M. Ishida, T. Nakajima, Y. Honda, O. Kitao, H. Nakai, T. Vreven, K. Throssell, J. A. Montgomery, Jr., J. E. Peralta, F. Ogliaro, M. J. Bearpark, J. J. Heyd, E. N. Brothers, K. N. Kudin, V. N. Staroverov, T. A. Keith, R. Kobayashi, J. Normand, K.

- Raghavachari, A. P. Rendell, J. C. Burant, S. S. Iyengar, J. Tomasi, M. Cossi, J. M. Millam, M. Klene, C. Adamo, R. Cammi, J. W. Ochterski, R. L. Martin, K. Morokuma, O. Farkas, J. B. Foresman, and D. J. Fox, Gaussian, Inc., Wallingford CT, 2016. Gaussian 16, Revision C.01.
34. Beagley B, Parrott CT, Ulbrecht V, et al. Gas-phase Electron-diffraction Study of the Molecular Structures of Cyclopentadienyls Cobalt Dicarbonyl,  $C_5H_5CO(CO)_2$ . *Journal of Molecular Structure* 1979;52(1):47-52, doi:10.1016/0022-2860(79)80093-9
  35. Oana M, Nakatsuka Y, Albert DR, et al. Photodissociation Dynamics of Gaseous  $CpCo(CO)_2$  and Ligand Exchange Reactions of  $CpCoH_2$  with  $C_3H_4$ ,  $C_3H_6$ , and  $NH_3$ . *Journal of Physical Chemistry A* 2012;116(21):5039-5044, doi:10.1021/jp3018919
  36. Hansen CS, Marchetti B, Karsili TNV, et al. Ultraviolet photodissociation of gas-phase transition metal complexes: dicarbonylcyclopentadienylidodiron(II). *Molecular Physics* 2020, doi:10.1080/00268976.2020.1813343
  37. Carreon-Macedo JL, Harvey JN. Do spin state changes matter in organometallic chemistry? A computational study. *Journal of the American Chemical Society* 2004;126(18):5789-5797, doi:10.1021/ja049346q
  38. Winters RE, Kiser RW. Ions produced in the mass spectrometer from cyclopentadienylmetal carbonyl compounds of cobalt, manganese and vanadium. *Journal of Organometallic Chemistry* 1965;4(3):8
  39. Marks JH, Batchelor AG, Blais JRC, et al. Cation Complexes of Uranium and Thorium with Cyclooctatetraene: Photochemistry and Decomposition Products. *J Phys Chem A* 2022, doi:10.1021/acs.jpca.2c03035
  40. Jaeger TD, Duncan MA. Photodissociation processes in transition-metal cation complexes with cyclooctatetraene. *J Phys Chem A* 2004;108(51):11296-11301, doi:10.1021/jp0462557
  41. Cole-Filipiak NC, Tross J, Schrader P, et al. Ultraviolet photodissociation of gas-phase iron pentacarbonyl probed with ultrafast infrared spectroscopy. *J Chem Phys* 2021;154(13), doi:10.1063/5.0041074
  42. Gonzalez-Blanco O, Branchadell V. Density functional study of the Fe-CO bond dissociation energies of  $Fe(CO)_5$ . *J Chem Phys* 1999;110(2):778-783, doi:10.1063/1.478045
  43. Cole-Filipiak NC, Tross J, Schrader P, et al. Ultrafast infrared transient absorption spectroscopy of gas-phase  $Ni(CO)_4$  photodissociation at 261 nm. *J Chem Phys* 2022;156(14), doi:10.1063/5.0080844

# Chapter 5

## General Conclusions

The aim of this study was to determine the origin of CO fragments produced by multi-step dissociation reactions of transition metal carbonyl complexes. In the photodissociation reaction of  $\text{Fe}(\text{CO})_5$ , highly vibrationally excited CO with vibrational state  $\nu > 10$  was detected, which was found to be the origin of dissociation from  $\text{FeCO}$ . In  $\text{CpCo}(\text{CO})_2$ , the wavelength dependence of the recoil velocity distribution of the coordinatively unsaturated intermediate was measured to identify CO fragments of different formation origins ( Sequential dissociation and second photodissociation) were experimentally demonstrated. As a new attempt, I have also developed an analytical method to obtain the velocity distribution in the center of mass coordinate system.

Despite the fact that state selection of photofragments using ion imaging is an effective method for studying reaction dynamics, its application to the study of photodissociation reactions of transition metal complexes has been limited. However, measuring the wavelength dependence has proven to be useful; CO fragments tend to be difficult to obtain wavelength dependence due to spectroscopic limitations. On the other hand, unsaturated photofragments can be ionized non-resonantly, so the reaction dependence of the dissociation can be measured from the ion yield spectra and scattering distribution images. Combining these results on the unsaturated complex side with those of CO, it is possible to determine which dissociation step the detected CO is a product of. We hope that this study will promote future experimental and theoretical studies.

# Acknowledgement

This study was conducted at Physical Chemistry of Kinetics laboratory, Department of Chemistry, Graduate School of Science, Hiroshima University.

I would like to express my sincere gratitude to my supervisor, Associate Professor Hiroshi Kohguchi, for his support in carrying out this research. Although I fell behind many times, I received reassuring support in the face of difficulties. I could not have accomplished this research without his support. I am profoundly thankful to Professor Katsuyoshi Yamasaki for his detailed insight into physical chemistry and for his encouragement of my research. I am grateful to Professor Schlemmer, Dr. Asvany, and the entire team at the University of Cologne's laboratory for providing me with the invaluable chance to engage with diverse research fields. I am also grateful to the staff of the Hiroshima University Monozukuri (Craftwork) Plaza for their assistance in developing the equipment. Lastly, I extend my deepest gratitude to every member of the Physical Chemistry and Kinetics Laboratory for their invaluable support.

KEIGO NAGAMORI